First-Principles Study on Dilute Magnetic States and Half Metallicity in Chalcopyrite Semiconductors

Ph.D. Dissertation

A dissertation submitted in partial fulfillment of the requirements for the degree of

philosophiae doctor in Theoretical Condensed Matter (Quantum) Physics

Mohammad **Shahjahan**

Department of Physics, Graduate School of Science, Osaka University, Japan

Osaka University

Contents

Dedication

To

my

beloved

child

AFNAN-kun

Abstract

Electronic states, band structures, dilute magnetic states and magnetic properties of group I-III-VI_2 based transition metal (TM) doped chalcopyrite compounds $A(BX)C_2$ and $A(BXY)C_2$ are calculated using the Green's function method of Korringa-Kohn-Rostoker and full-potential linearized augmented plane wave method, where A=Cu, Ag, B=Al, In, C=S, Se and X, Y= Ti, V, Cr, Mn, Fe, Co, and Ni. Single impurity doped compounds $A(BX)C_2$ exhibit a stable ferromagnetic (FM) state and half metallicity relative to a metallic disordered spin moment (DSM) state, when X=Ti, V, Cr, and Mn at low-concentration of each TM ion are incorporated at host cation B^{3+} site. Some of them exhibit magnetic transition temperatures above room temperature. On the contrary, in Fe, Co, and Ni doped alloys, instability of FM states to DSM is obtained. The situation is contrasting for simultaneous doping of a TM pair. Codoped compounds $A(BXY)C_2$ can exhibit a FM, ferrimagnetic (FiM) and antiferromagnetic (AF) states depending on the orientation of the local spins and net moments. A parallel order of spins determines FM states, whereas the antiparallel arrangements give rise to FiM states and especially AF states are obtained for null net moments. Some of the FiM and AF states are stable energetically relative to a DSM state and depict the half metallicity when TM pairs at equal concentrations and with d electrons occupancy less and more than half filled are implanted at host cation B^{3+} site. In some other codopant cases, instability of FiM states to DSM is obtained. Total energy, electronic charge density, magnetic critical temperatures, net moments, local spin moments, fixed spin moments, spin-orbit interaction properties, hyperfine fields, and enthalpy of formations are calculated. Calculated dilute magnetic states, half metallicity and other several magnetic properties imply that TM doped chalcopyrite type compounds $A(BX)C_2$ and $A(BXY)C_2$ are promising for respective spintronics applications.

Keywords: **Dilute Magnetic States, Half Metallicity, Chalcopyrite, Coherent Potential Approximation, KKR-Green's Function, FLAPW.**

PACS: 71.20.Nr, 75.50.Pp

Chapter 1

Introduction

Condensed state is one of the interesting and challenging branch of matters because the knowledge of it helps to design, synthesis and understand technologically important new materials. Magnetic and semiconducting properties at condensed states are the most fascinating areas of current research. Though some facts have long been known, several attempts have been made so far to understand the behavior of these materials from first-principles (*ab-initio*) methods. The first-principles electronic structure calculations are crucial to understand the underlying mechanisms and to further design new candidates of useful materials.

Numerous efforts were taken to exploit electron spins as a new degree of freedom of electronic charges in electronic devices, which is known as spin-electronics or spintronics [1]. The primal issue of spintronics is the half metallicity [2,3] i.e., metallic in one spin channel of electrons and semiconducting or insulating in the other spin direction, as shown schematically in **Fig.** 1.1. Materials having such a property are prominent candidates for data processing and info-storage, which is the field of present interest.

Many physical properties at condensed states are generally determined by the valence electrons. The valence electrons play important roles in electronic states and magnetic properties. Therefore, understanding the electronic structure of valence and conduction states is a crucial step in condensed matter theory. This branch of study is referred to as the theory of electronic structure of matter, or electronic structure calculation.

For calculating electronic structures of various matters many different methods have been proposed. Among them are Korringa-Kohn-Rostoker (KKR) Green's function [4,5], full-potential linearized augmented plane wave (FLAPW) [6-9], pseudopotential, projector augmented wave (PAW), linear muffin-tin orbital (LMTO), linear combination of atomic orbital (LCAO), and so on, which normally are combined with the density functional theory (DFT). In DFT [10,11], the basic quantity is the electron density. In particular, the exchange-correlation energy is the functional of the electron density. Once we know this functional, we can determine the electronic structures through solving Kohn-Sham equation of DFT [11]. However, it is impossible to know the exact form of this functional and we have to use some approximation. Most commonly used approximation is the local density approximation (LDA) or generalized gradient approximation (GGA) [12,13]. Using such an approximation we can rather accurately calculate the electronic structures. To study the magnetic and spin electronics properties one needs to have spin dependent electron density distribution. Once we have the knowledge of electronic structures, we can apply it to understand different features of solids, energy band structures, magnetic properties and half metallicity of technologically important spintronics materials.

Therefore, we perform the electronic structure calculations of spintronics materials, namely chalcopyrite semiconductors using the KKR [4,5] Green's function and FLAPW [6-9] method and then we investigate magnetic half metallicity and magnetic properties of chalcopyrite-type dilute magnetic states (DMS) with transition metal (TM) impurities doped. The KKR Green's function is the main solver in the present study for suitability to alloy systems, while the FLAPW method is used mainly for checking the numerical accuracy and adopted models (coherent potential approximation and supercell doping).

There are many different challenging areas of crystalline materials which are not completely understood theoretically yet. Among them the understanding of microscopic features of magnetic and semiconducting properties are far from complete. For example, some theories can explain the Slater-Pauling curve [14] of magnetization for substitutional alloys very well but fails to predict the Curie temperature, one of the most important features of magnetic materials, with the same level of accuracy. Moreover, the signs and magni-

tudes of the exchange coupling constants, J_{ij} are not well understood. Although some attempts have already been made in this direction, [14,15] where the electronic structures of the TM alloys are calculated by using the KKR method combined with the coherent potential approximation (CPA) [16] and LDA. Still a self-consistent theory for explaining the Slater-Pauling curve and Curie temperature within the same approach is lacking in the literature. On the other hand, KKR-CPA calculation explains various electrical and magnetic behaviors of $3d$ pyrite-type and $3d$ TM doped chalcopyrite-type mixed crystals well as long as the systems are in a metallic phase [17], but there still remain some discrepancies between the theory and experiment in the insulating or semiconducting phases. To remove the discrepancy, above point has to be investigated further both theoretically and experimentally. The theoretical challenge is to treat the loosely packed crystal structure in a spherical potential models such as the muffin-tin potential approximation (MTA) and atomic-sphere approximation (ASA): One of the useful methods is the MTA, which can be easily combined with CPA and other techniques using Green's functions. There is still a large scope to contribute in this area of physics. The knowledge gained this way will help us to design and construct new materials that will exhibit new properties and, will find potential applications in the industry.

In recent years some new materials are developed which have bright future for potential applications in the modern and ultramodern devices. One of them is the half metallic system that has drawn the interest of both theoreticians and experimentalists. The half metallicity [2,3] can play an important role on the device applications. But the theoretical understanding of these materials is still in a preliminary stage and have many rooms to find half metallicity with magnetic transition temperatures above room temperature. The first-principles study on different properties of spintronics materials (formed from group I-III-VI_2 elements) require the knowledge of electronic density of states or electron density. Electronic band structures provide a lucid evidence of metallic, insulating or half metallic properties of the investigated materials. By inspecting valence electronic charge density, we can understand the charge polarization, bonding-nonbonding and electron affinity of the anion-cation pairs.

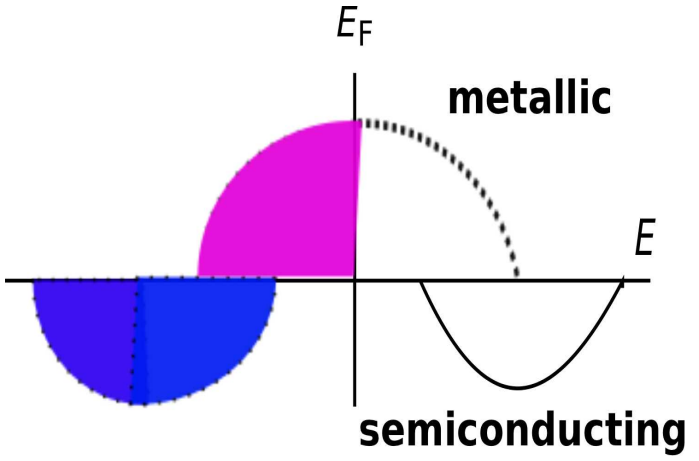

Fig. 1.1 Schematic view of a half metal. Upper (lower) panel denotes up spin (down spin) density of states. The Fermi energy E_F is shown by a vertical line.

The spin polarization (P) at the Fermi level E_F is defined by the ratio of the difference and the sum of the density of states (DOS) for up spin and down spin electrons, respectively, as

$$P = \frac{\left[D^{\uparrow}(E_F) - D^{\downarrow}(E_F)\right]}{\left[D^{\uparrow}(E_F) + D^{\downarrow}(E_F)\right]}, \tag{1.1}$$

where the arrows denote up and down spins. According to the sketch in Fig. 1.1, DOS at E_F in the minority spin direction is zero. Therefore, following eq. (1.1), a half metal is fully spin polarized at the Fermi level.

1.1 Research Chronology on Dilute Magnetic States

Dilute magnetic states (DMS) are realized as magnetic states at some dilute limit of magnetic impurities doped in semiconductors. The following legend lists up some representative works on DMS.

1998: Ohno [18] found Mn doped GaAs (group III-V) to be ferromagnetic with T_C=110 K.

1999: Ohno group [19] fabricated spin polarized light emitting diode (LED), a spintronics device, with Mn doped GaAs.

2000: Dietl team [20] theoretically studied ferromagnetic DMS and explain T_C in terms of Zener model.

2000: Akinaga team [21] experimentally confirmed half metallicity in thin film CrAs by MBE (molecular beam epitaxy) growth. The observed magnetic moment agreed well with the calculated one.

2000 onwards: about millions of papers are available in literature on wurtzite, zinc-blende, Heusler, semi-Heusler, and perovskite type DMS based study.

The experimental evidence on chalcopyrite type DMS mostly Mn doped in group II-IV-V_2 are listed below.

2000: Medvedkin group [22] observed ferromagnetic behaviors namely magnetic hysteresis loop, stripe domain pattern by magnetic force microscope (MFM) and magneto-optical kerr effect at room temperature, and therefore they claim a room temperature T_C in Mn doped $CdGeP_2$.

2002: Cho group [23] fabricated Mn doped $ZnGeP_2$ chalcopyrite and measured lattice parameter by Laue and powder X-ray diffraction (XRD) and measured Curie temperature by SQUID (superconducting quantum interference device) measurement and found T_C=312 K.

2003: Ishida group [24] again synthesized the same material like Cho group and obtained same Curie limit of 312 K in $ZnGeP_2$:Mn. They investigated electronic structures of the synthesized material using photoemission spectroscopy (PES).

2009: Asubar group [25] made Mn doped DMS in $ZnSnAs_2$, where the entire growth was monitored by reflection high-energy electron diffraction (RHEED) and achieved a FM transition temperature of 330 K.

2009: Koroleva team [26] measured magnetization with a SQUID magnetometer in the room temperature region, and they got T_C=325 K in Mn doped $ZnSiAs_2$ chalcopyrite as an advanced material for spintronics. They also measured lattice parameter of $ZnSiAs_2$ by XRD technique agreed with X-ray fluorescence measurements.

Therefore, fabricated Mn doped chalcopyrite type DMS (group II-IV-V_2) are evidence for exhibiting a Curie temperature higher than room temperature. We strongly expect a similar trend in the group I-III-VI_2 case. Yet many rooms are available to get a full fledge experimental picture for $3d$ TM doped at group II-IV-V_2 and group I-III-VI_2 based chalcopyrites.

1.2 Dilute Ferromagnetic States

DMS, especially ferromagnetic half metals (FHM) have attracted much attention because of full spin polarization for spintronic applications. The existence of FHM was first proposed by de Groot *et al.* [2] based on half-Heusler alloy NiMnSb by *ab-initio* electronic structure calculation. Lately several groups have attempted both experimentally and theoretically [18-30] to obtain room-temperature DMS based on compound semiconductors *viz.* zinc-blende, wurtzite, perovskite, and chalcopyrite compounds. Despite such efforts on DMS and metallic ferromagnets, the availability of room-temperature FHM is still at a preliminary stage. Therefore, to design a new type of FHM exhibiting higher Curie temperature than room temperature is yet intriguing.

Exciting features of FHM are as follows: (i) they have perfect spin polarization at the Fermi level, (ii) they often exhibit high magnetic transition temperature [27], (iii) they are asymmetric in spin orientation and used for electrical spin injection and spin transport, and (iv) they are utilized for spin coherence and decoherence in nanostructures by optical pulse [1]. These features indicate the suitability of FHM for the next-generation spintronic and opto-electronic applications.

There exist several attempts on the electronic structure calculations of pure chalcopyrite semiconductors [31], self-mixing of cations and anions among with different pure chalcopyrite semiconductors [32], and the system doped with TM [27], where the primal subject was to find magnetic properties and ferromagnetic states. In the present study, the investigation of stable magnetic phases and half metallicity by doping impurity in chalcopyrite semiconductors is given *a priori*. Copper and silver based chalcopyrite

semiconductors can be some suitable candidates to design FHM for wider energy gaps.

In this study, we investigate DMS and half metallicity by doping $3d$ TM at Al^{3+} and In^{3+} site of chalcopyrite hosts $CuAlSe_2$, $AgAlSe_2$, $AgAlS_2$ and $CuInS_2$ which are a group I-III-VI_2 based nonmagnetic and direct band-gap semiconductors. Invoking the solubility limit [18], we keep the doped level of TM ions at a low concentration. So far no experimental evidence is reported on the present I-III-VI_2 chalcopyrite type DMS. In doped cases ferromagnetic states are produced by the locally developed magnetic moments of impurities. To affirm the stability of the magnetic phases, we calculate the disordered spin moment (DSM) state, which is a random orientation of local spins of the magnetic ions. The lower energy phase is assumed to be the ground state magnetic configuration by ordering or disordering the spin moments. Some of them exhibit a stable ferromagnetic [27] and half metallic phase. We also calculate the core, valence and total hyperfine fields (HF) at the impurity sites in various TM doped compounds for future experimental works.

1.3 Dilute Antiferromagnetic States

The ternary compounds based on the chalcopyrite phase are used to design rather novel class magnetic materials by codoping $3d$ TM. We obtain ferrimagnetic (FiM) or antiferromagnetic (AF) states depending on the spin ordering and net magnetizations. In some compounds, the conduction electrons at the Fermi level are fully spin polarized and exhibit an elating key features of half metallicity. AF half metals (AFHM) [3] maintain a net compensated magnetization and keeping the local spin moments antiparallel. This happens as a special case of FiM state, where the possibility is that the system becomes half metallic and yet carries no net magnetization. Materials having such properties can be used for spin injection devices, non-volatile MRAM, spin FET and so on [1,19].

The existence of AFHM was first pointed out by van Leuken and de Groot [3] on semi-Heusler alloys CrMnSb and $V_{0.875}Mn_{0.125}FeSb_{0.875}In_{0.125}$ by first-principles electronic

structure calculation. Since then numerous attempts have been exploited to obtain room temperature DMS on groups III-V, II-VI, II-IV-V_2 and I-III-VI_2 based compound semiconductors both experimentally and theoretically [19-36]. Although some reports are found on DMS and half metallic ferromagnet, still the quest for room temperature AFHM is at a preliminary stage. We motivated to design rather promising AFHM and select group I-III-VI_2 based compounds Cu(AlXY)Se_2, Ag(AlXY)Se_2, Ag(AlXY)S_2 and Cu(InXY)S_2, where X and Y are $3d$ TM, which are chosen such that they have total sixteen valence electrons or ten effective valence d electrons [34-36]. We report electronic structures and discuss their magnetic and other favorable physical properties.

AFHM consists at least two types of magnetic ions with local spin moments aligned antiparallel, in contrast to the FHM which can be manifested by one type of magnetic ion. AFHM might have specific use compare to the FHM for the following reasons: (i) Sometimes they give higher magnetic transition temperatures than room temperature. (ii) They are insensitive to external fields due to zero net magnetization. (iii) Spin injections are rather easy to them because of their magnetic anisotropy [34,35]. These points imply that AFHM are favorable for spintronics application.

In this study, we calculate the ground state FiM and AF states of the codoped chalcopyrites relative to the spin disordered state. DSM states often become lower in total energy by super-exchange coupling. We find room temperature AFHM by codoping TM at the host matrix. The target materials exhibit half metallic DOS, full spin polarization and magnetic critical temperatures above room temperature. The materials stability can be verified by calculating the enthalpy of formation. Some instable phases become stable at a high entropic state.

HF at the magnetic impurity sites are directly proportional to the s electron spin density difference of up- and down spins at the nuclear position. HF are mostly linear to the corresponding local spin moments. Induced HF at the neighboring sites arises from the polarization of the core and valence electrons, which give an asymptotic tails of s wave function. Leading contribution to HF comes from the Fermi contact interaction of the nuclear magnetic moment due to nuclear spin and core electrons.

1.4 Goals of Present Study

Theoretically investigated TM doped Chalcopyrites in the Ref. [27] describe metallic FM states where undistorted structure was assumed and in the Ref. [34] AF state was calculated, but having relatively large net moment the magnetic states seem to be FiM with Curie temperature, rather than AF with Néel temperature. Therefore, from the above numerical analyses we infer to focus on: (i) to consider the proper structure (distorted) parameter in calculation. (ii) to explore ferromagnetic half metallicity, its stability and high T_C. (iii) to generalize the concept of DMS. (iv) to address the proper FiM and AF states with Curie and Néel temperatures, respectively. (v) to explain the mechanisms of magnetic stability in details for chalcopyrite-type DMS.

Since the inception of spin based electronics i.e., the discovery of giant magnetoresistive (GMR) effect [1] has drawn much attention to fabricate GMR based magnetoelectronics devices, for instance spin valve, magnetic tunnel junction, GMR heads, and so on. In such devices, alternate layers of nonmagnetic, FM and AF materials are used and the resistance of magnetic materials are lowest for parallel set up of local spin moments and highest for antiparallel order of spins. Therefore, we realized that novel class magnetic half metals are needed for the future spintronics and material science applications. Another crucial point is to operate them at room temperature. To serve such purposes, we select I-III-VI_2 chalcopyrites as host materials because chalcopyrite-type DMS are expected to give high T_C for practical applications. The goals in the present study are as follows:

(i) Materials design for novel class ferromagnetic and antiferromagnetic half metals.

(ii) Finding stable magnetic states having critical temperatures higher than room temperature.

(iii) Calculating several magnetic properties to understand the underlying stability mechanisms.

Therefore, we anticipate that computational materials design for FHM and AFHM might encourage experimentalists and those materials can be a substitute for the next-generation spin based electronics and optoelectronics applications.

The layout of the dissertation is organized in the following way. In chap. 2, a brief derivation of the underlying formalisms are given. Electronic structures and electronic properties of the host chalcopyrite semiconductors are discussed in chap. 3. Chapter 4 is planned to describe the FHM with underlying mechanisms and coupling schemes. Calculated magnetic properties are explained here. Chapter 5 is set by the computation of AFHM. In addition FM, FiM and spin disordered phases are described. HF in half metallic states are discussed too in this chapter. The dissertation is summarized in chap. 6 with remarks on the results. Outlooks explain the extension of the present work. Following the summary appendices have been added. A reference section is included at the end of each chapter.

1.5 References

[1] S.A. Wolf, D.D. Awschalom, R.A. Buhrman, J.M. Daughton, S. von Molnár, M.L. Roukes, A.Y. Chtchelkanova, D.M. Treger, Science **294**, 1488 (2001).

[2] R.A. de Groot, F.M. Mueller, P.G. van Engen and K.H.J. Buschow, Phys. Rev. Lett. **50**, 2024 (1983).

[3] H. van Leuken and R.A. de Groot, Phys. Rev. Lett. **74**, 1171 (1995).

[4] J. Korringa, Physica **13**, 392 (1947).

[5] W. Kohn and N. Rostoker, Phys. Rev. **94**, 1111 (1954).

[6] J.C. Slater, Phys. Rev. **51**, 846 (1937).

[7] O.K. Andersen, Phys. Rev. B **12**, 3060 (1975).

[8] D.D. Koelling and G.O. Arbman, J. Phys. F: Metal Phys. **5**, 2041 (1975).

[9] M. Weinert, J. Math. Phys. **22**, 2433 (1981).

[10] P. Hohenberg and W. Kohn, Phys. Rev. **136**, B864 (1964).

[11] W. Kohn and L.J. Sham, Phys. Rev. **140**, A1133 (1965).

[12] V.L. Moruzzi, J.F. Janak and A.R. Williams, Calculated Electronic Properties of Metals (Pergamon, New York, 1978).

[13] J.P. Perdew and Y. Wang, Phys. Rev. B **45**, 13244 (1992).

[14] C. Takahashi, M. Ogura and H. Akai, J. Phys: Condens. Matter **19**, 365233 (2007).

[15] M. Ogura, C. Takahashi and H. Akai, J. Phys: Condens. Matter **19**, 365226 (2007).

[16] H. Shiba, Prog. Theor. Phys. **46**, 77 (1971).

[17] M. Ogura and H. Akai, J. Phys: Condens. Matter **19**, 365215 (2007).

[18] H. Ohno, Science **281**, 951 (1998).

[19] Y. Ohno, D.K. Young, B. Beschoten, F. Matsukura, H. Ohno, and D.D. Awschalom, Nature **402**, 790 (1999).

[20] T. Dietl, H. Ohno, F. Matsukura, J. Cibert, and D. Ferrand, Science **287**, 1019 (2000).

[21] H. Akinaga, T. Manago, and M. Shirai, Jpn. J. Appl. Phys. **39**, L1118 (2000).

[22] G.A. Medvedkin, T. Ishibashi, T. Nishi, K. Hayata, Y. Hasegawa, and K. Sato, Jpn. J. Appl. Phys. **39**, L949 (2000).

[23] S. Cho, S. Choi, G.B. Cha, S.C. Hong, Y. Kim, Y.J. Zhao, A. J. Freeman, J.B. Ketterson, B.J. Kim, Y.C. Kim, and B.C. Choi, Phys. Rev. Lett. **88**, 257203 (2002).

[24] Y. Ishida, D.D. Sarma, K. Okazaki, J. Okabayashi, J.I. Hwang, H. Ott, A. Fujimori, G.A. Medvedkin, T. Ishibashi, and K. Sato, Phys. Rev. Lett. **91**, 107202 (2003).

[25] J.T. Asubar, Y. Jinbo, and N. Uchitomi, J. Cryst. Growth **311**, 929 (2009).

[26] L.I. Koroleva, D.M. ZashchirinskiĬ, T.M. Khapaeva, S.F. Marenkin, I.V. Fedorchenko, R. Szymczak, B. Krzumanska, V. Dobrovol'skiĬ, and L. KilanskiĬ, Phys. Solid State, **51**, 303 (2009).

[27] T. Kamatani and H. Akai, Mater. Sci. Semicond. Process. **6**, 389 (2003).

[28] H. Akai, Phys. Rev. Lett. **81**, 3002 (1998).

[29] K. Sato and H. Katayama-Yoshida, Semicond. Sci. Technol. **17**, 367 (2002).

[30] K.W. Edmonds, K.Y. Wang, R.P. Campion, A.C. Neumann, C.T. Foxon, B.L. Gallagher, and P.C. Main, Appl. Phys. Lett. **81**, 3010 (2002).

[31] J.E. Jaffe and A. Zunger, Phys. Rev. B **28**, 5822 (1983).

[32] S.H. Wei and A. Zunger, J. Appl. Phys. **78**, 3846 (1995).

[33] B.L. Gyorffy, A.J. Pindors, J. Staunton, G.M. Stocks, and H. Winter, J. Phys. F: Met. Phys. **15**, 1337 (1985).

[34] M. Ogura, Y. Hashimoto and H. Akai, Phys. Status Solidi c **3**, 4160 (2006).

[35] H. Akai and M. Ogura, Phys. Rev. Lett. **97**, 026401 (2006).

[36] L. Bergqvist and P.H. Dederichs, J. Phys.: Condens. Matter **19**, 216220 (2007).

Chapter 2

Theory

Korringa-Kohn-Rostoker (KKR) Green's function and full-potential linearized augmented plane wave (FLAPW) are among the efficient electronic structure calculation methods. Basically KKR is a multiple scattering theory and relatively faster than FLAPW, whereas FLAPW is more reliable and precise than KKR in a full-potential scheme. Both are all-electron first-principles calculation approach based on density functional theory [1,2] for electronic structures and other physical properties of crystals.

2.1 Many-Body Hamiltonian : Born-Oppenheimer Approximation

The full Hamiltonian for a large number of interacting electrons and ions (nuclei) is given below as the sum of electrons kinetic part, electron-electron interaction, electron-nuclei interaction, nuclei kinetic part and nuclei-nuclei interaction, respectively.

$$H = T_e + V_{ee} + V_{en} + T_n + V_{nn} \tag{2.1}$$

$$\therefore \quad H = \sum_i \frac{p_i^2}{2m} + \frac{1}{2}\sum_{i\neq j} \frac{e^2}{|r_i - r_j|} - \sum_{i,n} \frac{Z_n e^2}{|r_i - R_n|} + \sum_n \frac{P_n^2}{2M_n} + \frac{1}{2}\sum_{n\neq m} \frac{Z_n Z_m e^2}{|R_n - R_m|} \tag{2.2}$$

$$H = \frac{-\hbar^2}{2m}\sum_i \nabla_i^2 + \frac{1}{2}\sum_{i\neq j} \frac{e^2}{|r_i - r_j|} - \sum_{i,n} \frac{Z_n e^2}{|r_i - R_n|} - \sum_n \frac{\hbar^2}{2M_n}\nabla_n^2 + \frac{1}{2}\sum_{n\neq m} \frac{Z_n Z_m e^2}{|R_n - R_m|} \tag{2.3}$$

where $i,\ j$ stand for electronic index and n, m for ionic index, and $T_e = \frac{-\hbar^2}{2m}\sum_i \nabla_i^2$, $V_{ee} = \frac{1}{2}\sum_{i\neq j}\frac{e^2}{|r_i - r_j|}$, $V_{en} = -\sum_{i,n}\frac{Z_n e^2}{|r_i - R_n|}$, $T_n = -\sum_n \frac{\hbar^2}{2M_n}\nabla_n^2$, and $V_{nn} = \frac{1}{2}\sum_{n\neq m}\frac{Z_n Z_m e^2}{|R_n - R_m|}$

For many electron atomic, molecular or solid system, the time-independent and non-relativistic Schrödinger wave equation is given by

$$H\Psi = E\Psi \tag{2.4}$$

$$\Rightarrow \Big(H_e + T_n + V_{nn}\Big)\,\psi\Big(\{r_i\},\{R_n\}\Big)\phi\Big(\{R_n\}\Big) = E\,\psi\Big(\{r_i\},\{R_n\}\Big)\,\phi\Big(\{R_n\}\Big) \tag{2.5}$$

where $H_e = T_e + V_{ee} + V_{en}$ is the electronic part of the full Hamiltonian and E is the total energy and the full wave function Ψ is the product of two wave functions as $\psi\Big(\{r_i\},\{R_n\}\Big)\,\phi\Big(\{R_n\}\Big)$ according to the electronic and nuclei coordinates. For brevity, hereinafter we omitted the explicit coordinate dependency. Now (2.5) can be rewritten as

$$H_e\,\psi\phi + (T_n + V_{nn})\psi\phi = E\,\psi\phi \tag{2.6}$$

$$\Rightarrow E_e\,\psi\phi + T_n\psi\phi + V_{nn}\psi\phi = E\,\psi\phi \tag{2.7}$$

$$\Rightarrow E_e\,\psi\phi - \sum_n \frac{\hbar^2}{2M_n}\Big[\nabla_n\cdot\nabla_n\psi\phi\Big] + V_{nn}\psi\phi = E\,\psi\phi \tag{2.8}$$

$$\Rightarrow E_e\,\psi\phi - \sum_n \frac{\hbar^2}{2M_n}\Big[\underbrace{\phi\nabla_n\cdot\nabla_n\psi + 2\nabla_n\phi\cdot\nabla_n\psi}_{\text{tricky terms}} + \psi\nabla_n\cdot\nabla_n\phi\Big] + V_{nn}\psi\phi = E\,\psi\phi \tag{2.9}$$

where the second and third terms (essential for electron-phonon coupling) in the left side of (2.9) are the nuclei kinetic parts acting on electronic coordinates. These parts are too demanding to solve numerically. In addition, the inverse of nuclei mass is quite smaller than its electronic counterpart and therefore can be treated as a perturbation. Thus omission of these terms is known as Born-Oppenheimer approximation (BOA) [3] or adiabatic approximation. In the BOA the left equation is

$$E_e\,\psi\phi - \sum_n \frac{\hbar^2}{2M_n}\Big[\psi\nabla_n\cdot\nabla_n\phi\Big] + V_{nn}\psi\phi = E\,\psi\phi \tag{2.10}$$

$$\therefore\quad E_e\,\phi + T_n\phi + V_{nn}\phi = E\,\phi \tag{2.11}$$

$$\Rightarrow T_n\phi + (E_e\ + V_{nn})\phi = E\,\phi \tag{2.12}$$

where the bracketed sum is known as the Born-Oppenheimer potential, which is nothing but the calculated total energy in a crystal system at frozen nuclei. This is rather ease

to solve in only nuclei coordinates. Still we have to deal with nuclei motion to obtain the stability of the assumed structure and the ground state total energy for full Hamiltonian.

Nuclei terms can be solved explicitly or can be added as a parameter in the electronic Hamiltonian. Hence onwards we deal with electronic Hamiltonian:

$$H_e = \frac{-\hbar^2}{2m}\sum_i \nabla_i^2 + \frac{1}{2}\sum_{i\neq j}\frac{e^2}{|r_i - r_j|} - \sum_{i,n}\frac{Z_n e^2}{|r_i - R_n|} \tag{2.13}$$

Adopting Rydberg atomic units ($\hbar^2 = 1$, e^2=2, and $m = 1/2$) the Schrödinger equation, central to the theory of electronic structure calculations is

$$H_e\,\psi\Big(\{r_i\},\{R_n\}\Big) = E_e\Big(\{R_n\}\Big)\,\psi\Big(\{r_i\},\{R_n\}\Big) \tag{2.14}$$

$$\Rightarrow \Big[-\sum_i \nabla_i^2 + \sum_{i\neq j}\frac{1}{|r_i - r_j|} - \sum_{i,n}\frac{2Z_n}{|r_i - R_n|}\Big]\,\psi = E_e\,\psi \tag{2.15}$$

The dependence of the eigenvalues E_e on the nuclear positions is taken into account. The energy $E_e(\{R_n\})$ is called the adiabatic contribution of the electrons to the energy of the system. The remaining non-adiabatic terms contribute very little to the energy. If the nuclei are static in position then nuclei coordinates are no more variable and for N electron system with an external potential $\mathrm{V_{ext}}$ the Schrödinger equation is given by

$$\Big[-\sum_i^N \nabla_i^2 + \sum_{i\neq j}^N \frac{1}{|r_i - r_j|} + \sum_i^N V_{\mathrm{ext}}(r_i)\Big]\,\psi\Big(\{r_i\}\Big) = E_e\,\psi\Big(\{r_i\}\Big) \tag{2.16}$$

2.2 Density Functional Theory

Before development of the density functional theory (DFT), there was functional limitations to treat the inhomogeneous interacting electron systems e.g., atoms, molecules and solids for huge number of coordinates having the systems. DFT makes the job easy by ascribing a fundamental variable electron density, which drastically reduce the $3N$ coordinates of many electron system into only 3 coordinates, as a result the many body systems become tractable in practice. The basic formalism in DFT is based on two theorem proven by Hohenberg and Kohn [1]. First, the ground state (say nondegenerate) of an inhomogeneous interacting electron system is the functional of the electron density. External potential (electron-ion interaction) V_{ext}(r) is a unique functional of the electron

density n(r). Second, the total energy functional is minimum for a true (exact) electron density [4]. Interested readers can see the proofs elsewhere. DFT is invalid for a system having degenerate ground states.

Above many-body Schrödinger equation (2.16) is practically intractable owing to $3N$ coordinates to be dealt with. This crucial point is handled by DFT by imposing a basic variable function known as electron density having only 3 coordinates and thus the many-body problem is tractable in practice. In operator form we can write the electronic Hamiltonian operator as

$$\hat{H}_e = \hat{T} + \hat{U} + \hat{V} \tag{2.17}$$

Hence total energy is the expectation value of the Hamiltonian operator with respect to the ground state wave function of electron:

$$E_e = (\psi, \hat{H}_e\psi) = (\psi, \hat{T}\psi) + (\psi, \hat{U}\psi) + (\psi, \hat{V}\psi) \tag{2.18}$$

where U includes all Coulombic interactions and V is the external potential produced by the static nuclei. We define a density operator as

$$\hat{n}(r) = \sum_i \delta(r - r_i) \tag{2.19}$$

and the electron density is

$$n(r) = (\psi, \hat{n}(r)\psi) \tag{2.20}$$

so the external potential is given by

$$V = (\psi, \hat{V}\psi) = (\psi, \sum_i V_{\text{ext}}(r_i)\psi) = \int dr_1, dr_2, ..., dr_N \psi^* \sum_i V_{\text{ext}}(r_i)\psi \tag{2.21}$$

$$V = \int dr \int dr_1, dr_2, ..., dr_N \psi^* \sum_i \delta(r - r_i) V_{\text{ext}}(r)\psi \tag{2.22}$$

$$V = \int dr V_{\text{ext}}(r) \int dr_1, dr_2, ..., dr_N \psi^* \hat{n}(r)\psi = \int dr V_{\text{ext}}(r)(\psi, \hat{n}(r)\psi) \tag{2.23}$$

$$V = \int dr V_{\text{ext}}(r) n(r) \Rightarrow V = V[n(r)] \tag{2.24}$$

where the delta function relation $V_{\text{ext}}(r_i) = \int dr \sum_i \delta(r - r_i) V_{\text{ext}}(r)$ is used and we see that external potential is a functional of electron density. In terms of this electron density

the total (electronic) energy functional in the Kohn-Sham attempt can be written as

$$E_{\mathrm{KS}}[n] = V_{\mathrm{ext}}[n] + V_{\mathrm{H}}[n] + G[n] \tag{2.25}$$

$$G[n(r)] \equiv T_{\mathrm{s}}[n] + E_{\mathrm{xc}}[n] \tag{2.26}$$

where $G[n]$ is a global energy functional defined as the sum of kinetic energy functional for single electron or non-interacting system of electrons and exchange-correlation (XC) energy functional for an interacting system of electrons. The additional XC term was absent in the Hartree or Hartree-Fock approximation. The time-independent and non-relativistic one electron Kohn-Sham equation is given by

$$H_{\mathrm{KS}}\psi_i(r) = \epsilon_i\psi_i(r) \tag{2.27}$$

where ϵ_i is the single orbital electron energy and

$$n(r) = \sum_{i=1}^{occ} |\psi_i(r)|^2 \tag{2.28}$$

is the electron density (statistical approach) summed up to the occupied orbitals. Thus the set of N one-electron equations can be written as

$$\Big[-\nabla^2 + V_{\mathrm{KS}}(r) \Big] \psi_i = \varepsilon_i \, \psi_i \tag{2.29}$$

where

$$V_{\mathrm{KS}}(r) = V_{\mathrm{H}}(r) + V_{\mathrm{ext}}(r) + V_{\mathrm{xc}}(r) \tag{2.30}$$

is the Kohn-Sham effective interaction energy, provided the many electron XC potential is given by the functional derivative (a derivation is given in **Appendix B**) of the XC energy functional as

$$V_{\mathrm{xc}}(r) = \frac{\delta E_{\mathrm{xc}}[n(r)]}{\delta n(r)} \tag{2.31}$$

Under certain conditions the XC energy functional for a system of N electrons which behave like a uniform electron gas can be rather accurately calculated as

$$\frac{E_{\mathrm{xc}}[n]}{N} = \epsilon_{\mathrm{xc}}(n) \tag{2.32}$$

The general form of $E_{\mathrm{xc}}[n]$ can be written as

$$E_{\mathrm{xc}}[n] = \int n(r)\epsilon_{\mathrm{xc}}[n(r)]dr \tag{2.33}$$

where $\epsilon_{\rm xc}$ at r depends on the shape of electron density $n(r)$ everywhere.

In the local spin density approximation (LSDA), an inhomogeneous electron system is regarded as a locally homogeneous with uniform electron density $n(r)$:

$$E_{\rm xc}^{\rm LSDA}[n] \approx \int \Big(n_\uparrow(r) + n_\downarrow(r)\Big)\epsilon_{\rm xc}^{\rm h}\Big(n_\uparrow(r) + n_\downarrow(r)\Big)dr \tag{2.34}$$

where $\epsilon_{\rm xc}^{\rm h}(n)$ is the XC contribution to the total energy (per electron) of a homogeneous, but interacting, electron gas of density $n(r)$. The function $\epsilon_{\rm xc}^{\rm h}(n)$ is itself known only approximately. Therefore, the XC potential is given by

$$V_{\rm xc}^{\rm LSDA}(r) \approx \epsilon_{\rm xc}^{\rm h}\Big(n_\uparrow(r) + n_\downarrow(r)\Big) + \Big(n_\uparrow(r) + n_\downarrow(r)\Big)\frac{\partial\epsilon_{\rm xc}^{\rm h}\Big(n_\uparrow(r) + n_\downarrow(r)\Big)}{\partial\Big(n_\uparrow(r) + n_\downarrow(r)\Big)} \tag{2.35}$$

where $\epsilon_{\rm xc}^{\rm h}$ at r only depends on the density at r and rather exact for homogeneous electron gas.

Generalized gradient approximation (GGA) is obtained by including the gradient terms to LSDA as

$$E_{\rm xc}^{\rm GGA}[n] \approx \int \Big(n_\uparrow(r) + n_\downarrow(r)\Big)\epsilon_{\rm xc}^{\rm h}\Big((n_\uparrow(r) + n_\downarrow(r)), \nabla(n_\uparrow(r) + n_\downarrow(r)), ...\Big)dr \tag{2.36}$$

where $\epsilon_{\rm xc}^{\rm h}$ at r depends on the density and its gradient (+ higher terms)

Finally in the LSDA the KS orbital equations for one electron can be written by

$$\Big[-\nabla^2 + V_{\rm ext}(r) + \int \frac{n(r')}{|r-r'|}dr' + V_{\rm xc}^{\rm LSDA}(r)\Big]\,\psi_i = \varepsilon_i\psi_i \tag{2.37}$$

2.3 KKR-Green's Function

Assume the Green's function (GF) (a definition is given in **Appendix B**) of a periodic assembly of central potentials. The potential is given by

$$V(r + R^i) = V^i(r) \tag{2.38}$$

where the atomic position in the crystal is defined by the lattice vector R^i (period) and the Green's function in atomic units is defined as

$$\Big[-\nabla^2 + V^i(r) - E\Big] G(r + R^i, r' + R^j, E) = -\delta_{ij}\, \delta(r - r') \tag{2.39}$$

For $i \neq j$ the GF satisfies the homogeneous Schrödinger equation and the full wave function (here GF) can be expanded in the regular solutions $R^i_L(r, E)$ and $R^j_L(r, E)$ of the Schrödinger equation. In the muffin-tin spherical potential approximation, the solutions are given as the product of radial part and spherical harmonics, $R^i_L(r, E) = R^i_\ell(r, E)Y_L(r)$ The radial wavefunctions $R^i_\ell(r, E)$ satisfy the radial Schrödinger equation:

$$\Big[-\frac{1}{r}\frac{\partial^2}{\partial r^2} r + \frac{\ell(\ell+1)}{r^2} + V^i(r) - E\Big] R^i_\ell(r, E) = 0 \tag{2.40}$$

and $Y_{\ell m}(\theta, \varphi)$ are the spherical harmonics defined to be the eigenfunctions of L^2 and L_z

$$\hat{L}^2 Y_{\ell m}(\theta, \varphi) = L^2 Y_{\ell m}(\theta, \varphi) = \hbar^2 \ell(\ell+1) Y_{\ell m}(\theta, \varphi) \tag{2.41}$$

$$\hat{L}_z Y_{\ell m}(\theta, \varphi) = L_z Y_{\ell m}(\theta, \varphi) = m\hbar Y_{\ell m}(\theta, \varphi) \tag{2.42}$$

The Laplace spherical harmonics are generally defined as

$$Y_{\ell m}(\theta, \varphi) = \left[\frac{(2\ell+1)}{4\pi} \frac{(\ell - |m|)!}{(\ell + |m|)!} \right]^{\frac{1}{2}} P_\ell^{|m|}(\cos\theta) e^{im\varphi} \tag{2.43}$$

which is normalized to unity

$$\int_{\theta=0}^{\pi} \sin\theta d\theta \int_{\varphi=0}^{2\pi} d\varphi \Big| Y_{\ell m}(\theta, \varphi) \Big|^2 = 1 \tag{2.44}$$

where $P_\ell^m(\cos\theta)$ are associated Legendre polynomials.

For $i = j$ the Green's function for a central potential with a boundary condition of back (multiple) scattering by all other potential in the crystal is given by

$$G(r, r', E) = -i\sqrt{E} \sum_L R_\ell(r_<, E) H_\ell(r_>, E) Y_L(\hat{r}) Y_L(\hat{r}') \tag{2.45}$$

$$\equiv \sum_L G_\ell(r, r', E) Y_L(\hat{r}) Y_L(\hat{r}') \tag{2.46}$$

where R_ℓ (regular, *i.e.*, converging at $r \to 0$) and H_ℓ (irregular, *i.e.*, diverging at $r \to 0$) are two linearly independent solutions of the radial equation.

In the mixed site the crystal Green's function in angular momentum (cell-centered) representation is the sum of single site GF plus multiple (back) scattering term: $G = G_s + G_m$ where the single site GF for a single MT potential V^i at i^{th} site is given by

$$G_s^i(r, r', E) = -i\sqrt{E}\sum_L R_L^i(r_<, E)H_L^i(r_>, E) \tag{2.47}$$

where we define $R_L(r, E) = j_\ell(\sqrt{E}r)Y_L(\hat{r})$ and $H_L(r, E) = h_\ell^{(1)}(kr)Y_L(\hat{r})$ in terms of the spherical Bessel and Hankel functions, respectively. The crystal GF is given by

$$G(r + R^i,\, r' + R^j,\, E) = \underbrace{\sum_{LL'} R_L^i(r, E)\, G_{LL'}^{ij}(E) R_{L'}^j(r', E)}_{\text{homogeneous part}} + \underbrace{\delta_{ij}\sum_L R_L^i(r_<, E)H_L^i(r_>, E)}_{\text{heterogeneous part}} \tag{2.48}$$

where $L \equiv (\ell m)$ are angular momentum indices, $r_<$ ($r_>$) is the shorter (longer) of the radii r and r' and $R_L^i(r, E)$ and $H_L^i(r, E)$ are properly normalized regular and irregular scattering solutions corresponding to the potential centered at position R_i. The inhomogeneous part is the single site expansion of the partial waves. The homogeneous part of GF matrix $G(E) = \{G_{LL'}^{ij}(E)\}$ can be expressed at the following *algebraic Dyson equation* determining the structural Green's function, known as structure constants.

$$G = G^0 + G^0tG^0 + G^0tG^0tG^0 + ... = G^0(I - tG^0)^{-1} = (I - G^0t)^{-1}G^0 = G^0 + G^0tG \tag{2.49}$$

where the free-space (unperturbed system) or reference GF is $G^0(E) = \{G_{LL'}^{0,ij}(E)\}$ and the single-site t matrices $t(E) = \{t_{LL'}^i(E)\delta_{ij}\}$, which become diagonal in the angular momentum indices if muffin-tin potentials are used. For brevity, the explicit energy dependence of the matrices in (2.49) has been omitted and I denotes a unit matrix in the mixed site-angular-momentum representation.

In practice, the structural GF are first calculated in k space using matrix inversion, a Fourier transform returns the real space quantities.

$$G_{LL'}(k, E) = \sum_j G_{LL'}^{ij} e^{-\mathrm{ik}\cdot(\mathrm{R^i}-\mathrm{R^j})} \tag{2.50}$$

which is independent of site i for translational symmetry and in a periodic crystal we use the Bloch condition which imply that the amplitude of a scattered wave at position

R^i differs from the amplitude of a scattered wave at position R^j by a phase factor of $e^{-\mathrm{ik}\cdot(\mathrm{R^i}-\mathrm{R^j})}$. The structural GF, reference GF and t matrix are matrices in L and L' and is solved by matrix inversion after a cutoff at some $\ell = \ell_{max}$ for which the t matrix becomes negligible and the result is [5]

$$G^{ij}_{LL'}(E) = \frac{1}{\tau}\int_{\tau} dk\, e^{\mathrm{ik}\cdot(\mathrm{R^i}-\mathrm{R^j})}\Big[\Big(1 - G^0(k,E)t(E)\Big)^{-1} G^0(k,E)\Big]_{LL'} \tag{2.51}$$

where τ is the Brillouin zone volume. To calculate the charge density or the density of states, only the on-site term $i = j$, $G^{ii}_{LL'}(E)$ is needed. The crystal GF is then given by

$$G(r+R^i, r'+R^j, E) = \delta_{ij}\, G^i_s + \sum_{LL'} R^i_L(r,E)\left[\frac{1}{\tau}\int_{\tau} dk\, e^{\mathrm{ik}\cdot(\mathrm{R^i}-\mathrm{R^j})}\Big\{(1-G^0t)^{-1}G^0\Big\}_{LL'}\right] R^j_{L'}(r',E) \tag{2.52}$$

Note: The scattering-path operator, τ(E), can be defined as

$$\tau = \Big[t^{-1} - G^0\Big]^{-1} \tag{2.53}$$

which is related to the homogeneous part of Green's function matrix, (2.52) through

$$G = G^0 + G^0\tau G^0 = t^{-1}\tau t^{-1} - t^{-1} \tag{2.54}$$

In KKR-Green's function method, the major step is to calculate the crystal structure constants introduced in (2.52), which involves the inversion of an infinite matrix. However, if all the elements G^{ij} decay fast enough as the distance $|R^i - R^j|$ increases, then (2.52) can be solved for a finite assembly of atomic sites.

2.4 Density of States and Electron Density

The homogeneous form of one electron Kohn-Sham (KS) equation is $(E_i - \hat{H})\varphi_i$=0 where $\hat{H}$ is the Hamiltonian or total energy operator and φ_i is the KS eigenstate. The corresponding Green's function (a derivation is given in **Appendix B**) is given by

$$(z - \hat{H})G(r, r',\, z) = \delta(r - r') \tag{2.55}$$

where z is a complex energy parameter $z = E + i\varepsilon$. Expand G in terms of the eigenstates of Kohn-Sham equation:

$$G(r, r',\, z) = \sum_k c_k(r')\varphi_k(r) \tag{2.56}$$

where $c_k(r')$ is the expansion coefficient to be determined. Putting (2.56) into (2.55) one obtains

$$(z - \hat{H}) \sum_k c_k(r')\varphi_k(r) = \delta(r - r') \tag{2.57}$$

$$\sum_k c_k(r')(z - E_k)\varphi_k(r) = \delta(r - r') \tag{2.58}$$

Multiplying both sides by $\varphi_k^*(r)$, integrating and following the delta function properties

$$\int_{-\infty}^{\infty} f(x)\delta(x - a)dx = f(a) \tag{2.59}$$

where $\delta(x)$ is the Dirac delta function. we obtain

$$\sum_{k'} c_{k'}(r')(z - E_{k'}) \int dr\varphi_k^*(r)\varphi_{k'}(r) = \int dr\varphi_k^*(r)\delta(r - r') \tag{2.60}$$

$$\sum_{k'} c_{k'}(r')(z - E_{k'})\delta_{kk'} = \varphi_k^*(r') \tag{2.61}$$

$$c_k(r')(z - E_k).1 = \varphi_k^*(r') \tag{2.62}$$

$$c_k(r') = \frac{\varphi_k^*(r')}{(z - E_k)} \tag{2.63}$$

where Kronecker delta (not function) is defined as

$$\delta_{kk'} = \begin{pmatrix} 1, & for & k = k' \\ 0, & for & k \neq k' \end{pmatrix} \tag{2.64}$$

Hence putting back (2.63) into (2.56) we get the complex Green's function matrix as

$$G(r, r', z) = \sum_k \frac{\varphi_k^*(r')\varphi_k(r)}{(z - E_k)} = \sum_k \frac{\varphi_k^*(r')\varphi_k(r)}{(E - E_k + i\varepsilon)} \tag{2.65}$$

This follows from the Dirac identity,

$$\int_{-\infty}^{\infty} \frac{f(x)}{x - x_0 \pm i\varepsilon} dx = P\left[\int_{-\infty}^{\infty} \frac{f(x)}{x - x_0} dx\right] \mp i\pi \int_{-\infty}^{\infty} \delta(x - x_0)f(x)dx\,(= \mp i\pi f(x_0)) \tag{2.66}$$

where P stands for the Cauchy principal part of the integral.

$$G(r, r', E + i\varepsilon) = P\left[\sum_k \frac{\varphi_k^*(r')\varphi_k(r)}{(E - E_k)}\right] - i\pi \sum_k \varphi_k^*(r')\varphi_k(r)\delta(E - E_k) \tag{2.67}$$

In general eigenfunction and hence Green's function are complex in nature. Therefore at $r = r'$ case imaginary part of Green's function is

$$G(r, r', E + i\varepsilon) = -\pi \sum_k \varphi_k^*(r')\varphi_k(r)\delta(E - E_k) \tag{2.68}$$

where ε is a positive infinitesimal quantity. The density of states (DOS) $n(r, E)$ per unit energy E in the angular momentum (L) representation is obtained by the diagonal part of G with $r' = r$:

$$n(r, E) = \sum_k \left|\varphi_k(r)\right|^2 \delta(E - E_k) \tag{2.69}$$

and hence

$$n(r, E) = -\frac{1}{\pi}\Im G(r, r, E + i\varepsilon) \tag{2.70}$$

Electron density can be obtained by integrating DOS up to Fermi energy:

$$n(r) = -\frac{1}{\pi}\Im \int_{-\infty}^{E_F} G(r, r, E + i\varepsilon)dE \tag{2.71}$$

$$n(r) = -\frac{1}{\pi}\Im \int_{-\infty}^{E_F + i\varepsilon} G(r, r, z)dz = -\frac{1}{\pi}\Im \oint_C G(r, r, z)dz \tag{2.72}$$

$$n(r) = \int_{-\infty}^{E_F} \sum_k \left|\varphi_k(r)\right|^2 \delta(E - E_k)dE \tag{2.73}$$

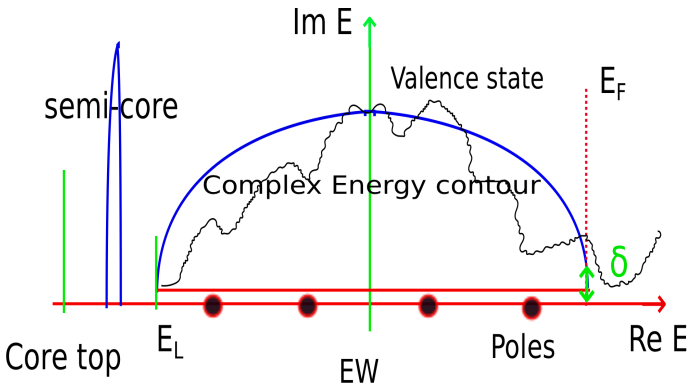

Fig. 2.1 Contour path integration of Green's function.

The energy contour for a complex energy integration is shown in **Fig.** 2.1. In practice, core states are very deep, semi-cores are bit shallower than cores and they are fully occupied discrete energy levels. The energy integration is preformed between the lower bound

(chosen at some sub-gap energy to avoid poles) of the valence band and the Fermi energy by adding a small imaginary part of energy. The core contributions of the electron charge density is added later. The imaginary part of the Green's function in equation (2.68) is a delta (spike) function and is unable to perform the integration literally. Therefore, to overcome this subtle, we perform contour integration for the complex energies (energy samplings) along the contour path.

The generalized Lloyd formula [6] for the electronic DOS can be written as

$$n(E) = n^0(E) + \frac{2}{\pi}\frac{d}{dE}\Im Tr\, ln\, T(E) \tag{2.74}$$

where $n(E)$ and $n^0(E)$ are the DOS of the system and the reference system, respectively and $T(E)$ is the t matrix of the system with respect to the reference system given by

$$T(E) = t\frac{1}{1 - G^0 t} \tag{2.75}$$

2.5 Muffin-Tin Form of Potential

In KKR-Green's function formalism, we can readily solve one electron Kohn-Sham equation using the muffin-tin (MT) shape potential at each atomic site. The electron density is assumed as the MT form, where the potential is finite inside a MT sphere mainly at the core or atomic region, and zero (constant) at the interstitial region. Therefore, at an atomic site a sphere of the radius $R_{\rm mt}$, called MT radius, the potential can be defined as follows

$$V_{\rm mt}(\mathbf{r}) = \left\{ \begin{array}{cc} \sum_i V_i\Big(|\mathbf{r} - \mathbf{R}_i|\Big)\,, & for \quad |\mathbf{r} - \mathbf{R}_i| \leq R_{\rm mt} \\ 0\,, & for \quad |\mathbf{r} - \mathbf{R}_i| > R_{\rm mt} \end{array} \right\} \tag{2.76}$$

where r is a distance from any arbitrary origin, R_i are atomic positions, $|\mathbf{r} - \mathbf{R}_i|$ are less than or equal to half the nearest-neighbor distance to become the spheres as inscribed and the sum covers the atomic assembly. A cluster of atoms which replicate the MT potentials is shown in **Fig.** 2.2. The schematic MT form of potentials are shown in **Fig.** 2.3 (a), whereas the actual crystal potentials are drawn in **Fig.** 2.3 (b) which is quite flat and finite (non-zero) in the **I** regions and very deep or diverging nature in the negative

axis of potential over the **C** regions. The crystal potential at any point is obtained by summing up the Coulombic terms over each charge of ions, and other electrons in the crystal. The average crystal potential acting on each electron is $U(r) = U_{\rm ion}(\rm r)+U_{\rm el}(\rm r)$.

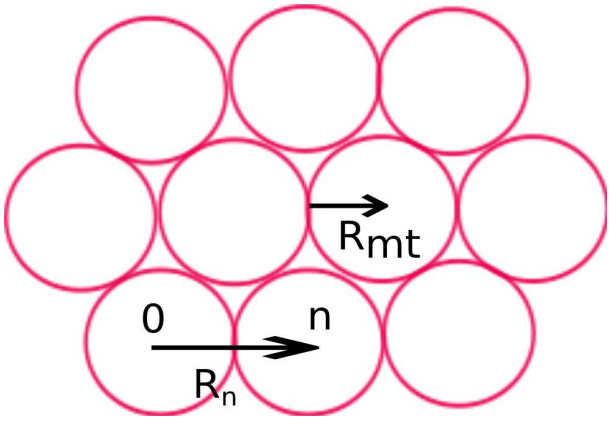

Fig. 2.2 A cluster of muffin-tin (MT) form of potentials in a crystal, $R_{\rm mt}$ is the radius of the MT sphere. $R_{\rm n}$ is the crystal translation (period) vector.

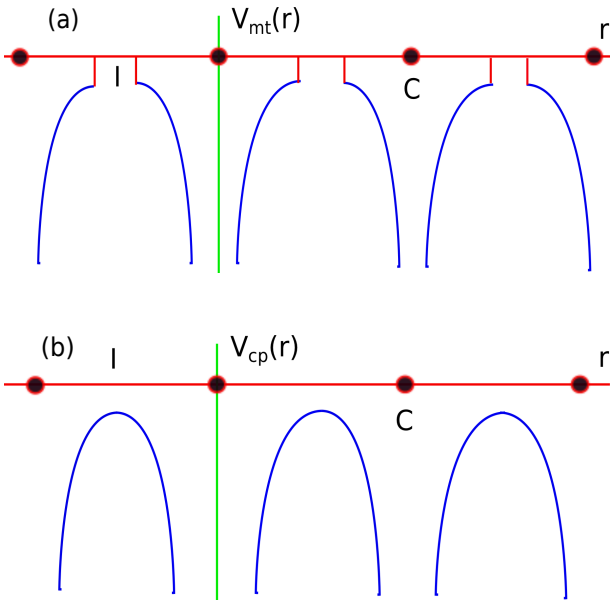

Fig. 2.3 (a) The muffin-tin potentials are sketched along a line of ions. It is zero in the interstitial (I) regions and very deep in each core (C) region. (b) The actual crystal potential (cp) is also drawn.

2.6 Coherent Potential Approximation

Coherent (effective) potential approximation (CPA), a concept of mean-field theory, is an efficient way to treat the doped system in KKR. In CPA disordered (aperiodic) system is regarded as a periodic array of average atom and determine the coherent t matrix at each site. CPA combined with Green's function gives an elegant approach to obtain the single-site scattering of the embedded atom in an effective medium. We take the configuration average of the possible configurations of doped systems. The effective medium is an array of atoms whose atomic potentials are specified by the coherent t matrix $\tilde{t}(E)$ of the MT potential. Once the coherent t matrix is obtained any ground state properties of the system can be known within the single site approximation.

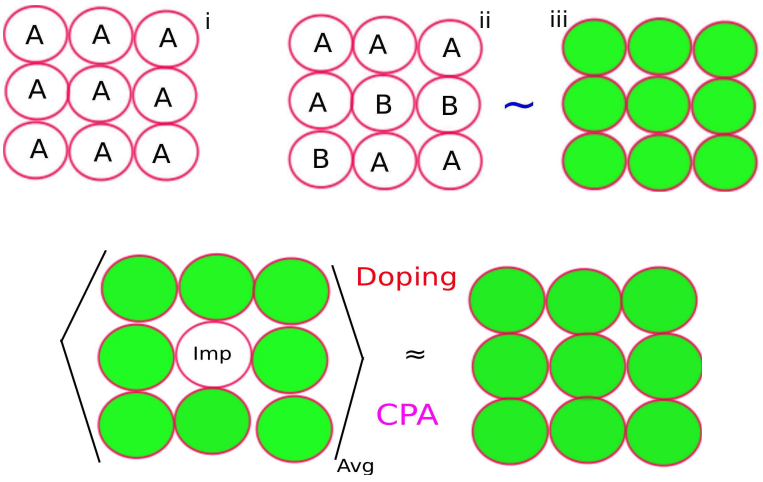

Fig. 2.4 Upper panel: i) a periodic solid of A atom, ii) some A atoms are substituted randomly by B atoms. The solid is now aperiodic, and iii) effective averaging over the sites. All A and B atoms are treated as same kind of atom. Lower panel: impurity doping and configuration average in coherent potential scheme.

To determine $\tilde{t}(E)$ consider a random alloy of impurity A or B atom embedded in the effective medium. The Green's function for the doped system is

$$G_{LL'}^{\mathrm{A(orB)}} = \sum_{L''} \tilde{G}_{LL''}^{00} \Big[1 - \Big(t_{\mathrm{A(orB)}} - \tilde{t}\Big)\tilde{G}^{00}\Big]_{L''L'}^{-1} \tag{2.77}$$

where $\tilde{G}^{00}_{LL'}$ is the back (multiple) scattering term for a host crystal with impurity sites A=B=0.

$$\tilde{G}^{00}_{LL'} = \int_{\tau} \frac{dk}{\tau} \tilde{G}_{LL'}(k) = \int_{\tau} \frac{dk}{\tau} \sum_{L''} g_{LL''}(k) \Big[1 - \tilde{t} g(k)\Big]^{-1}_{L''L'} \tag{2.78}$$

We determine the Green's function of the effective medium (periodic) by taking weighted average of the Green's function of the impurity atoms placed at the origin of the host medium (see **Fig.** 2.5).

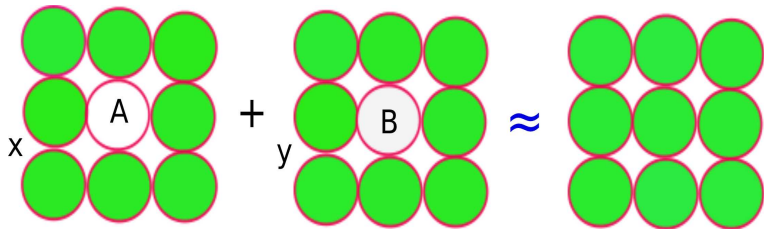

Fig. 2.5 Random mixing of impurity at host medium sites.

The cluster of green spheres (right) represents an effective average medium and the equation denotes that the weighted average over the sites A and B with concentration x and y is equal to the CPA average, as shown in **Fig.** 2.5. This leads a complex CPA potential in Green's function representation after solving the coherent t matrix iteratively. The self-consistency condition for $\tilde{t}$ is [7]

$$x\Big[t_A^{-1} - \tilde{t}^{-1} + \tilde{S}^{-1}\Big]^{-1} + y\Big[t_B^{-1} - \tilde{t}^{-1} + \tilde{S}^{-1}\Big]^{-1} = \tilde{S} \tag{2.79}$$

where $t(\omega)$ is the t matrix of each muffin-tin potential (ω is an energy parameter) and $\tilde{S}$ is defined as a propagator in an effective medium (a matrix in the $L = (\ell, m)$ representation):

$$\tilde{S} = \int_{\tau} \frac{dk}{\tau} \Big[\tilde{t}^{-1} - G(k)\Big]^{-1} \tag{2.80}$$

where τ is the Brillouin zone volume and $G(k)$ is the k-space structural Green's function. The set of equations in truncation series of L (s, p, and d states) must be solved iteratively. Once one obtained the coherent (average or effective) t matrix the other local and total quantities can be calculated accordingly.

2.7 Breit Integral

We define the Hamiltonian of hyperfine interaction with the spherical tensor operators T_n and T_e of rank one acting on the nuclear and electronic subspace, respectively as

$$H = \mathbf{T}_n \cdot \mathbf{T}_e \tag{2.81}$$

The interaction of the nuclear magnetic dipole moment *operator* $\vec{\mu}_N$, originates from the polarizations of the nuclear proton (spin-1/2) and neutron (spin-1/2) spin moment, with the magnetic field created by the electrons at the nucleus mediate the hyperfine splittings. The nuclear magnetic dipole moment *operator* produces a nuclear vector potential at a distance r from the nucleus:

$$\vec{A}(\vec{r}) = \vec{\mu}_N \times \frac{\vec{r}}{r^3} = \vec{\nabla} \times \left(\frac{\vec{\mu}_N}{r}\right) \tag{2.82}$$

From the non-relativistic Schrödinger theory a hyperfine energy level shift (first-order perturbation) $\Delta E_{\rm hf}$ can be obtained as

$$\Delta E_{\rm hf} = \langle\Psi\Big|\frac{1}{2m}(\vec{P} - \frac{e}{c}\vec{A})^2 - \frac{1}{2m}p^2\Big|\Psi\rangle = -\frac{e}{2mc}\langle\Psi\Big|\vec{P}\vec{A} + \vec{A}\vec{P} - \frac{e}{c}A^2\Big|\Psi\rangle \tag{2.83}$$

where p is the electron's linear momentum, e is the electronic charge, m is the electron mass, c is the speed of light and $|\Psi\rangle$ is the Schrödinger wave function. $\Delta E_{\rm hf}$ can be decomposed into three terms as $\Delta E_{\rm hf}$=$\Delta E^{\rm F}_{\rm hf}$+$\Delta E^{\rm D}_{\rm hf}$+$\Delta E^{\rm O}_{\rm hf}$ known as Fermi contact term, dipolar term, and orbital term, respectively. With

$$\Delta E^{\rm F}_{\rm hf} = -\vec{\mu}_N \frac{8\pi}{3}\mu_B\langle\Psi\Big|\vec{\sigma}\delta(r)\Big|\Psi\rangle \tag{2.84}$$

$$\Delta E^{\rm D}_{\rm hf} = \mu_B \langle\Psi\Big|\frac{1}{r^3}\Big[\vec{\sigma}\vec{\mu}_N - 3(\vec{\sigma}\hat{r})(\vec{\mu}_N\hat{r})\Big]\Big|\Psi\rangle, \hat{r} = \frac{\vec{r}}{r} \tag{2.85}$$

$$\Delta E^{\rm O}_{\rm hf} = -\vec{\mu}_N \frac{e}{mc}\langle\Psi\Big|\frac{1}{r^3}\vec{L}\Big|\Psi\rangle \tag{2.86}$$

where $\mu_{\rm B}(=\frac{e\hbar}{2m})$ is Bohr magneton, $\sigma(=\sigma_1, \sigma_2, \sigma_3)$ are the Pauli spin matrices, and $\vec{L}(=\vec{r}\times\vec{p})$ is orbital angular momentum operator.

In scalar relativistic approximation (SRA), spin-orbit interaction is neglected and taking a crystal with cubic symmetry the last two terms become zero and choosing z-axis

as the magnetic field direction, we are left only the dominating Fermi contact hyperfine field. Choosing $-\vec{\mu}_N = \langle T_n \rangle$ and hyperfine field $H_{\rm hf} = \langle T_e \rangle$ we obtain

$$H_{\rm hf}^{\rm F}; z = \frac{8\pi}{3}\mu_{\rm B}\, m(0) \tag{2.87}$$

$$m(r=0) = \int_{-\infty}^{E_F} \Big[R^2_{s,\uparrow}(r=0,E)n_{s,\uparrow}(E) - R^2_{s,\downarrow}(r=0,E)n_{s,\downarrow}(E)\Big]dE \tag{2.88}$$

where $R_s(0,E)$ is the radial s wave function and $n_s(E)$ is the corresponding s electron DOS. The non-relativistic spin density is

$$m(0) = \langle \Psi | \vec{\sigma}\delta(r) | \Psi \rangle$$

Now the first order perturbation ($H^{'} = e\vec{\alpha}\cdot\vec{A}$) of the Dirac equation leads a hyperfine energy level shift as

$$\Delta E_{\rm hf} = -e\langle\Phi|\vec{\alpha}\cdot\vec{A}(\vec{r})|\Phi\rangle = -e\langle\Phi\left|\vec{\alpha}\,\frac{\vec{\mu}_N\times\vec{r}}{r^3}\right|\Phi\rangle = -e\langle\Phi\left|\vec{\mu}_N\,\frac{\vec{r}\times\vec{\alpha}}{r^3}\right|\Phi\rangle \tag{2.89}$$

where Φ is an eigenspinor (four spinor or bispinor) of the unperturbed Dirac Hamiltonian and $\vec{\alpha}(=\alpha_1,\alpha_2,\alpha_3)$ are the first three Dirac 4×4 matrices. Set z-axis as the magnetic field direction and decompose the Dirac four spinor (wave function) $|\Phi\rangle$ into phi $|\phi\rangle$ and varphi $|\varphi\rangle$ we obtain

$$H_{\rm hf}; z = e\sum_{n\Lambda}\langle\Phi_{n\Lambda}\left|\frac{\vec{r}\times\vec{\alpha}}{r^3}|_z\right|\Phi_{n\Lambda}\rangle = \mu_B\sum_{\Lambda}A_\Lambda\int_{-\infty}^{E_F}F_\Lambda(E)n_\Lambda(E)dE \tag{2.90}$$

which is an energy integration with $\Lambda=(\kappa,\mu)$ is the relativistic equivalent of $L=(\ell,m)$ and

$$A_\Lambda = 4\pi i\langle\chi_\Lambda|(\vec{\sigma}\times\hat{r})_z|\sigma_r\chi_\Lambda\rangle = \frac{16\pi\kappa\mu}{4\kappa^2-1} \tag{2.91}$$

where χ_Λ is spin-angular spinor, σ_r operates as $\sigma_r\chi_\Lambda = -\chi_{\bar{\Lambda}}$ with $\bar{\Lambda}=(-\kappa,\mu)$ and a radial integration as

$$F_\Lambda(E) = -\frac{mc}{\pi\hbar}\int_0^\infty g_\Lambda(r,E)f_\Lambda(r,E)dr \tag{2.92}$$

where $g_\Lambda(r,E)$ and $f_\Lambda(r,E)$ are radial wave functions. The equation (2.90) with (2.91) and (2.92) is the relativistic formulation of hyperfine field (HF), first derived by G. Berit in New York University [8,9]. In (2.90) the component varphi $|\varphi\rangle$ is replaced by

$$|\varphi\rangle = \Big(\frac{1}{2M(r)c}\Big)\vec{\sigma}\vec{P}\,|\phi\rangle = \Big(\frac{1}{2mc}\Big)S(r)\vec{\sigma}\vec{P}\,|\phi\rangle \tag{2.93}$$

obtained from the Dirac equation, where the relativity factor

$$S(r) = \frac{m}{M(r)} = \left[1 + \frac{E - V^0(r)}{2mc^2}\right]^{-1} \tag{2.94}$$

is defined as the inverse of the relativistic mass enhancement and at $\lim_{c\to\infty} S(r) = 1$, using this relativity limit we can deduce the relativistic form of the hyperfine terms as

$$\Delta E_{\rm hf}^{\rm D} = \mu_B \langle\phi\Big|\frac{S(r)}{r^3}\Big[\vec{\sigma}\vec{\mu}_N - 3(\vec{\sigma}\hat{r})(\vec{\mu}_N\hat{r})\Big]\Big|\phi\rangle, \hat{r} = \frac{\vec{r}}{r} \tag{2.95}$$

$$\Delta E_{\rm hf}^{\rm O} = -\vec{\mu}_N \frac{e}{mc}\langle\phi\Big|\frac{S(r)}{r^3}\vec{L}\Big|\phi\rangle \tag{2.96}$$

The left generalized contact interaction is

$$\Delta E_{\rm hf}^{\rm F} = -\vec{\mu}_N \frac{8\pi}{3}\mu_B\langle\phi\Big|S(r)\vec{\sigma}\delta(r)\Big|\phi\rangle - \mu_B\langle\phi\Big|\frac{1}{r^2}\frac{\partial S}{\partial r}\Big[\vec{\sigma}\vec{\mu}_N - (\vec{\sigma}\hat{r})(\vec{\mu}_N\hat{r})\Big]\Big|\phi\rangle \tag{2.97}$$

In the non-relativistic limit S=1 and $\frac{\partial S}{\partial r}$=0 and thus 2$^{\rm nd}$ term of (2.97) vanishes and the 1$^{\rm st}$ term reduces to the previous Fermi contact term.

In SRA spin-orbit interaction is omitted and thus we can treat the semi-relativistic magnetic problems with the same ease as in the non-relativistic theory. Hence only the states $\kappa = -1(s_{1/2})$ contribute to the contact interaction. From (2.90) with $A_{-1,\pm 1/2} = \mp(8\pi)/3$ we can express the relativistic formulation of HF in integral form as

$$H_{\rm hf}; z = \frac{8\pi}{3}\mu_B \int_{-\infty}^{E_F}\Big[F_{s,\uparrow}(E)n_{s,\uparrow}(E) - F_{s,\downarrow}(E)n_{s,\downarrow}(E)\Big]dE \tag{2.98}$$

This is basically the reformulation of the original contact term. In the non-relativistic limit, the matrix elements in relativistic form of the s wave function $F_s(E)$ related to $R_s(0,E)$ as $F_s(E) \cong \frac{1}{4\pi}\Big|R_s(0,E)\Big|^2$ [10]. The integral equation (2.98) accounts for both up- and down spin electrons by including the contributions of all core, occupied and valence states.

2.8 Exchange Couplings and Stability Mechanism in Dilute Magnetic States

Hybridization introduced by doped TM impurities plays crucial role in realizing magnetic couplings that stabilize the dilute magnetic states. Among them double-exchange (DX), super-exchange (SX), and *p*-*d* exchange (*pd*X) couplings are prominent in the present system[11], shown schematically in **Fig.** 2.6 (a-d).

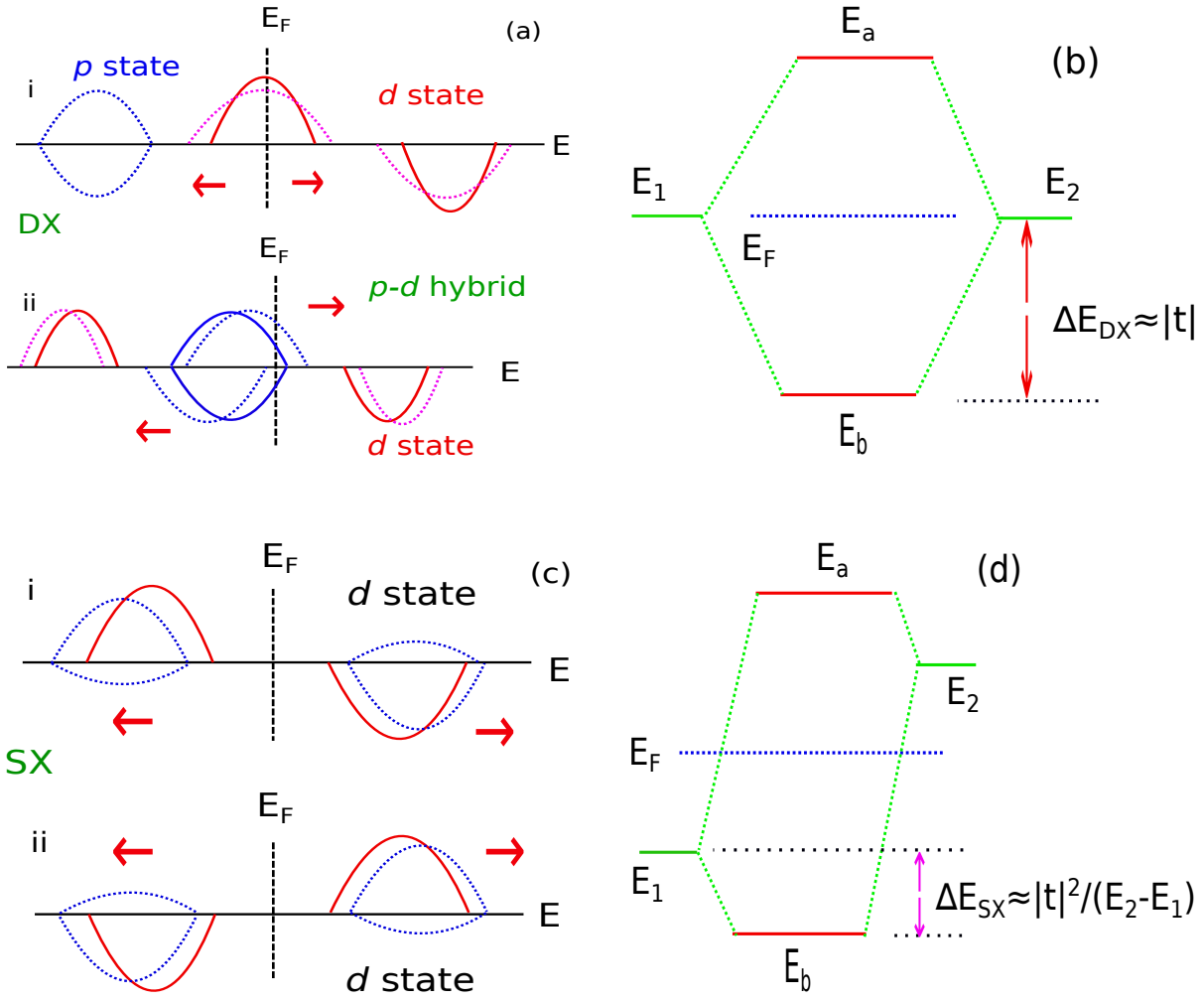

Fig. 2.6 (a) Schematic drawing of impurity partial density of states to explain (i) double-exchange, and (ii) *p*-*d* exchange, and (b) energy splittings due to double-exchange. (c) Super-exchange coupling between occupied up (down) spin and empty up (down) spin states, and (d) energy diagram in super-exchange splitting.

Figure 2.6 (a(i)) shows schematic spin-polarized partial d DOS associated doped TM impurity around the gap region in a chalcopyrite semiconductor. The drawn state is symmetric at the Fermi level and inverse parabolic shape. The Fermi level is located in the majority t_{2g} state in the Cr^{3+} and Mn^{3+} doped cases. The states lying below the Fermi level are mostly occupied bonding states. When a transfer integral t is introduced between two degenerate atomic states with energies E_1=E_2, as shown in **Fig.** 2.6(b), they form lower lying bonding and higher lying antibonding level. The energy gain in bonding states by mixing and broadening is of the order of $|t|$, which stabilizes the FM state. This effect is known as the double-exchange mechanism, which can be expressed as $\Delta E_{\mathrm{DX}}(x) \approx \sqrt{x}|t|$, where x is the doping composition. Thus DX originates from the impurity *d*-*d* hybridization, and energy is gained by broadening of the hybridized band, where the band center of gravity is fixed. The energy gain is maximum if the Fermi level appears just at the middle of the band and vanishes at the band edge.

*pd*X comes from the mixing between impurity d and host p states. Mixed band shifted down (up) to lower (higher) energy results in gain energy. Therefore, in *pd*X the hybridized band center of gravity is shifted in lower energy range to stabilize the FM state, as shown in **Fig.** 2.6 (a(ii)). The energy gain is proportional to the impurity concentration x and the transfer integral t.

The expression for energy gain can be derived from a tight-binding model of the impurity band. The impurity bandwidth W is defined as the variance of the energy eigenvalues E to the mean value $\bar{E}$ as [12]

$$W^2 = \langle (E - \bar{E})^2 \rangle = \sum_{j \neq 0} |H_{0j}|^2 \tag{2.99}$$

where H_{0j} denotes the hopping matrix element between the sites 0 and j. Suppose that in a certain configuration of Mn atoms in $CuAlSe_2$ one of the Mn atoms is at site 0. In this configuration, H_{0j} has a finite value, say, t_{0j}, if another Mn atom is at site j, otherwise, $H_{0j} = 0$. In CPA, a configurational average is taken over all sites $j \neq 0$. The probability of finding a Mn atom at site j is given by concentration x of Mn. Thus the configuration

average gives

$$\langle W^2 \rangle_{\text{conf}} = x \sum_{j \neq 0} |t_{0j}|^2 \tag{2.100}$$

Therefore, effective bandwidth W is proportional to $\sqrt{x}$ and the energy gain in double exchange relates as $\Delta E_{\text{DX}}(x) \approx \sqrt{x}|t|$, whereas in *p*-*d* exchange W relates linearly with concentration x and thus energy gain can be mapped as $\Delta E_{pd\text{X}}(x) \approx x|t|$, shown in **Fig.** 2.6 (a(ii)).

In V^{3+} doped case majority $e_{\text{g}}^{\uparrow}$ state is fully occupied and majority $t_{2\text{g}}^{\uparrow}$ state is fully empty. Due to band broadening mechanism, the energy is gained by shifting the majority $e_{\text{g}}^{\uparrow}$ state to lower energy region and gives a stability of FM state by ferromagnetic super-exchange (FSX) coupling. FSX coupling can be expressed as

$$\Delta E_{\text{FSX}}(x) \approx \frac{2x|t|^2}{\epsilon_{t_{2\text{g}}}^{\uparrow} - \epsilon_{e_{\text{g}}}^{\uparrow}} \tag{2.101}$$

where the hopping integral t acts between the $e_{\text{g}}^{\uparrow}$ and the $t_{2\text{g}}^{\uparrow}$ states of the impurity.

SX is a *d*-*d* coupling (via valence *p* state) between two antiferromagnetic spin states of impurity i and impurity ii, as shown pictorially in **Fig.** 2.6 (c-i, ii). Up spin electron of impurity i can hop at the same up spin state of impurity ii, and *vice versa*. Coupled bands gain energy by sliding back and forth. Therefore, antiferromagnetic super-exchange (ASX) may dominate where the Fermi level lies in between the occupied and unoccupied states. Some minor bands can be explained as the tails of *d* bands. If two separate atomic levels brought closer enough as like the diagram in **Fig.** 2.6 (d), the atomic wave functions overlap each other and form a bonding-antibonding level. The energy levels of bonding and antibonding states are lower and higher than the respective energy level $E_1 < E_2$, as shown in **Fig.** 2.6(d). The degenerate energy picture can be deduced from this diagram when $E_1 = E_2$. The energy gain in ASX (DSM state in the present case) can be expressed as

$$\Delta E_{\text{ASX}}(x) \approx \frac{x|t|^2}{\epsilon_{t_{2\text{g}}}^{\uparrow} - \epsilon_{t_{2\text{g}}}^{\downarrow}} \tag{2.102}$$

where the hopping integral t acts between majority and minority $t_{2\text{g}}$ states, as shown in the denominator.

2.9 Computational Strategy in KKR-CPA

We used Korringa-Kohn-Rostoker (KKR) Green's function method in combination with generalized gradient approximation (GGA) (a semilocal density approximation) with the parametrization given by Perdew and Wang [13] for electronic structures and magnetic properties calculations. Random mixing of impurity ions are treated by coherent potential approximation (CPA) within the single-site approximation [7]. CPA is not employed in host compounds electronic structure calculation. In DSM state (a disordered paramagnetic state) the local magnetic moments of TM or TM pair are aligned randomly. Such spin disordered state is also treated by the CPA. Muffin-tin (MT) potential is assumed for electron density at each atomic site and interstitial site, where the system is considered to be filled with an array of inscribed, non-overlapping spheres of spherical potentials, and constant in the region between the spheres. Any core charge outside the MT (tails of orbitals) are treated as part of the interstitial charge. Multiple scattering from the potentials are assumed and the expansion of the valence wave functions in spherical harmonics was truncated at maximum angular momentum of scattering $L_{\max}$=2, whereas the interstitial sites are treated as s wave scattering centers. Relativistic effects are considered within the scalar relativistic approximation (SRA). Eight extra empty MT potentials with zero charge, not centered on atoms, are taken in the interstitial sites in addition to those for the normal eight atomic sites. Self-consistency is obtained with an eigenvalue tolerance level of convergence $\sim 1\mu$Ry in total energy. An imaginary part of 1 mRy is used in complex contour integration. Finally, the iteration to self-consistency was continued until the total energy was stable to 0.0001mRy. Magnetic structures and related properties are computed using the KKR-CPA program package "Machikaniyama 2002" produced by Akai [14].

2.9.1 *Computational Steps*

The Kohn-Sham (KS) equations are solved by the following self-consistent procedures:

1) Presume a trial effective potential $V_{\mathrm{KS}}(\mathrm{r})$.

2) Solve one-electron KS equations and calculate the eigenfunctions $\psi_i(\mathrm{r})$.

3) Integrate $\sum_i |\psi_i(r,E)|^2$ up to Fermi energy to obtain electron density n(r).

4) Solve the Poisson's equation for n(r) and construct the Hartree potential $V_{\mathrm{H}}(\mathrm{r})$.

5) Calculate the new effective potential by adding the exchange-correlation potential with Hartree potential : $V_{\mathrm{KS}}(r) = V_{\mathrm{H}}(r) + V_{\mathrm{XC}}(r)$

6) Compare the new $V_{\mathrm{KS}}(\mathrm{r})$ and old $V_{\mathrm{KS}}(\mathrm{r})$ and generate a next trial effective potential $V_{\mathrm{KS}}(\mathrm{r})$ (by proper adjusting the mixing parameter, if needed).

7) Iterate the above steps until KS effective potential $V_{\mathrm{KS}}(\mathrm{r})$ converges.

2.10 Full-Potential Linear Augmented Plane Wave

In full-potential linear augmented plane wave (FLAPW) scheme, the plane waves are treated as the basis functions in the interstitial region:

$$\phi(k_n') = \frac{1}{\sqrt{\Omega}} e^{\mathrm{i}\mathbf{k}_{\mathrm{n}}'\cdot\mathbf{r})} \tag{2.103}$$

where $\mathbf{k}_n' \equiv \mathbf{k} + \mathbf{G}_n$ with the reduced wave vector $\mathbf{k}$ $(= 2\pi/\lambda)$ or $\mathbf{k}$ point and reciprocal lattice vector $\mathbf{G}_n$ in the first Brillouin zone (BZ). $\mathbf{k}_n'$ is any wave vector lies outside the first BZ. Ω is the unit cell volume. Inside the muffin-tin (MT) spheres the basis function can be written as a linear combination of all radial functions with spherical harmonics:

$$\phi(k_n) = \sum_{lm} \Big[A_{lm}^n R_l(E_l) + B_{lm}^n \dot{R}_l(E_l) \Big] Y_l^m(\hat{r}) \tag{2.104}$$

where R_l, $\dot{R}_l$ are the radial wave function and its energy derivative at an appropriate energy E_l for angular quantum number l. The coefficients A_{lm}^n and B_{lm}^n are determined from boundary condition. Using the Rayleigh expansion procedure, the plane waves are

expanded to apply the boundary condition at the MT sphere.

$$\phi(k_n, R_{\rm mt}) = \frac{4\pi}{\sqrt{\Omega}} \sum_{lm} i^l j_l(k_n R_{\rm mt}) Y_l^{m*}(\hat{k}_n) Y_l^m(\hat{R_{\rm mt}}) \tag{2.105}$$

We get a trial wave function using the above basis sets as

$$\psi(k) = \sum_n a_n \phi(k_n) \tag{2.106}$$

Applying the variational method yields the secular or eigen-energy equation [15-18] as

$$H\, a = E\, O\, a \tag{2.107}$$

$$H_{nm} = \langle \phi(k_n) | H | \phi(k_m) \rangle \tag{2.108}$$

$$O_{nm} = \langle \phi(k_n) | \phi(k_m) \rangle \tag{2.109}$$

where H_{nm} is the Hamiltonian matrix and O_{nm} is the overlap matrix with respect to the basis set and a is the expansion coefficients of a trial wave function. In practice, above secular equations are solved to obtain the eigenstates and eigenvalues.

In full-potential case, we consider plane waves in the interstitial region and spherical harmonics inside the MT sphere given by

$$V_{\rm full}(\mathbf{r}) = \left\{ \begin{array}{ll} \sum_{ilm} V_{ilm}\Big(|\mathbf{r} - \mathbf{R}_i|\Big) Y_{lm}\Big(\mathbf{r} - \mathbf{R}_i\Big), & for \quad |\mathbf{r} - \mathbf{R}_i| \le R_{\rm mt} \\ \sum_{\mathbf{G}} e^{i\mathbf{G}\cdot\mathbf{r}}\, V_{\mathbf{G}}\,, & for \quad |\mathbf{r} - \mathbf{R}_i| > R_{\rm mt} \end{array} \right\} \tag{2.110}$$

where i is the atomic site index and $\mathbf{G}$ is the reciprocal lattice vector. $\mathbf{G}$=0 gives a constant potential at the interstitial region and l=0, m=0 yield the MT potential (**cf. Eq. 2.76**). Therefore, KKR-MT potential is a limiting form of the full-potential LAPW. Interested readers can see more details on full-potential method in FLAPW in the Ref. [18].

2.11 Computational Framework in FLAPW

Electronic band structures and 3*d* TM doped supercells are calculated with GGA exchange-correlation potential by Perdew, Burke, and Ernzerhof (PBE) [19]. One-electron Kohn-Sham equations are solved iteratively by the FLAPW method [15-18]. The spin-orbit interaction is treated as the second-variation step in the self-consistent

field (SCF) iteration with a spin quantization axis along the [001] direction. In GGA+U calculation, Hubbard U and Stoner terms are included as parameters with U=5 eV and J=0.99 eV for the Cu d states in $CuInS_2$ to realize the effect of Hubbard U term in opening the energy gap. Brillouin-zone (BZ) integrations are performed with a 8×8×8 mesh for the host system and 4×4×4 mesh for the doped supercells, where a uniform grid including BZ center is considered and set the cutoff energy of plane wave basis is 20Ry for wave functions and 160Ry for charge density and potential functions. Improved tetrahedron method is used for k point integration inside BZ. Appropriate number of valence states is used in self-consistent field (SCF) mode. Cubic harmonics is used for projection of PDOS and Euler angles are taken as (0, 0, 0). Magnetic calculations, especially the 3d TM doped supercells are calculated carefully for simple and then second-order Anderson mixing of charge and spins to achieve the SCF convergence. Experimental lattice and internal parameters are used for numerical computations. Electronic band structures, magnetic states of 3d TM doped systems, and enthalpy of formation for a substitutionally doped supercells (4 times bigger than primitive cell) are calculated by the full-potential linearized augmented plane wave (FLAPW) package "HiLAPW2002" produced by T. Oguchi [20].

2.12 References

[1] P. Hohenberg and W. Kohn Phys. Rev. **136**, B864 (1964).

[2] W. Kohn and L.J. Sham Phys. Rev. **140**, A1133 (1965).

[3] M. Born and J.R. Oppenheimer, Ann. Phys. (Leipzig) **84**, 457 (1927).

[4] V.L. Moruzzi, J.F. Janak and A.R. Williams, Calculated Electronic Properties of Metals (Pergamon, New York, 1978).

[5] P. Mavropoulos and N. Papanikolaou, NIC Series, Jülich, Vol. 31, ISBN 3-00-017350-1, pp. 131-158 (2006).

[6] A. Lodder and P.J. Braspenning, Phys. Rev. B **49**, 10215 (1994).

[7] H. Shiba, Prog. Theor. Phys. **46**, 77 (1971).

[8] G. Breit, Phys. Rev. **35**, 1447 (1930).

[9] H. Akai, M. Akai, S. Blügel, B. Drittler, H. Ebert, K. Terakura, R. Zeller and P.H. Dederichs, Prog. Theor. Phys. Suppl. **101**, 11 (1990).

[10] S. Blügel, H. Akai, R. Zeller and P.H. Dederichs, Phys. Rev. B **35**, 3271 (1987).

[11] B. Belhadji, L. Bergqvist, R. Zeller, P.H. Dederichs, K. Sato and H. Katayama-Yoshida, J. Phys.: Condens. Matter **19**, 436227 (2007).

[12] K. Sato, L. Bergqvist *et al.*, Rev. Mod. Phys. **82**, 1633 (2010).

[13] J.P. Perdew and Y. Wang, Phys. Rev. B **45**, 13244 (1992).

[14] H. Akai, 2002, http://sham.phys.sci.osaka-u.ac.jp/∼kkr/

[15] J.C. Slater, Phys. Rev. **51**, 846 (1937).

[16] O.K. Andersen, Phys. Rev. B **12**, 3060 (1975).

[17] D.D. Koelling and G.O. Arbman, J. Phys. F: Metal Phys. **5**, 2041 (1975).

[18] M. Weinert, J. Math. Phys. **22**, 2433 (1981).

[19] J.P. Perdew, K. Burke and M. Ernzerhof, Phys. Rev. Lett. **77**, 3865 (1996); **78**, 1396 (1997).

[20] T. Oguchi, http://www.cmp.sanken.osaka-u.ac.jp/ oguchi/index-e.html

Chapter 3

Chalcopyrite Semiconductors

Chalcopyrite (CP)[1] semiconductors are basically ternary compounds consist of either group I-III-VI_2 or group II-IV-V_2 elements with chemical formula ABX_2, where A= Cu, Ag, Zn, Cd, B=Al, Ga, In, Tl, Si, Ge, Sn and X=S, Se, Te, P, As, Sb. CP structure is a superlattice of zinc-blende (ZnS) structure. The conventional unit cell is twice of the zinc-blende structure. The former (latter) consists of eight (two) atoms per primitive unit cell. The Bravais lattice of CP structure is body-centered tetragonal (BCT).

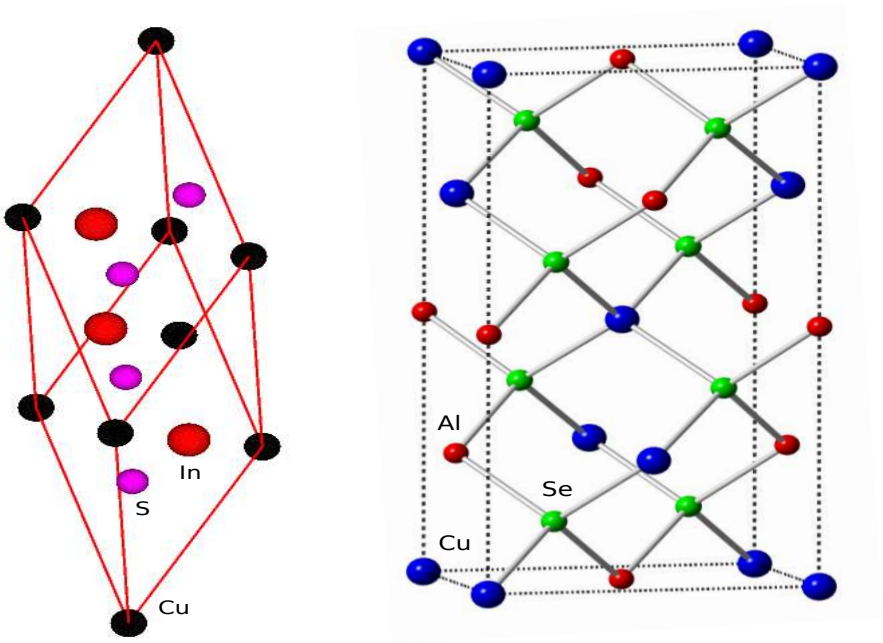

Fig. 3.1 Primitive (left) and conventional (right) unit cell of chalcopyrite structure.

[1]Greek meaning of chalco is cuprum and pyrite is puritēs (in fire), e.g., sulfide mineral $CuFeS_2$.

A lattice is a periodic array of abstract points in space. The atoms are the basis and attached to the lattice points. Therefore, the logical construction is

$$crystal\ structure = lattice + basis \tag{3.1}$$

The unit cell contains three different types of basis atoms. The primitive cell contains two formula units of atoms and the conventional cell comprises a four formula units of atoms, whereas a single formula unit, say $CuAlSe_2$ has only four atoms. In terms of the containing lattice points, the conventional cell is twice than the primitive cell.

The prototypical mineral of the CP structure is $CuFeS_2$, whereas FeS_2 type compound has a pyrite (cubic) structure. $CuInS_2$, $CuAlSe_2$, $AgAlSe_2$ and $AgAlS_2$ are the CP semiconductors having relatively wider energy band gap, that we consider as host systems in this study.

3.1 Crystal Structure

The unit cell of CP structure is shown in **Fig.** 3.1 which consist of 16 atoms in the conventional cell and eight atoms in the primitive unit cell and other equivalent atoms are simply connected by the Bravais vectors. Three distinct types of atoms exist in the cell: two cations and one anion. Two cations form two near-neighbor cation-anion bonds A-X and B-X with unequal bond lengths when the cell is tetragonally distorted from its undistorted structure. The BCT structure has space group symmetry $I\bar{4}2d$ and number 122 [1]. BCT in real space becomes a face-centered tetragonal in inverse space, which is equivalent to the original BCT rotated 45° about the z (principal) axis.

Constraints on conventional cell axes and angles in tetragonal system are: a_1=$a_2 \neq a_3$ and α=β=γ=90°. The general crystal structure is triclinic system, one of the 14 Bravais lattices constrained as $a_1 \neq a_2 \neq a_3$ and $\alpha \neq \beta \neq \gamma \neq 90°$ and the tetragonal structure is a special case of triclinic structure.

A symmetric set of primitive translation vectors to connect the equivalent lattice points in the BCT structure is

$\vec{a}_1 = a\hat{x} \qquad (\because \quad |\vec{a}_1| = \text{a}, \ \text{etc.})$

$\vec{a}_2 = a\hat{y} \ (a = b)$

$\vec{a}_3 = \frac{1}{2}(a\hat{x} + a\hat{y} + c\hat{z}) \ (a = b \neq c),$

where the numbers a, b, and c specifying the size of a unit cell are called lattice parameters (lattice constants) or edges of a tetragonal cell, and $\hat{x}$, $\hat{y}$, and $\hat{z}$ are three orthogonal unit vectors.

Another symmetric set of basic (fundamental or primitive) vectors to connect the equivalent sites is

$\vec{a}_1 = \frac{1}{2}(-a\hat{x} + a\hat{y} + c\hat{z})$

$\vec{a}_2 = \frac{1}{2}(a\hat{x} - a\hat{y} + c\hat{z})$

$\vec{a}_3 = \frac{1}{2}(a\hat{x} + a\hat{y} - c\hat{z})$

The crystal displacement or translation vector (period between crystal atoms) connecting equivalent sites is given by

$$\vec{R} = n_1\vec{a}_1 + n_2\vec{a}_2 + n_3\vec{a}_3 \tag{3.2}$$

$$\therefore \quad \vec{R} = \sum_{i=1}^{3} n_i\vec{a}_i \quad \left(\vec{G} = \sum_{i=1}^{3} n_i\vec{a}_i^*\right) \tag{3.3}$$

where $\vec{a}_1$, $\vec{a}_2$, and $\vec{a}_3$ are three fundamental or primitive translation vectors of direct lattice ($\vec{G}$ is a reciprocal lattice vector formed by linear sum of reciprocal lattice primitive vectors $\vec{a}_i^*$, and defined as $\vec{a}_1^* = 2\pi(\vec{a}_2 \times \vec{a}_3)/(\vec{a}_1 \cdot \vec{a}_2 \times \vec{a}_3)$, etc.) not all in the same plane, and n_1, n_2, and n_3 are arbitrary integers, i.e., n_i=0, $\pm$1, $\pm$2, $\pm$3, ... [2]. The lengths of any two sides are equal and the third axis can be longer or shorter than the two equal sides. Since any primitive unit cells of a given structure are of equal volume, thus irrespective of the arbitrariness in basic vectors, the volume of the primitive cell is:

$$V = \vec{a}_1 \cdot (\vec{a}_2 \times \vec{a}_3) = \frac{1}{2}a^2c \tag{3.4}$$

The general form of the atomic coordinates [3, 4] of CP crystals in BCT structures are shown in **Table** 3.1, where u is the local distortion parameter of cation-anion.

Table 3.1 Cartesian coordinates (x, y, z) of atomic sites of chalcopyrite-type ABX_2 BCT structure. The Wyckoff letters (WL) denote the symmetry level in accordance to the space group $I\bar{4}2d$.

Atoms	Coordinates (x, y, z)	WL
A_1	$0, \quad 0, \quad 0$	a
A_2	$0, \quad \frac{1}{2}, \quad \frac{1}{4}$	a
B_1	$0, \quad 0, \quad \frac{1}{2}$	b
B_2	$0, \quad \frac{1}{2}, \quad \frac{3}{4}$	b
X_1	$u, \quad \frac{1}{4}, \quad \frac{1}{8}$	d
X_2	$-u, \quad \frac{3}{4}, \quad \frac{1}{8}$	d
X_3	$\frac{3}{4}, \quad u, \quad \frac{7}{8}$	d
X_4	$\frac{1}{4}, \quad -u, \quad \frac{7}{8}$	d

3.2 Lattice Parameters and Bond Lengths

We can estimate cell parameters either by i) first-principles method (energy minimization technique), or ii) empirical method (Vegard's rule). As muffin-tin potential limits us to obtain a true minimum energy point with arbitrary variation of lattice parameters, hence we used Vegard's rule to estimate cell parameter for a typical case.

Vegard's Rule

We can estimate cell parameters by Vegard's rule for equistructural crystals. Assume that cell volume is constant for iso-structure at a fixed temperature. Suppose we dope x=5% of Fe at host In site of CP $CuInS_2$ and obtain the disordered alloy $Cu(In_{1-x}Fe_x)S_2$. To employ the Vegard's rule, we decompose the alloy into its basic compounds in terms of the percentage of concentration. First, using a linear relation we obtain an estimation of

the alloy (target material) lattice parameter with respect to the measured cell parameters of the host compounds [5,6].

Parameter a : $a[\mathrm{Cu(In_{1-x}Fe_x)S_2}] = (1\text{-x})a_0[\mathrm{CuInS_2}] + \mathrm{x}\ a_1[\mathrm{CuFeS_2}]$

$\Rightarrow a[\mathrm{Cu(In_{0.95}Fe_{0.05})S_2}] = 0.95(5.52) + 0.05(5.289) = 5.50845$ Å

Parameter c : $c[\mathrm{Cu(In_{1-x}Fe_x)S_2}] = (1\text{-x})c_0[\mathrm{CuInS_2}] + \mathrm{x}\ c_1[\mathrm{CuFeS_2}]$

$\Rightarrow c = 0.95(11.13) + 0.05(10.423) = 11.09465$ Å

Parameter u: $u[\mathrm{Cu(In_{1-x}Fe_x)S_2}] = (1\text{-x})u_0[\mathrm{CuInS_2}] + \mathrm{x}\ u_1[\mathrm{CuFeS_2}]$

$\Rightarrow u = 0.95(0.214) + 0.05(0.2574) = 0.21617 \Rightarrow u = 0.216$

Bond Lengths

Chemical bonds are formed at minimum-energy state, where the distance between the atomic nuclei is the **bond length**. Chemical formula of CP structure has two distinct cations ($A \neq B$), their electronic affinity with anion would be different. Bond length [7] elucidates the effect of crystal field splitting and charge polarization.

Exemplary Bond Length Calculation of $\mathrm{CuAlSe_2}$

In chalcopyrite $\mathrm{CuAlSe_2}$ anion sublattice parameter u=0.26 and tetragonal distortion $\eta = c/2a$=10.90/2(5.606)=0.972 < 1. The calculated cation-anion bond-lengths in terms of the measured lattice parameters are as follows

$R_{\mathrm{Cu-Se}}$=$a[1/16 + u^2 + \eta^2/16]^{1/2}$=0.4349 a=2.44 Å

$R_{\mathrm{Al-Se}}$=$a[1/16 + (1/2 - u)^2 + \eta^2/16]^{1/2}$=0.4233 a=2.37 Å

Al-Al (doped site) bond length can be estimated as $R_{\mathrm{Al-Al}}$=$[(a/2)^2 + (c/4)^2]^{1/2}$=3.91 Å. For undistorted lattice u=1/4, tetragonal ratio η=$c/2a$=1 and $R_{\mathrm{Cu-Se}}$=$R_{\mathrm{Al-Se}}$=$a\sqrt{3/16} = 0.4330\,a$ =2.43 Å

Bond length mismatch: α=$R^2_{\mathrm{Cu-Se}} - R^2_{\mathrm{Al-Se}} = (u - 1/4)a^2 = 0.01\,a^2$=0.31 Å^2.

Similarly, the bond lengths in $\mathrm{CuInS_2}$, $\mathrm{AgAlSe_2}$ and $\mathrm{AgAlS_2}$ are calculated and summarized them in **Table** 3.2.

Table 3.2 Chalcopyrite-type ABX_2 BCT structure form two types of tetrahedral bond between cation and anion as $A-X$ and $B-X$. Tetragonal distortion (ratio) $\eta = c/2a = 1$ for undistorted lattice with inner parameter u=1/4 and undistorted bond length (UBL) is $R_{\rm UBL}$=($R_{\rm A-X}$=$R_{\rm B-X}$). The bond length mismatch is defined as the modulus of α=$R^2_{\rm B-X}$ − $R^2_{\rm A-X}$.

ABX_2	η	$A-X$	R_{A-X} (Å)	$B-X$	R_{B-X} (Å)	$R_{\rm UBL}$ (Å)	α (Å^2)
$CuInS_2$	1.008>1	Cu−S	2.29	In−S	2.52	2.39	1.1
$CuAlSe_2$	0.972<1	Cu−Se	2.44	Al−Se	2.37	2.43	0.31
$AgAlSe_2$	0.903<1	Ag−Se	2.57	Al−Se	2.429	2.579	0.71
$AgAlS_2$	0.901<1	Ag−S	2.567	Al−S	2.229	2.466	1.62

3.3 Electronic States and Properties

Electronic structures of the ordered compounds $CuInS_2$ (CIS), $CuAlSe_2$ (CAS), $AgAlSe_2$ (AASe) and $AgAlS_2$ (AAS) calculated by KKR-Green's function method are shown in **Fig.** 3.2 (a-d). Total and partial (Cu d, Ag d, In p, Al p, S p and Se p state) density of states are plotted as a function of energy in Rydberg unit. The valence states below the intrinsic energy gap are occupied and the conduction states beyond the principal gap are empty. Cu d states dominate over In (Al) p states and S (Se) p states. Cu d and anion p states compete and eventually anion p state dominate near the lower bound of the energy, whereas In (Al) p states are much smaller. CIS exhibit relatively lower energy gap than CAS, AASe and AAS. The measured energy gaps are CIS: $E_{\rm g}^{\rm expt}$ =1.53 eV, CAS: $E_{\rm g}^{\rm expt}$ =2.67 eV, AASe: $E_{\rm g}^{\rm expt}$ =2.55 eV, and AAS: $E_{\rm g}^{\rm expt}$ =3.13 - 3.60 eV [7,8]. The measured cell parameters are CIS: a=5.52Å, c=11.13Å, and u=0.214 [5], CAS: a=5.606Å, c=10.90Å, and u=0.26, AASe: a=5.956Å, c=10.75Å, and u=0.27 and AAS: a=5.695Å, c=10.26Å, and u=0.30 [4]. Tetragonal ratios of CIS, CAS, AASe, and AAS are η=c/a=2.016, 1.944, 1.805, and 1.802, respectively.

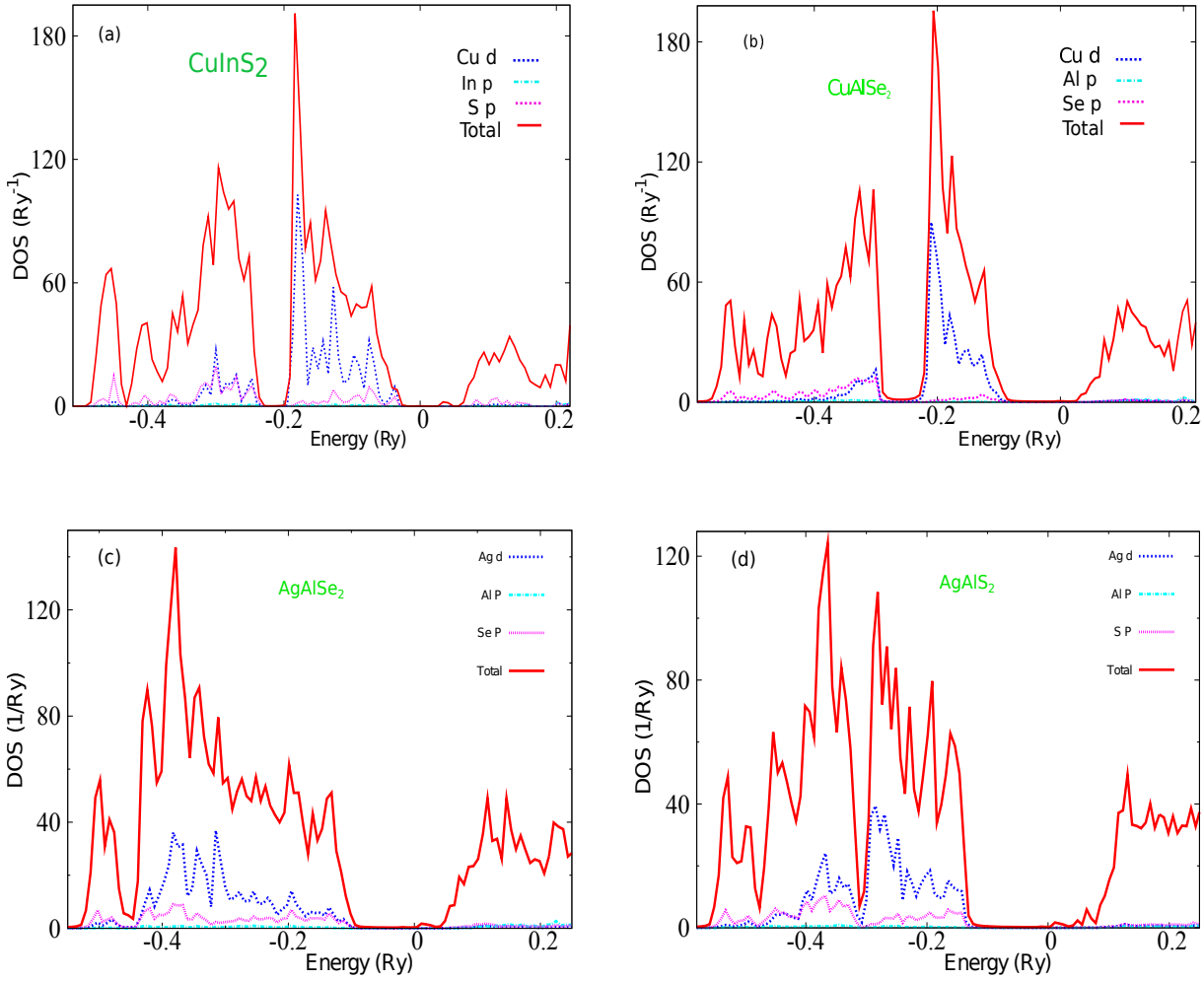

Fig. 3.2 Total density of states (DOS) and local p and d DOS of chalcopyrite semiconductors (a) $CuInS_2$, (b) $CuAlSe_2$, (c) $AgAlSe_2$, and (d) $AgAlS_2$.

Density of states (DOS) of occupied valence and empty conduction states are separated by an energy gap. The valence Cu d and Ag d states mostly control the peak total DOS in Cu and Ag based compounds, respectively. Chalcopyrite semiconductors are non-spin polarized materials with zero total and local magnetic properties (e.g., moments, hyperfine fields etc.). They can be used as a host (starting) material to realize dilute magnetic states by doping and codoping. For optimum or wider and direct energy gaps, they can be used to design novel class magnetic half metals.

3.4 Electronic Band Structures

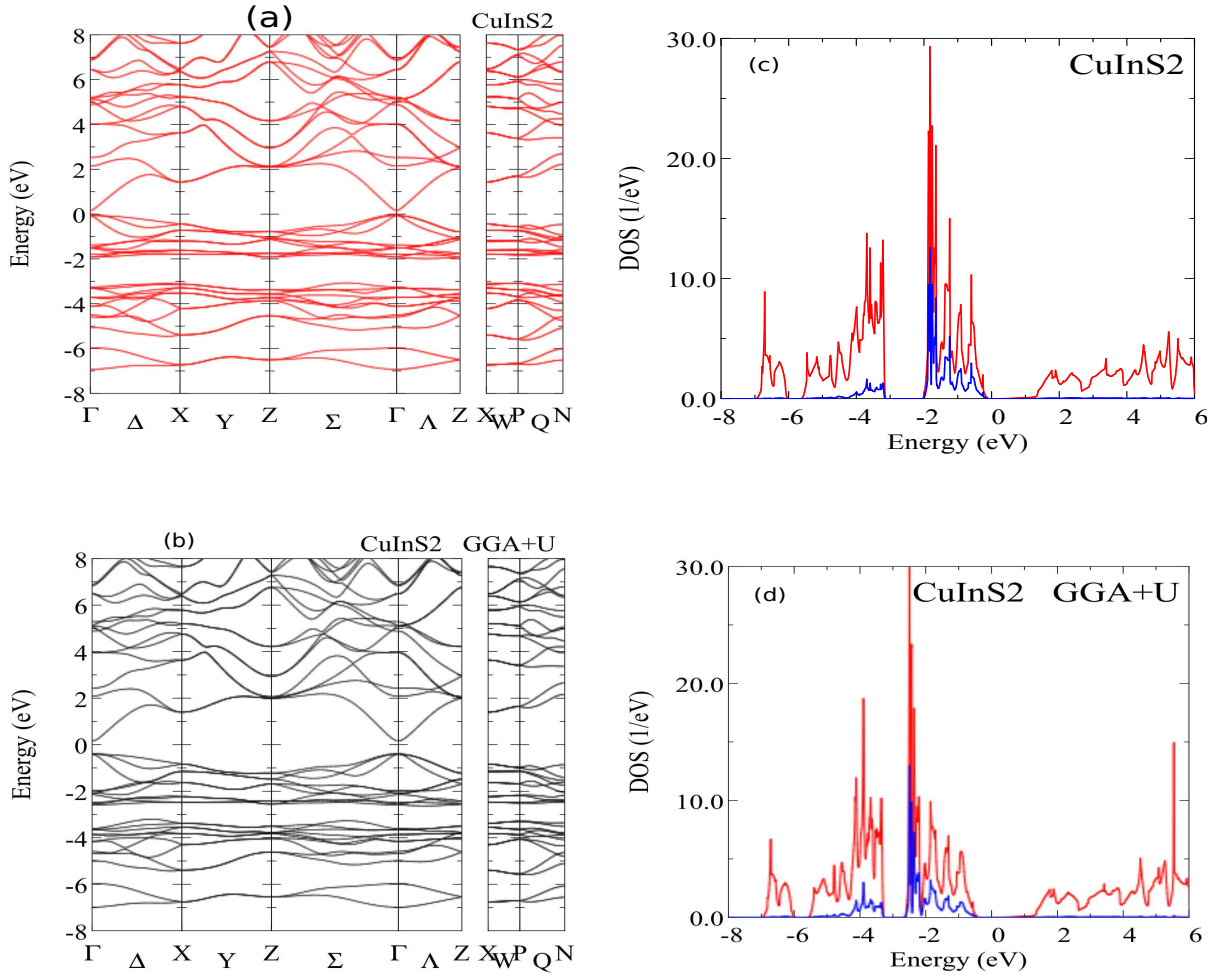

Fig. 3.3 Band structures along the symmetric k points in Brillouin zone of chalcopyrite semiconductor $CuInS_2$ (a) GGA, and (b) GGA+U. In the case of density of states (DOS), (c) GGA, and (d) GGA+U, where red curves are total DOS and blue curves are Cu d DOS.

Chalcopyrite semiconductor $CuInS_2$ has the measured energy gap of 1.53 eV, higher than the familiar zinc-blende GaAs (reported by K. Sato *et al.* [9] as DMS by KKR-CPA-LDA) with the measured energy gap of 1.43 eV. On the contrary, FLAPW calculated energy gap of $CuInS_2$ is 0.18 eV as shown in **Fig.** 3.3 (a,c), a half of the zinc-blende InAs (reported by H. Akai [10] as DMS by KKR-CPA-LDA) measured energy gap. An improved gap of 0.54 eV (three times larger than before) is obtained by GGA + U calculations as shown in **Fig.** 3.3 (b,d), where the Hubbard U parameter was fixed to U=5 eV and the exchange (Stoner parameter) to J=0.99 eV and was included in the d states of Cu atom.

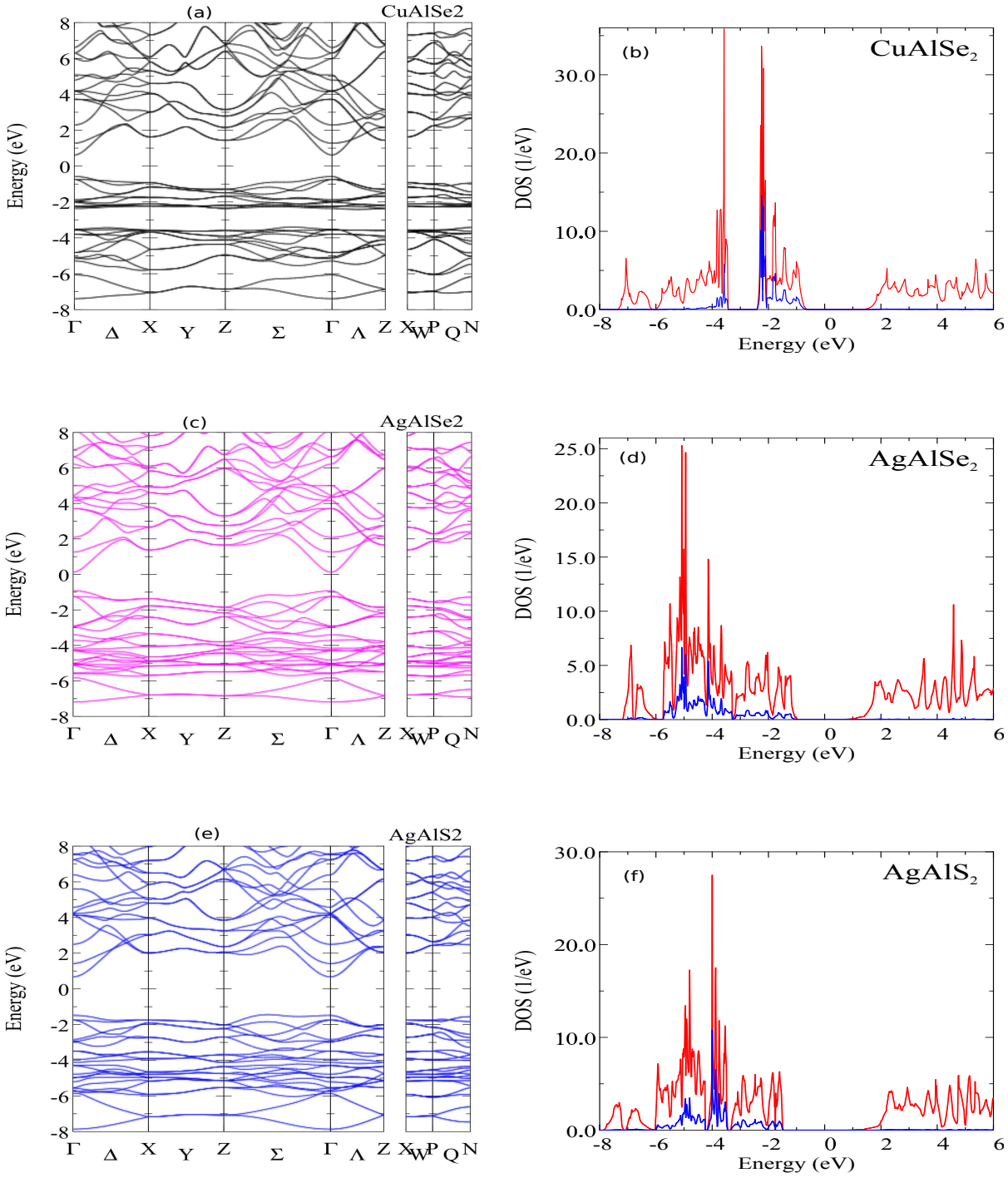

Fig. 3.4 Band structures along symmetric k points in Brillouin zone and total and partial density of states (DOS) of $CuAlSe_2$ (a) and (b), $AgAlSe_2$ (c) and (d), and $AgAlS_2$ (e) and (f). In DOS mode, red curves are total DOS and blue curves are Cu or Ag d DOS.

Electronic band structures and DOS calculated by FLAPW method are shown in

Fig. 3.4 (a-f). The bands and states below (above) the energy gap indicate the valence (conduction) bands and states, respectively. The band gaps are seen to be direct, because the maximum (minimum) filled (empty) valence (conduction) bands produce at the same symmetric k points of the first Brillouin zone (BZ). The Greek letters denote the k points inside the BZ and the Latin letters for the k points at the zone boundary. Γ is the zone center. The BZs are constructed by bisecting lines connected to the symmetry points. The BZs are simply polygon type. The lines continuity between two k points is done by extrapolation. The s and p bands are mostly dispersive (curly), parabolic and inverse parabolic style, whereas the flat bands denote the localized d (or f) band type. Due to hybridization, some mixed bands are appeared just below and onwards the energy gap. The FLAPW calculated energy gaps are well underestimated from the experimental values. In $CuAlSe_2$ calculated energy gap is 1.2 eV, where more than a half of the measured energy gap is underestimated by FLAPW based DFT calculation, i.e., mainly for GGA type exchange-correlation of electrons. Calculated energy gaps in $AgAlSe_2$ and $AgAlS_2$ are 1.04 eV and 2.15 eV, respectively.

In tetragonal structure each group VI anion (S, Se) is coordinated tetrahedrally with two group I cations (Cu, Ag) and two group III cations (Al, In) by a local distortion (inner) parameter u. Alternatively, each cation also bonded by four anions. The tetragonal ratio (due to tetragonal distortion of unequal bond lengths) η=$c/2a$ is greater than one in $CuInS_2$ and less than one in the remaining host systems.

3.5 Electronic Charge Density

Electronic charge densities, in units of e/a.u.^{3}, of the three electronic sub-bands of $CuInS_2$ are sketched in **Fig.** 3.5, where a plane is sliced to understand the nature of the charge polarization and bondings. The contours are linearly spaced, the central solid areas denote the atomic cores, where the charge density [7] vary rapidly. Sulfur is bonded with indium and copper and more closer to copper cation. The shading surrounding the contours noted the partial or weak bonding of charges. The remaining blue space is empty, having quite low electronic charge, as shown in the adjacent scale.

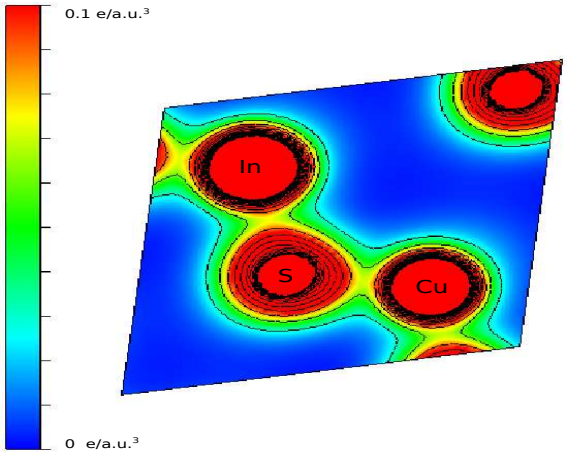

Fig. 3.5 Planar view of electronic charge density in units of e/a.u.^{3} in chalcopyrite $CuInS_2$.

Thereafter, in subsequent two chapters, we calculate dilute magnetic states by substitutional CPA and supercell doping of (i) one impurity atom, and (ii) codoping by two magnetic atoms. The doped compounds are calculated in the framework of chalcopyrite structure. The experimental lattice parameters including anion sublattice parameter of host semiconductors are used throughout the calculation.

3.6 References

[1] International Tables for Crystallography, Vol. A, Kluwer academic pub., London (1996).

[2] N.W. Ashcroft and N.D. Mermin, Solid State Physics, Brooks/Cole, USA (1976).

[3] R.W.G. Wyckoff, Crystal Structures, 2nd ed. Vol. **2**, John Wiley & Sons, Inc (1964).

[4] H. Hahn, G. Frank, W. Klingler, A.-D. Meyer and G. Störger, Z. Anorg. Chem. **271**, 153 (1953).

[5] S.C. Abrahams and J.L. Bernstein, J. Chem. Phys. **59**, 5415 (1973).

[6] S.R. Hall and J.M. Stewart, Acta Crystallogr., Sect. B: Struct. Crystallogr. Cryst. Chem. **B29**, 579 (1973).

[7] J.E. Jaffe and A. Zunger, Phys. Rev. B **28**, 5822 (1983).

[8] H. Xiao, J. Tahir-Kheli, and W. A. Goddard, J. Phys. Chem. Lett. **2**, 212 (2011).

[9] K. Sato, P.H. Dederichs and H. Katayama-Yoshida, Europhys. Lett. **61**, 403 (2003).

[10] H. Akai, Phys. Rev. Lett. **81**, 3002 (1998).

Chapter 4

Ferromagnetic Half Metals

Ferromagnetic (FM) states may be obtained by doping $3d$ transition-metals (TM) at group III site of chalcopyrite semiconductors $CuInS_2$, $CuAlSe_2$, $AgAlSe_2$ and $AgAlS_2$. Calculated FM states have spontaneous vector magnetizations parallel to the local spin moments. The stability of FM states are compared with the corresponding disordered spin moment (DSM) state. Both FM and DSM states are treated by the coherent potential approximation. FM states are realized by either double exchange or p-d hybridization with the neighbor anion p states. FM metallic states produce up-spin and down-spin bands at the Fermi level, whereas FM half metallic states [1] are fully spin polarized with an insulating gap at the minority spin channel.

4.1 Mechanism

In this section, we explain the underlying mechanism occurring FM states and half metallicity. The concept of half metallicity, crystal field effect, and the relative stability of a ferromagnetic state can be explained by coupling mechanisms and hybridization scheme between the magnetic ionic states as well as with the anion p states [2-5]. Typically we consider magnetic ions, say Cr and Ni having valence d electrons less and more than half filled, respectively. Although d electron oxidation states vary from system to system, we can assume that when Cr and Ni impurity randomly mixed at the Al^{3+} site, trivalent states of Cr^{3+} (d^3) and Ni^{3+} (d^7) are realized. The schematic density of

states (DOS) of a ferromagnetic half metal (FHM) and metallic DSM states around the Fermi energy are shown in **Fig.** 4.1 (a). Relative total energies of FHM and DSM states indicate which magnetic phase is stable. Ligand field effects of $3d$ band splitting and p-d hybridization with anion p states are schematically shown in **Fig.** 4.1 (b). In the tetrahedral splitting of d orbitals, $3d\gamma$ orbitals (e_g) are energetically lower than $3d\varepsilon$ orbitals (t_{2g}), and the wave functions of triply degenerate $3d\varepsilon$ states hybridize well with the anion Se $4p$ states, producing bonding (t^b) and anti-bonding (t^a) states. On the other hand, doubly degenerate $3d\gamma$ states have less hybridization and are rather localized, remaining as nearly non-bonding (e_g) states.

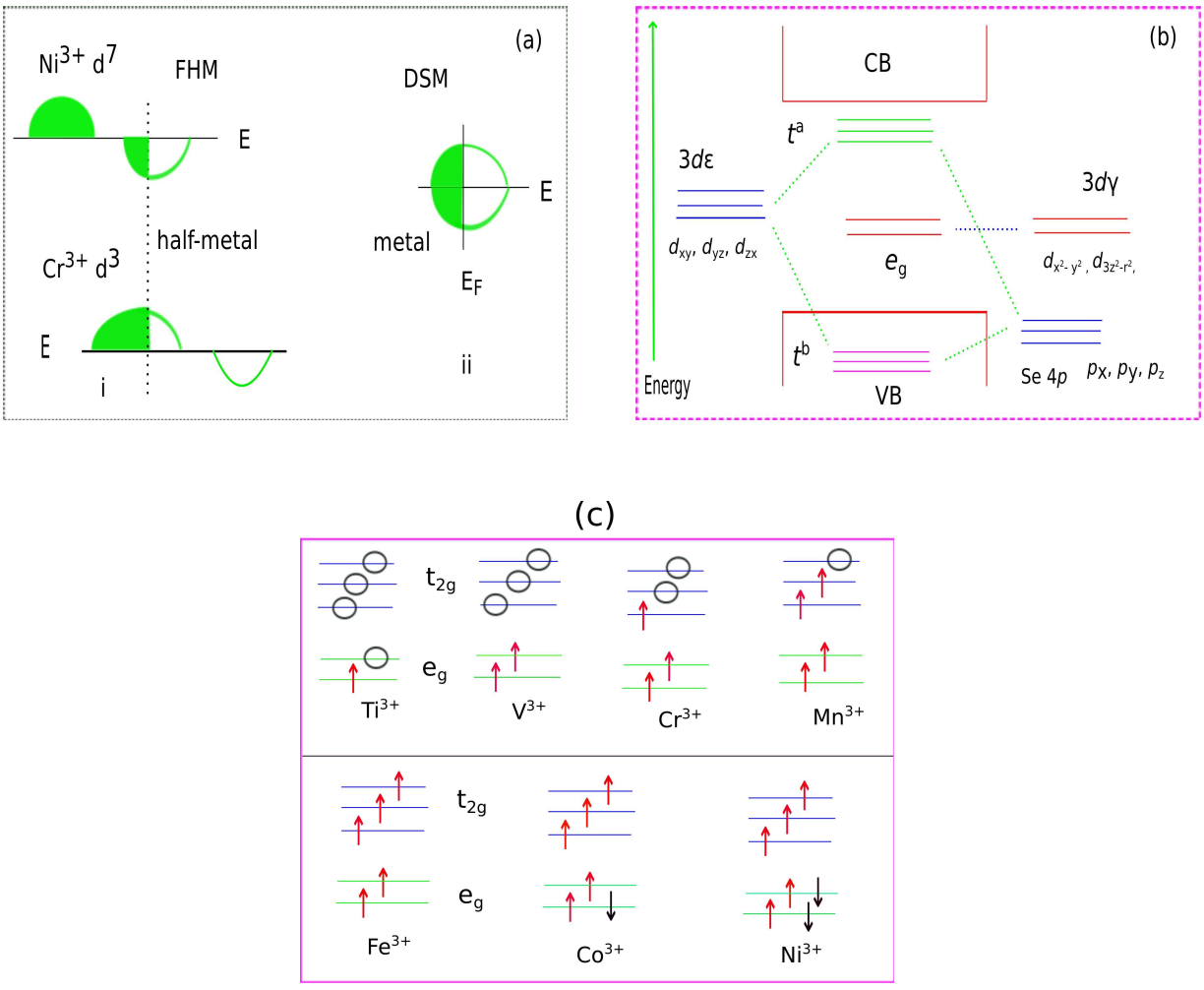

Fig. 4.1 (a) i) Schematic impurity density of states, which is half metallic, and ii) metallic disordered spin moment state. (b) Splitting of $3d$ bands due to ligand field and p-d hybridization. (c) Schematic picture of impurity ions and high spin configurations.

The high spin configuration is pictured in **Fig.** 4.1 (c), which denotes the splitting of $3d$ spin bands due to ligand field and p-d hybridization, where the up and the down arrows indicate up spin and down spin electrons, respectively, otherwise $3d$ holes. While t_{2g} orbitals well hybridize with neighboring p orbitals of the anions, e_g orbitals are well localized.

Table 4.1 Summary of iron (ferrum) group ions (triply ionized) basic electron configurations and **dominating mechanism** [2], namely double-exchange (DX), super-exchange (SX) and p-d hybridization in stabilizing either ferromagnetic (FM) or disordered spin moment (DSM) (a paramagnetic) state in group I-III-VI_2 based chalcopyrite semiconductors.

ions	Ti^{3+}	V^{3+}	Cr^{3+}	Mn^{3+}	Fe^{3+}	Co^{3+}	Ni^{3+}
config.	$3d^1$	$3d^2$	$3d^3$	$3d^4$	$3d^5$	$3d^6$	$3d^7$
DX/p-d	FM	—	FM	FM	—	—	—
SX	—	FM	—	—	DSM	DSM	FM/DSM

The basic electron configurations of triply ionized $3d$ TM in solid is shown in **Table** 4.1, where Fe has the half filled d^5 electron configuration and in fact having no mobile carriers for conduction. According to Hund's rule, total spin is S=5/2 in the high spin configuration and total orbital angular momentum L=0. Otherwise, Ti, V, Cr, and Mn have less than half filled configuration with d electrons or holes as carrier for conduction. On the contrary, Co and Ni have more than half filled d electrons where the 6^{th} or 7^{th} d electrons are of e_g type, rather localized and less effective for conduction. Detailed crystal field effects and electronic states can be understood from **Fig.** 4.1 (a-c) for doping impurities at triply ionized site, whereas **Table** 4.1 summarizes the underlying mechanisms which stabilize the dilute magnetic states in FM or DSM state [2].

(**see § 2.8 for magnetic couplings in DMS.**)

4.2 Copper Aluminum Diselenide $CuAlSe_2$

4.2.1 *Electronic Structures*

To obtain a stable magnetic ordering, one type of low-concentration (here 10%) magnetic ion is randomly introduced into the host material $CuAlSe_2$ at Al site. Electronic states of these disordered compounds are calculated for the following cases and compared their total energies to obtain the magnetic ground state: (i) local spin moments oriented in the same direction (FM state), and (ii) local spin moments aligned randomly (DSM state).

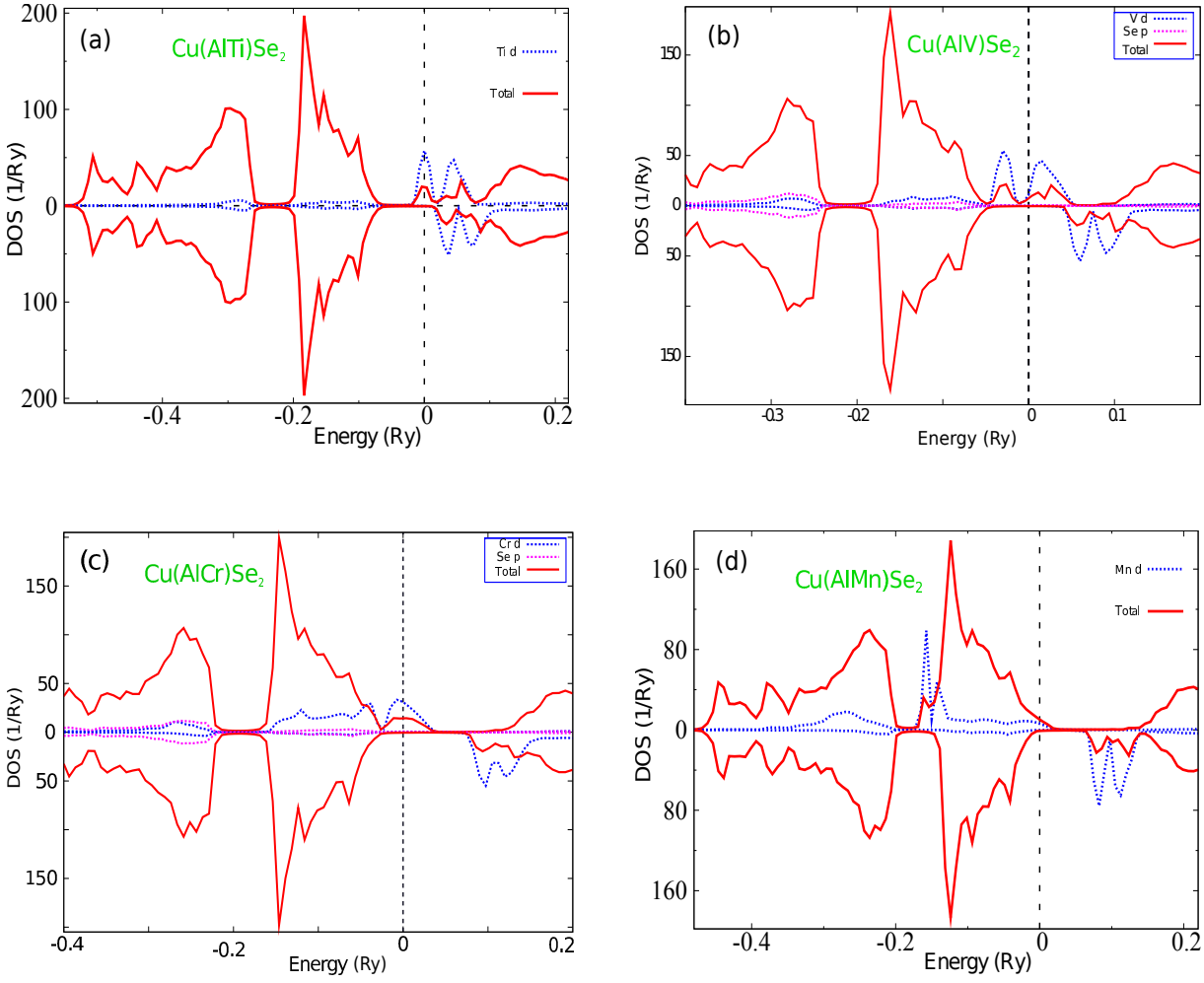

Fig. 4.2 Total density of states (DOS) per cell and local *d* DOS per atom for doping of (a) Ti, (b) V, (c) Cr, and (d) Mn, at host Al site. Vertical broken lines denote the Fermi energy.

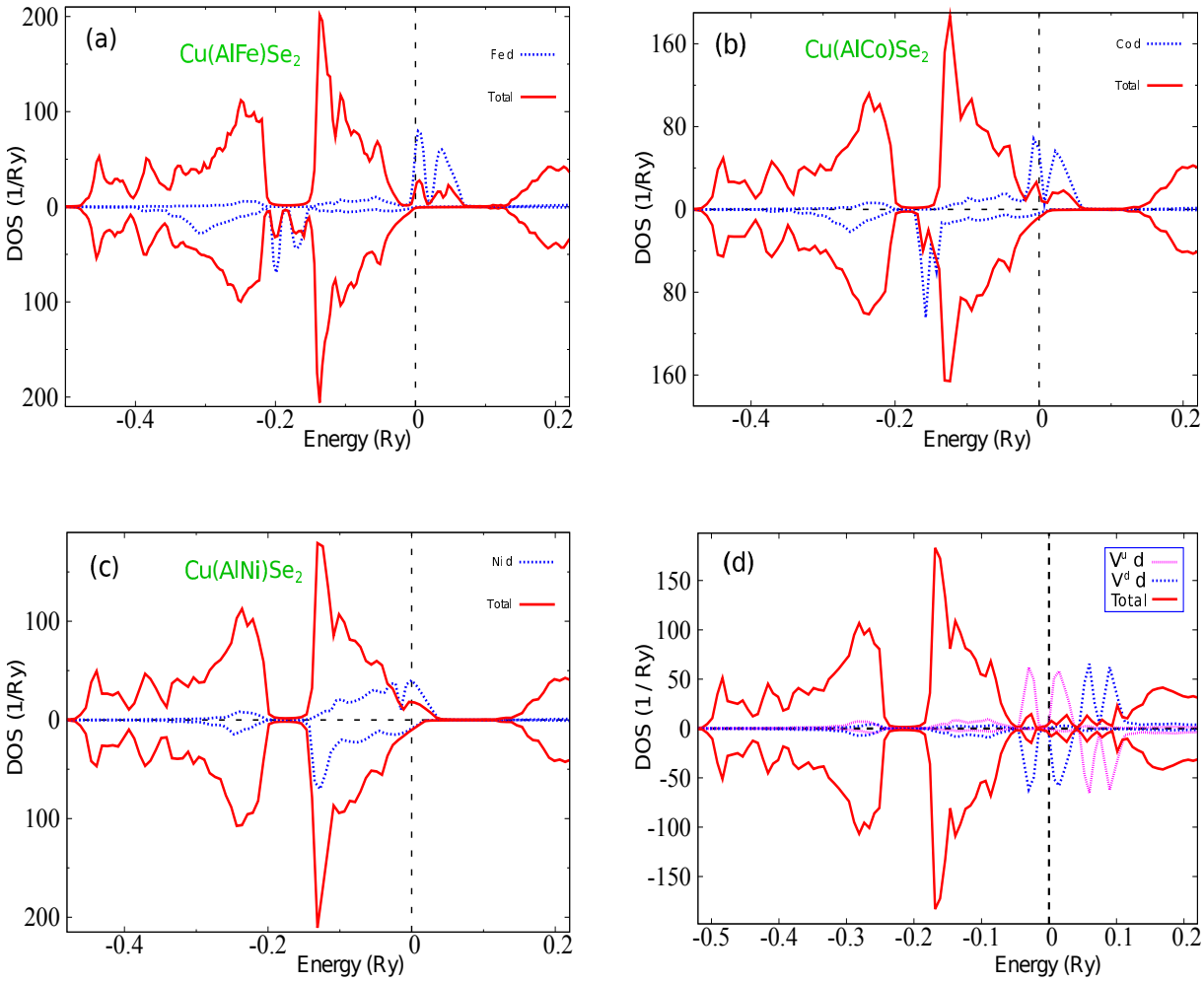

Fig. 4.3 Total density of states (DOS) per cell and local d DOS per atom for doping of (a) Fe, (b) Co, and (c) Ni at host Al site. (d) DOS of a typical disordered spin moment state. Vertical broken lines denote the Fermi energy.

FM states are lower in energy for Ti, V, Cr, and Mn doped cases, while Fe, Co, and Ni doped alloys are instable ferro-magnetically, as listed in **Table** 4.2. **Figures** 4.2 (a-d) show calculated DOS for those systems having a stable FM state. The expected configurations of d electrons of the doped A^{3+} cations in FM states are d^1 - d^4, being less than half filled situations. In these cases either e_g state or t_{2g} state is incomplete and contribute either holes or electrons as d carriers in the system for conduction. In FM cases, the d states become widen and decreases the total energy relative to the corresponding DSM state. The energy gain due to such band widening stabilizes the FM states by the double-exchange mechanism. In Ti doped system, majority e_g state

incomplete, while in V doped case it is filled and majority t_{2g} state empty. In V doped case, the coupling between $e_g^{\uparrow}$-$t_{2g}^{\uparrow}$ states results in shifting of majority e_g state to lower energy region and stabilized by FM super-exchange mechanism. Therefore, stable FM states can be obtained either by double-exchange caused by the d carriers or Zener's p-d hybridization or super-exchange coupling [2-6]. The FM states realize the half metallicity by forming simultaneously a semiconducting band gap in the minority spin channel and metallic bands in the majority spin channel, mostly evolved from the doping ions.

The electron configurations of the doped Fe^{3+}, Co^{3+}, and Ni^{3+} are d^5, d^6, and d^7, respectively. For half filled d^5 case (e.g. Fe^{3+}) there is no majority and minority spin carriers for conduction, where antiferromagnetic super-exchange (ASX) coupling [2-6] stabilizes the DSM state, as shown in **Fig.** 4.3 (a-c). Similarly, for d^6 case minority e_g state incomplete and for d^7 case the minority e_g state filled and minority t_{2g} state empty. In these case the $3d$ carriers are mainly $3d\gamma$ orbital and their wave functions are well localized and less effective for conduction, therefore ASX coupling prevails to stabilize them in DSM state. In the present calculation, DSM state is manifested as $Cu(Al_{0.90}A_{0.05}^{\uparrow}A_{0.05}^{\downarrow})Se_2$ which usually simulates a disordered paramagnetic state as shown in **Fig.** 4.3(d).

To confirm some of the above results, we perform supercell (treated as ordered system) calculations with the FLAPW method. We construct a 32 atoms (4 times bigger than host system) supercell, which has eight Al atoms and one of the Al atoms is substituted by $3d$ TM. As a result, We have a supercell with 12.5% doping concentrations of impurity atoms. The TM doped supercell calculations, shown in **Fig.** 4.4, of $Cu(AlCr)Se_2$ gives a half-metallic band structure with impurity spin moment inside MT is 2.76 μ_B/atom and total spin moment = 3 μ_B/cell. The minority spin channel exhibits an energy gap of 1.16 eV. In contrast, $Cu(AlV)Se_2$ provides a FM insulating band structure with V spin moment inside MT = 1.74 μ_B/atom and net spin moment= 2 μ_B/cell. In this case, we obtained energy gaps at majority channel = 0.42 eV and minority channel =1.15 eV.

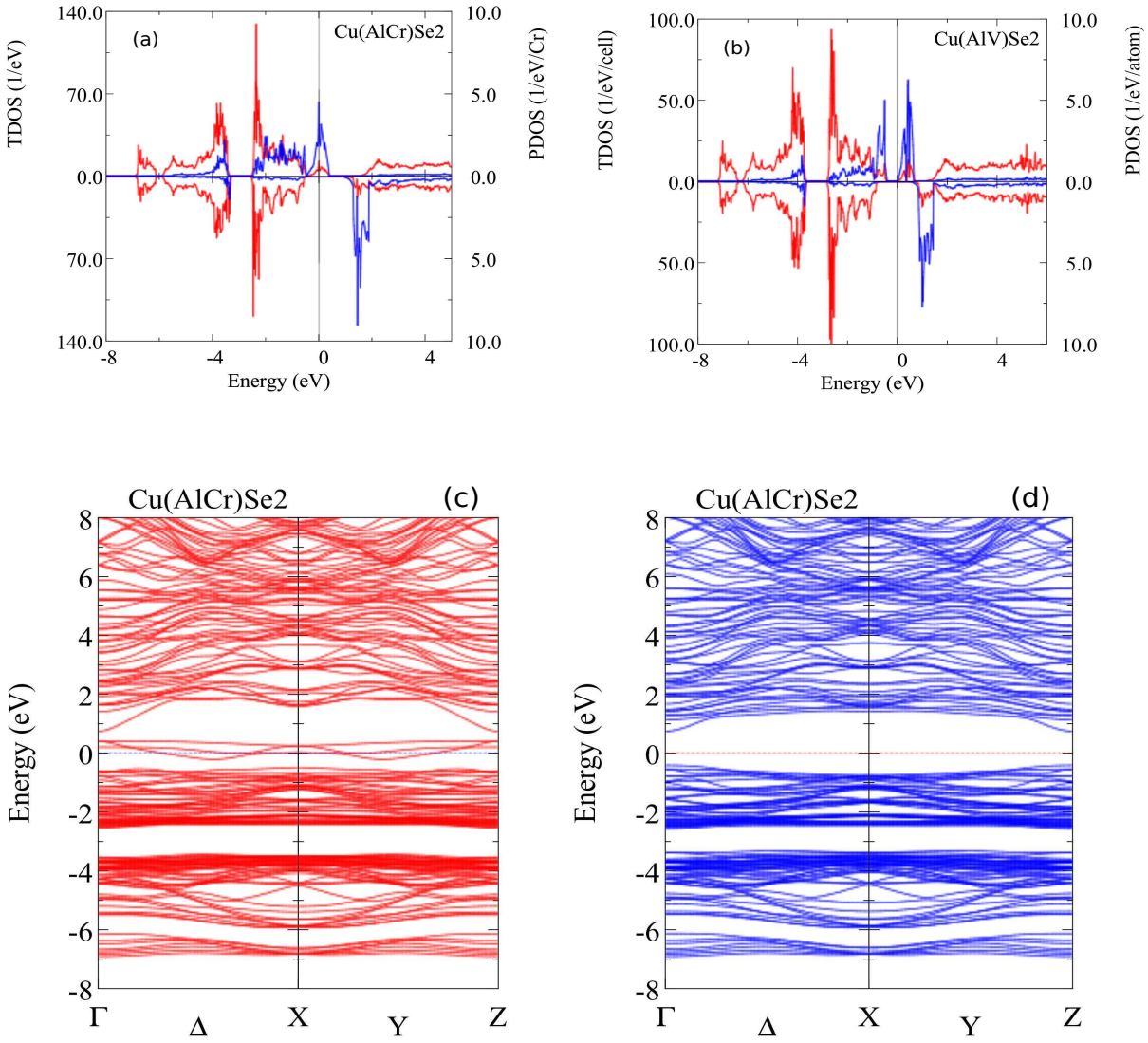

Fig. 4.4 Total density of states (DOS) per cell and local *d* DOS per atom for doping of (a) Cr, and (b) V, at host Al site, where the band structures are ferromagnetic half metallic and insulating, respectively. Band structures for (c) majority spin, and (d) minority spin in Cr doped supercell. The energy zero is taken at the Fermi level.

4.2.2 *Comparison of Two Methods in Results*

In order to check the numerical accuracy of CPA and MT potential, we have performed supercell calculations using FLAPW method. To make a crude comparison, two methods are used to see the effects of full-potential method and a type of ordered calculation using supercell over the MT potential and disordered calculation by CPA treatment. We found general agreement in the cases of some dopants namely Ti, Cr, Mn, etc., and slightly different behaviors in few cases. A typical example is V doped (group I-III-VI_2) chalcopyrite, for which KKR-MT-CPA and FLAPW-supercell calculations of DOS give FHM and FM insulator, respectively. In V doped system, majority e_g state is fully filled and majority t_{2g} state is empty. Therefore, the coupling between $e_g^{\uparrow}$-$t_{2g}^{\uparrow}$ states results in shifting of majority e_g state to lower energy region by broadening the bands relative to the corresponding DSM state. The magnetic phase thus stabilized through energy gain by the FM super-exchange coupling. Such a band broadening by disorder is missing in FLAPW-supercell case. Because KKR-CPA results are for a disordered system, where bands are broadened by mixing and hybridization, whereas FLAPW-supercell ones for an ordered state and no such band broadening may be realized.

4.2.3 *Magnetic Properties*

There are several approximation methods available for computing magnetic transition temperature. Mean field approximation (MFA) (a brief derivation is given in **Appendix A**) is one of them, which is exploited in the present calculation. MFA gives an average (gross) picture of the critical region. Despite inadequacies (limited accuracy) at low temperatures, MFA offers the simplest approach in confronting a sophisticated spin orderings in a crystal with several types of magnetic coupling.

Table 4.2 Total magnetic moments ($M_{\rm T}$), local spin moments (SM), total hyperfine fields ($H^{\rm t}_{\rm hf}$) at impurity site, magnetic Curie temperatures ($T_{\rm C}$) estimated by MFA and the energy difference $\Delta E(x)$ between DSM and FHM state for a series of transition metal doped compounds.

Composition	$M_{\rm T(\mu_B/cell)}$	SM$_{(\mu_{\rm B}/{\rm ion})}$	$H^{\rm t}_{\rm hf(KG/ion)}$	$\Delta E_{\rm (mRy/cell)}$	$T_{\rm C}^{\rm MFA}{}_{\rm (K)}$
$Cu(Al_{0.90}Ti_{0.10})Se_2$	0.22	0.74 (Ti)	−60.45 (Ti)	0.253	267
$Cu(Al_{0.90}V_{0.10})Se_2$	0.44	1.85 (V)	−139.71 (V)	0.328	345
$Cu(Al_{0.90}Cr_{0.10})Se_2$	0.65	3.03 (Cr)	−217.73 (Cr)	0.677	713
$Cu(Al_{0.90}Mn_{0.10})Se_2$	0.88	3.79 (Mn)	−245.51 (Mn)	0.675	710
$Cu(Al_{0.90}Fe_{0.10})Se_2$	0.92	3.22 (Fe)	−189.63 (Fe)	−0.825	–
$Cu(Al_{0.90}Co_{0.10})Se_2$	0.59	2.07 (Co)	−126.67 (Co)	−0.121	–
$Cu(Al_{0.90}Ni_{0.10})Se_2$	0.30	0.84 (Ni)	−54.32 (Ni)	−0.258	–

The total energy (a derivation is given in **Appendix A**) difference $\Delta E(x) = E^{\rm DSM} - E^{\rm FM}$ per unit cell between DSM and FM states is exploited to estimate the magnetic critical temperatures in MFA [7] as

$$T_{\rm C}^{\rm MFA}(x) = \frac{2\,\Delta E(x)}{3x\,k_{\rm B}} \tag{4.1}$$

where x is the impurity concentration and $k_{\rm B}$ is the Boltzmann constant. The estimated Curie temperatures $T_{\rm C}$ are listed in **Table** 4.2, which are above room-temperature for V, Cr, and Mn doped compounds. FM state is stable in Ti doped case with $T_{\rm C}$ slightly lower than room temperature, possibly due to a low carrier ($e_{\rm g}$) of d electrons.

The concentration dependence of the magnetic properties such as net magnetizations, local spin moments, total HF and magnetic critical temperatures of the doped compounds are listed in **Table** 4.2 at the TM concentration of x=10%. Relatively larger net moments, spin moments and HF are obtained in Cr, Mn and Fe doped compounds. Total HF of the impurity sites can be measured by nuclear magnetic resonance (NMR) or Mössbauer spectroscopic experiment [8]. As the Fermi contact term is dominated in the HF of the present systems, the HF are directly proportional to the spin density (s states) at the nuclear position.

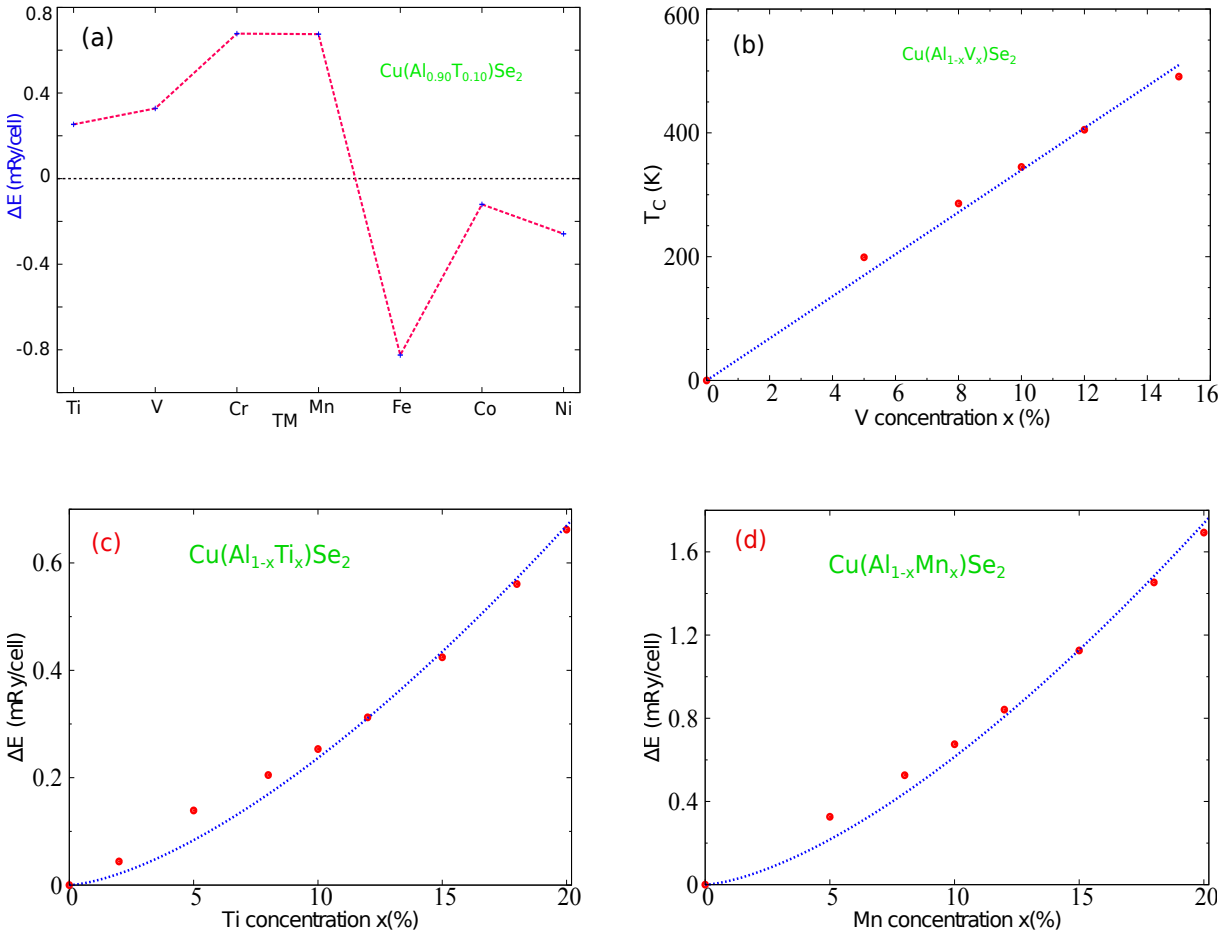

Fig. 4.5 Chemical trends on (a) stability of magnetic states, (b) critical temperatures in V doped case, and magnetic behaviors in (c) Ti, and (d) Mn doped cases with concentrations.

According to our choice of reference level, positive energy difference in **Fig.** 4.5 (a) denote the stable FM states, otherwise the DSM state is the minimum energy state. According to expression (4.1), if $\Delta E(x)$ vary quadratically then $T_{\rm C}$ would be linear with concentration, and if $\Delta E(x)$ vary as third power of square root of concentration then $T_{\rm C}$ would be square root of it. The total energy difference versus concentration curves in **Figs.** 4.5 (c), and (d) well fitted as $x^{3/2}$, indicating that double-exchange mechanism is effective to stabilize the FM states. On the other hand, in V doped case, **Fig.** 4.5 (b), $T_{\rm C}$ fitted linearly with impurity concentrations and thus FM super-exchange would dominate. (**see § 2.8 for the mechanism of exchange couplings.**)

4.2.4 Energy of Formation

Exemplary formation energy calculations using KKR-CPA and FLAPW methos are given below. In KKR-CPA, we dope x=5% V at Al site in $CuAlSe_2$ and calculate total energy, while the host and elements total energy are calculated without CPA. We assume a uniform mixing of dopant at the host matrix by excluding spatial, temporal, and thermal fluctuations. This corresponds to a MFA, also known as Bragg-Williams approximation (BWA). The energy of mixing (parabolic in concentration) in BWA seems mild.

$$\Delta H_{\mathrm{f}}^{\mathrm{KKR}} = \mathrm{E}[\mathrm{Cu}(\mathrm{Al}_{1-\mathrm{x}}\mathrm{V}_{\mathrm{x}})\mathrm{Se}_2 - [\mathrm{E}(\mathrm{CuAlSe}_2) - \mathrm{xE}(\mathrm{Al}) + \mathrm{xE}(\mathrm{V})] \tag{4.2}$$

$$= \mathrm{E}[\mathrm{Cu}(\mathrm{Al}_{0.95}\mathrm{V}_{0.05})\mathrm{Se}_2] - [\mathrm{E}(\mathrm{CuAlSe}_2) - 0.05\mathrm{E}(\mathrm{Al}) + 0.05\mathrm{E}(\mathrm{V})] \tag{4.3}$$

$$= 7.468 \text{ mRy/f.u.} = 0.102 \text{ eV/f.u.} \tag{4.4}$$

In FLAPW, we construct a supercell of 32 atoms and calculate the total energy of doped supercell, host material and elements. We replace one of the eight Al atoms in the supercell by a V atom, and this give rise to a 12.5% composition of magnetic atom.

$$\Delta H_{\mathrm{f}}^{\mathrm{FLAPW}} = \mathrm{E}[\mathrm{Cu}_8(\mathrm{Al}_7\mathrm{V})\mathrm{Se}_{16}] - [\mathrm{E}(\mathrm{Cu}_8\mathrm{Al}_8\mathrm{Se}_{16}) - \mathrm{E}(\mathrm{Al}) + \mathrm{E}(\mathrm{V})] \tag{4.5}$$

$$= 0.0856 \text{ Ry/V} = 1.165 \text{ eV/V} \tag{4.6}$$

$$\Delta H_{\mathrm{f}}^{\mathrm{FLAPW}} = \mathrm{E}[\mathrm{Cu}_8(\mathrm{Al}_7\mathrm{Ti})\mathrm{Se}_{16}] - [\mathrm{E}(\mathrm{Cu}_8\mathrm{Al}_8\mathrm{Se}_{16}) - \mathrm{E}(\mathrm{Al}) + \mathrm{E}(\mathrm{Ti})] \tag{4.7}$$

$$= 0.0263 \text{ Ry/Ti} = 0.358 \text{ eV/Ti} \tag{4.8}$$

In both cases enthalpy of formations are rather small and positive, indicating that doped compound might segregate to other phases at 0 K, but would be stabled through entropy at some higher temperatures (around 10^3 K). In some entropic state, the alloy favors toward the material fabrication. Moreover, the relative elements are taken as bcc V, fcc Al and hcp Ti for total energy calculation.

4.3 Silver Aluminum Diselenide $AgAlSe_2$

4.3.1 *Electronic Structures*

Following $CuAlSe_2$, electronic structures of silver based chalcopyrite $AgAlSe_2$ are calculated by doping one impurity ion at Al^{3+} site at 10% concentration of dopant.

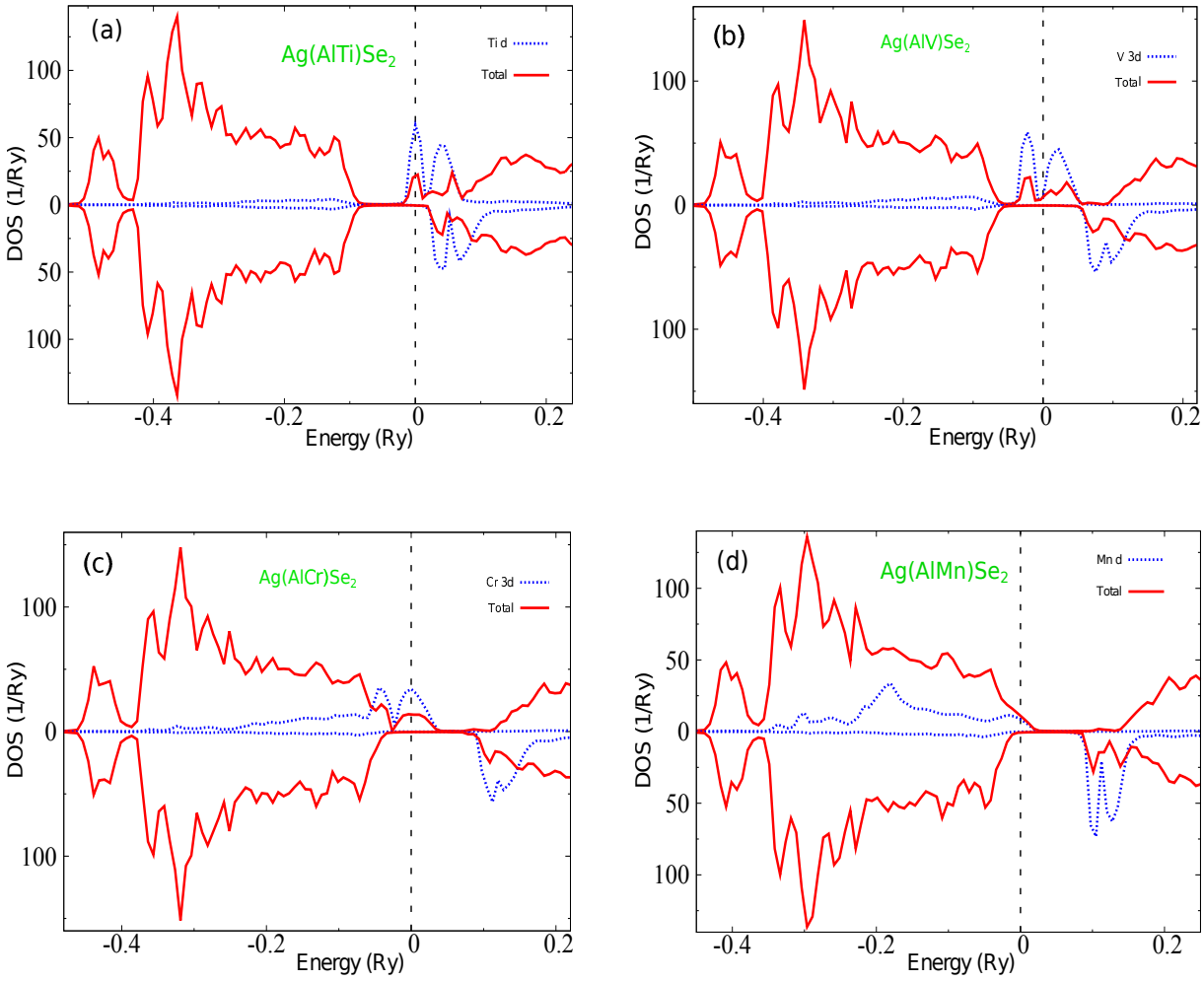

Fig. 4.6 Total density of states (DOS) per cell and local d DOS per atom for doping of (a) Ti, (b) V, (c) Cr, and (d) Mn at Al site of host $AgAlSe_2$, where ferromagnetic state is the ground state. The energy zero is taken at the Fermi level.

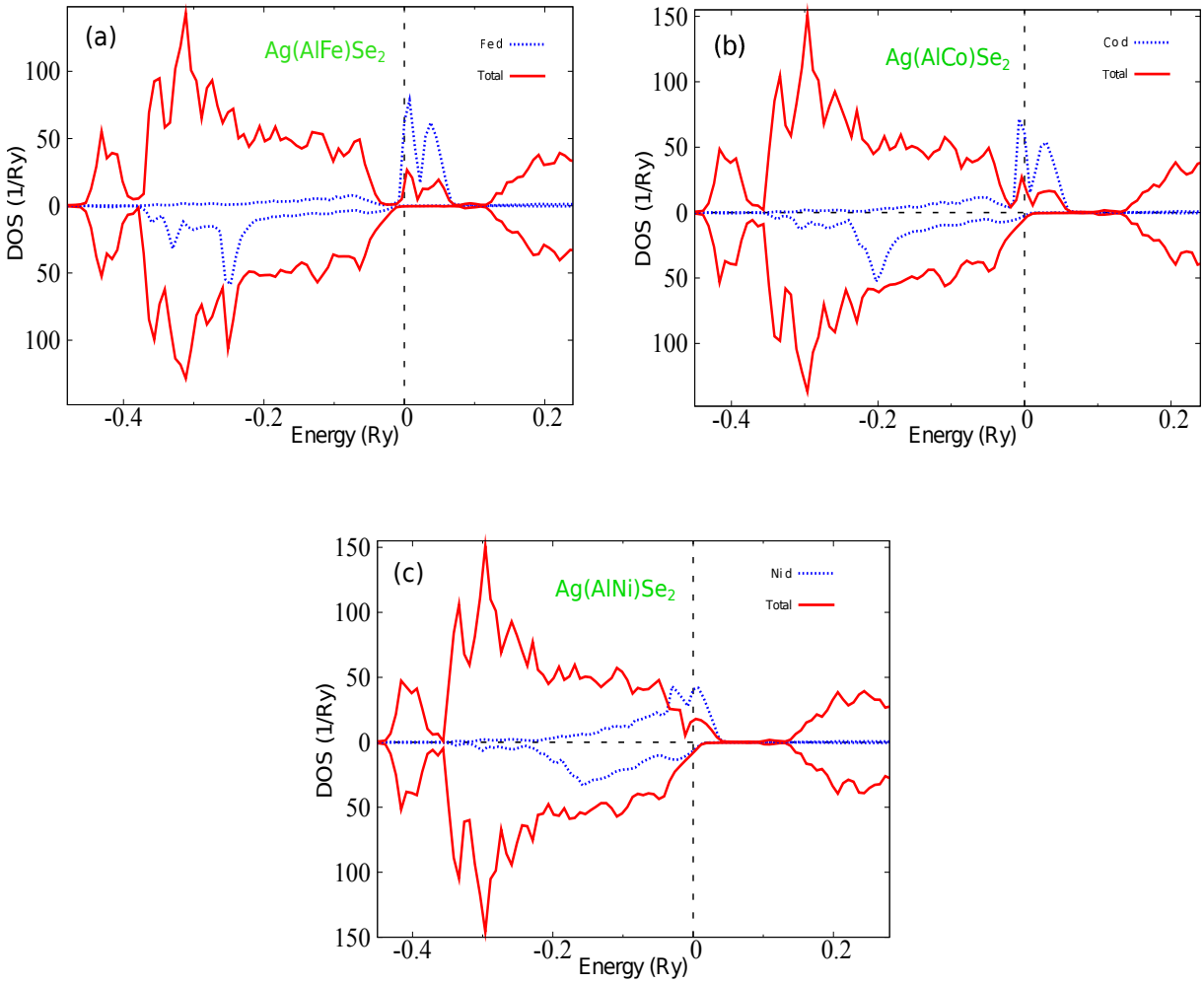

Fig. 4.7 Total density of states (DOS) per cell and local d DOS per atom for doping of (a) Fe, (b) Co, and (c) Ni at Al site of host $AgAlSe_2$, where disordered spin moment (DSM) state is the ground state. Vertical broken lines denote the Fermi energy.

KKR-CPA calculation of electronic states in V, and Ni doped cases are FM half-metallic and AF metallic as shown in **Fig.** 4.6(b) and **Fig.** 4.7(c), respectively. Ti, V, Cr, and Mn doped systems are stable at FM state, whereas Fe, Co, and Ni doped compounds are instable at FM state, where super-exchange coupling may lead them to a disordered paramagnetic ground state. Mn doped case in **Fig.** 4.6(d), rather small majority t_{2g} state produce a common total band at up spin direction and zero band at down spin channel, therefore FM half-metallic state is stable by double-exchange coupling. Total DOS (solid red curves) is the aggregate of all host and impurity local DOS, and the high peaked total DOS are mainly a contribution of localized partial d DOS of host Ag.

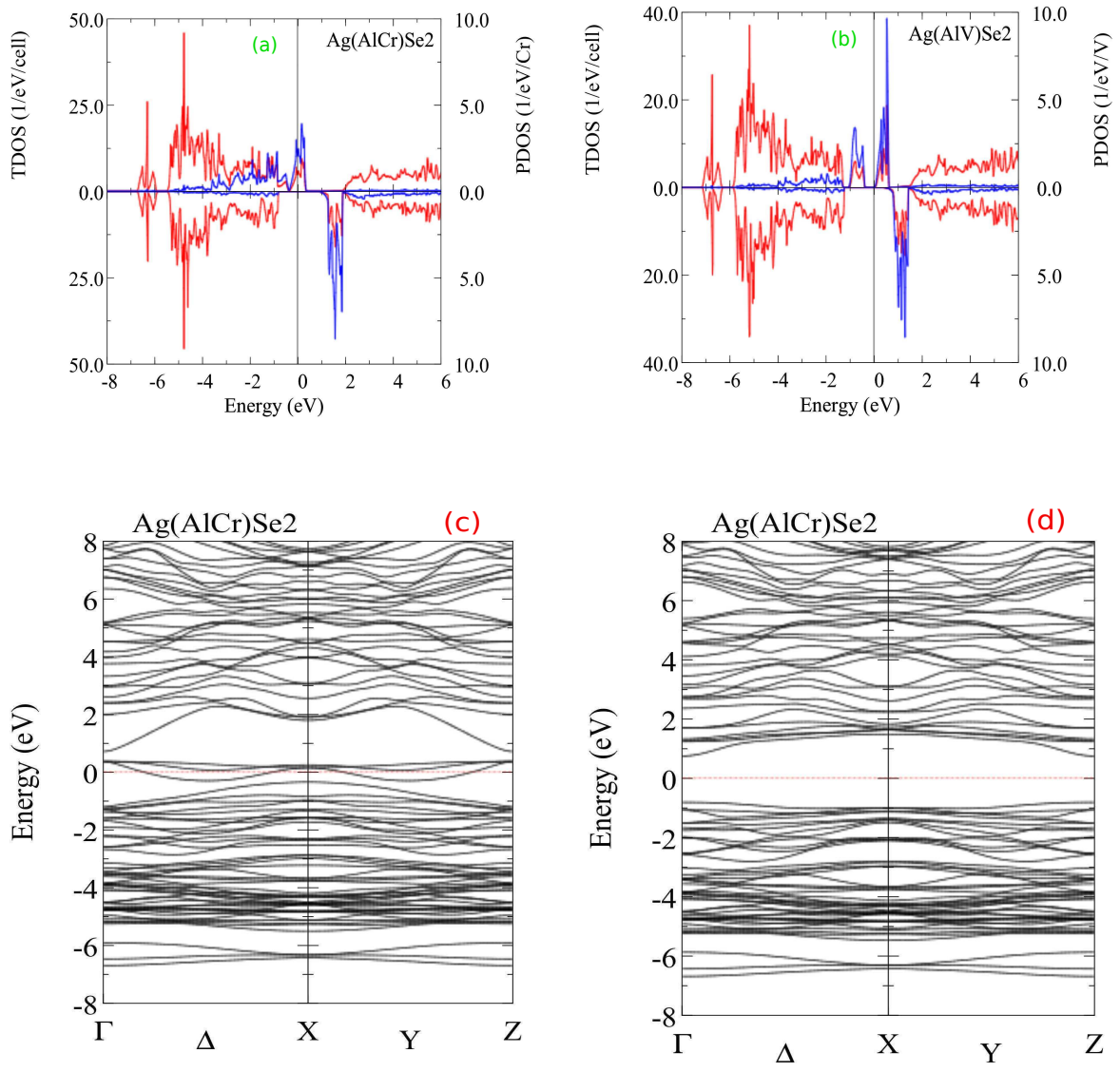

Fig. 4.8 Total density of states (DOS) per cell and local d DOS per atom for doping of (a) Cr, (b) V in $AgAlSe_2$ and band structures for (c) up spin, and (d) down spin in the Cr doped supercell, where half metallicity at ferromagnetic state is found, in contrast to the insulating electronic structure in V doped case. The energy zero is taken at the Fermi level.

Both DOS and band structures in **Fig.** 4.8 (a, c, d) for Cr doped supercell calculation proof the half metallicity in $Ag(AlCr)Se_2$, where two up spin bands are partially occupied and all the down spin bands are fully occupied and thus valence band maximum is separated from the conduction band minimum with an energy gap of 1.56 eV. Net spin

moment per cell is 3 μ_B per cell and local spin moment at Cr site within the sphere is 2.68 μ_B. Inclusion of spin-orbit coupling more than 10 mRy lower total energy is obtained while SCF calculation in FLAPW method, where in addition to local spin moment the total orbital magnetic moment is 0.0124 μ_B. This extra energy can be treated as the perturbation or the interaction energy (calculated by the second-variation step) between spins and *d* orbital electrons. On the contrary, in V doped case, **Fig.** 4.8 (b), an insulating band structure is found with energy gaps at majority spin band of 0.39 eV and minority spin band of 1.56 eV. Net moment of V in the cell is 2 μ_B and local spin moment at V site is 1.70 μ_B.

4.3.2 *Magnetic Properties*

Table 4.3 Total magnetic moment (M_T), local spin moments (SM), total hyperfine fields (H_{hf}^t) at impurity site, magnetic Curie temperatures (T_C) estimated by MFA and the energy difference $\Delta E(x)$ between DSM and FHM state for a series of transition metal doped compounds.

Composition	$M_{T(\mu_B/cell)}$	$SM_{(\mu_B/ion)}$	$H_{hf(KG/ion)}^t$	$\Delta E_{(mRy/cell)}$	$T_C^{MFA}{}_{(K)}$
$Ag(Al_{0.90}Ti_{0.10})Se_2$	0.20	0.76 (Ti)	−61 (Ti)	0.497	523
$Ag(Al_{0.90}V_{0.10})Se_2$	0.42	1.92 (V)	−143 (V)	0.298	314
$Ag(Al_{0.90}Cr_{0.10})Se_2$	0.64	3.07 (Cr)	−216 (Cr)	0.695	732
$^\star Ag(Al_{0.90}Cr_{0.10})Se_2$	0.64	3.06 (Cr),−0.07* (Cr)	−215 (Cr)	0.797	839
$Ag(Al_{0.90}Mn_{0.10})Se_2$	0.86	3.88 (Mn)	−183 (Mn)	0.790	832
$Ag(Al_{0.90}Fe_{0.10})Se_2$	0.95	3.37 (Fe)	−190 (Fe)	−0.835	–
$Ag(Al_{0.90}Co_{0.10})Se_2$	0.68	2.29 (Co)	−141 (Co)	−0.318	–
$Ag(Al_{0.90}Ni_{0.10})Se_2$	0.41	1.11 (Ni)	−72 (Ni)	−0.455	–

*Calculation with inclusion of LS coupling.

Total, local and very local magnetic properties at TM doped chalcopyrite $AgAlSe_2$ are listed in Table 4.3. We see that Ti doped case T_C is higher than V doped compound, but why?. In Ti case majority e_g state is partially filled, whereas in V case majority

e_g states are filled. As a result, in Ti case hybridization is stronger than in V case. In addition, d^1 wave function is more delocalized than d^2 case, thus exchange energy coupling is higher and results in more transition temperature. Fixed spin moment (FSM) mode provides a preset net moment per cell in SCF calculation. FSM is a spin-polarized electronic structure calculation setting in a particular quantization axis. It (FSM) always neglects the orbital moments. On the contrary, spin-orbit (SO) interaction, for a typical compound calculated by KKR-CPA method shown in **Table** 4.3 as '$\star$' row, produce a small but finite orbital moment of -0.07 in addition to local spin moment and hyperfine fields for $3d$ TM, but critical temperature in SO case is found about 100 K higher than without SO interaction. Because, LS coupling energy (perturbative energy) is an additive quantity in total energy calculation, and hence the total energy difference between FM and DSM states is lower (higher) in SO coupling inclusion (exclusion) case. Therefore, LS coupling may not be neglected.

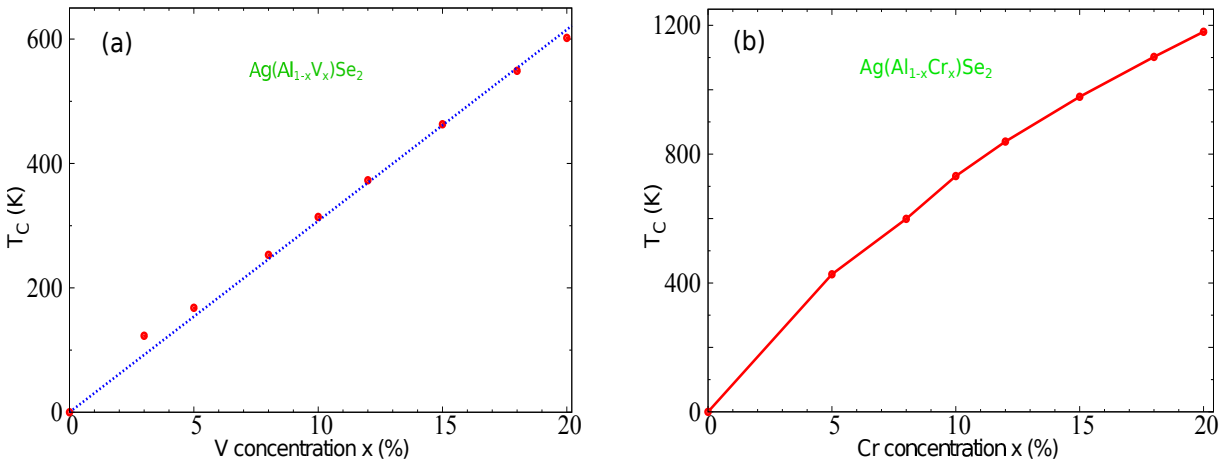

Fig. 4.9 Chemical trends on critical temperatures versus concentrations for (a) V and (b) Cr doped in $AgAlSe_2$.

The magnetic behavior, namely critical temperatures with V and Cr doping concentrations are shown in **Fig.** 4.9. Estimated Curie temperatures by MFA in V doped case is well fitted linearly and dominate to a FM super-exchange coupling, whereas in Cr doped case T_C also increases with composition and FM half metallic state is stable by double-exchange interaction.

4.4 Silver Aluminum Disulfide $AgAlS_2$

4.4.1 *Electronic Structures*

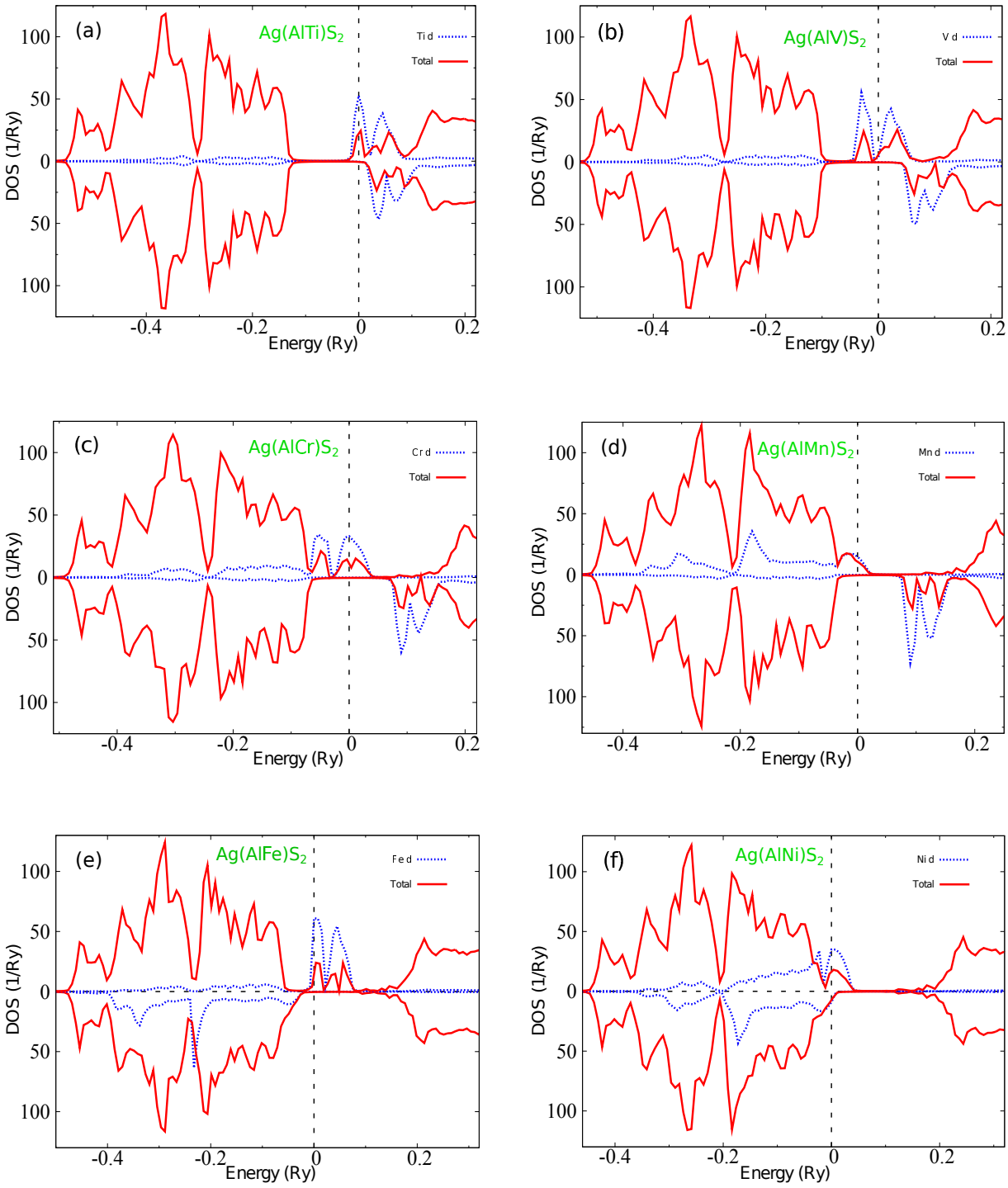

Fig. 4.10 Total density of states (DOS) per cell and local *d* DOS per atom for doping of (a) Ti, (b) V, (c) Cr, (d) Mn, (e) Fe, and (f) Ni at host Al site, where ferromagnetic states are found as the ground state, except Fe, Co, and Ni doped cases, where DSM is the ground state.

Electronic structures of silver based chalcopyrite $AgAlS_2$ doping a impurity at Al^{3+} site for 10% concentration are shown in **Fig.** 4.10 (a-f). Electronic states in Ni doped compound exhibit a FM metallic DOS, where majority t_{2g} and minority t_{2g} states have common bands at the Fermi level. Other DOS in **Fig.** 4.10 (a-d) shows a FM half metallicity with an insulating gap at the minority spin states. Spins are resolved by exchange splitting and energy of splittings slowly increases from Ti to Mn doped cases.

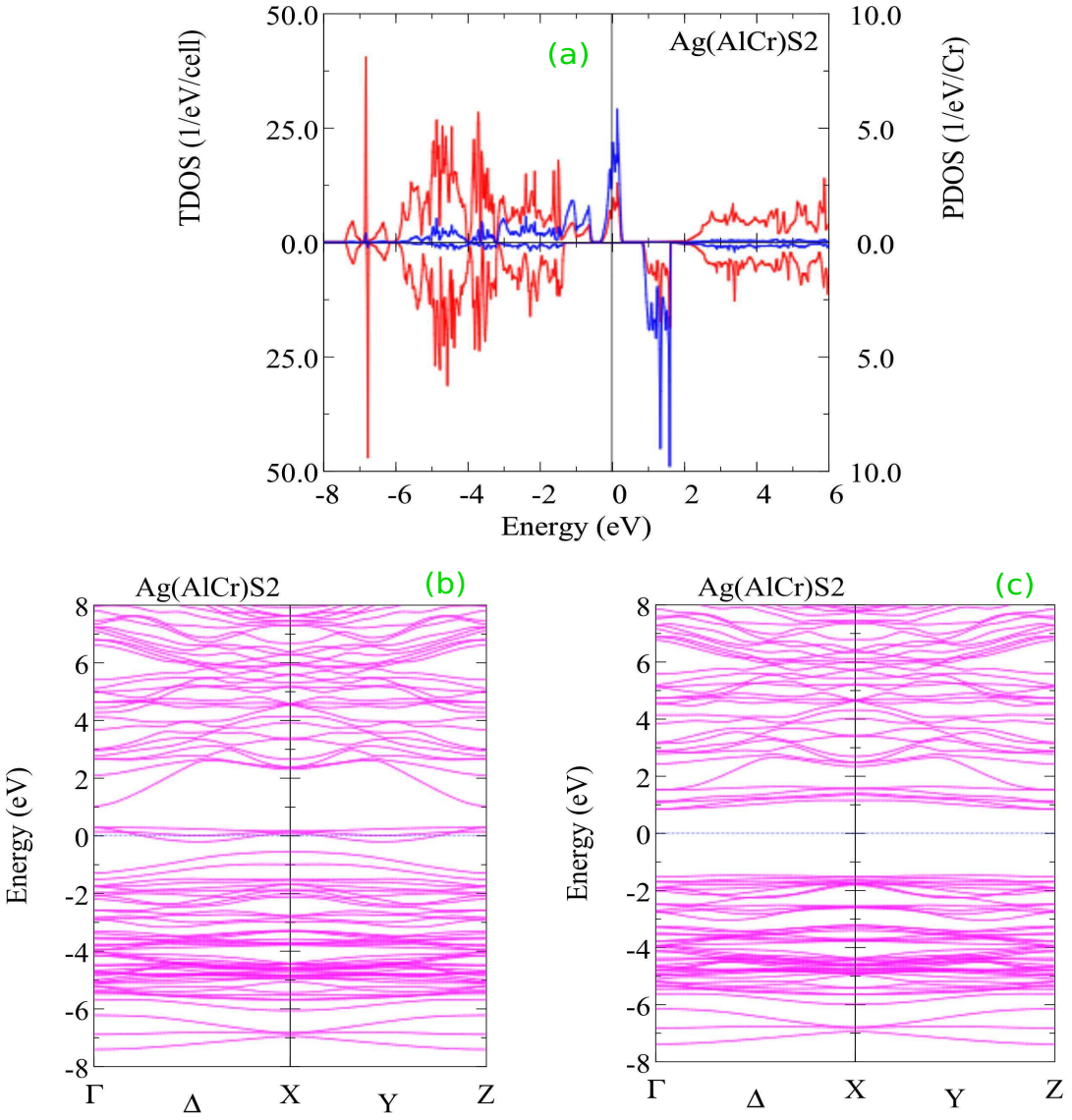

Fig. 4.11 Total density of states (DOS) per cell and local *d* DOS per atom in a supercell doping (25%) of (a) Cr in $AgAlS_2$, (b) majority spin band structure, and (c) minority spin band structure of the same supercell, where ferromagnetic state is the ground state. The energy zero is taken at the Fermi level.

FLAPW based supercell calculation with 25% Cr doped in $AgAlS_2$ is shown in **Fig.** 4.11 (a) DOS, (b) up spin and (c) down spin band structures with an energy gap of 2.15 eV at the minority spin channel. Total spin moment is 3 μ_B/cell and Cr site spin moment is 2.41 μ_B/atom. Two fold bands are plotted in the first Brillouin zone (BZ), where some bands are seen doubly, triply, and multiply degenerate at some energy level. The reduced wave vectors (critical points in BZ) are plotted along the independent axis. Γ is the zone center and X, and Z are zonal edges connected by Δ and Y lines. Origin of metallic and insulating states can be understood by sp^3 hybrid states. In **Fig.** 4.11(b), the metallic bands (partially occupied) at Fermi level for up spin state are mainly mixed bands between impurity Cr d and host S p. For down spin state, energy gap is governed by forming a bonding-antibonding states of the four sp^3 hybrid bands.

4.4.2 *Magnetic Properties*

Table 4.4 Total magnetic moment (M_T), local spin moments (SM), total hyperfine fields (H_{hf}^t) at impurity site, magnetic Curie temperatures (T_C) estimated by MFA and the energy difference $\Delta E(x)$ between DSM and FHM state for a series of transition metal doped compounds.

Composition	$M_{T(\mu_B/cell)}$	$SM_{(\mu_B/ion)}$	$H_{hf(KG/ion)}^t$	$\Delta E_{(mRy/cell)}$	$T_C^{MFA}{}_{(K)}$
$Ag(Al_{0.90}Ti_{0.10})S_2$	0.19	0.67 (Ti)	−60 (Ti)	0.663	698
$Ag(Al_{0.90}V_{0.10})S_2$	0.42	1.73 (V)	−146 (V)	0.389	410
$Ag(Al_{0.90}Cr_{0.10})S_2$	0.63	2.74 (Cr)	−221 (Cr)	0.810	853
$Ag(Al_{0.90}Mn_{0.10})S_2$	0.86	3.53 (Mn)	−266 (Mn)	0.945	994
$Ag(Al_{0.90}Fe_{0.10})S_2$	0.95	3.20 (Fe)	−221 (Fe)	−0.113	–
$Ag(Al_{0.90}Co_{0.10})S_2$	0.70	2.20 (Co)	−93 (Co)	−0.379	–
$Ag(Al_{0.90}Ni_{0.10})S_2$	0.44	1.06 (Ni)	−86 (Ni)	−0.713	–

Saturate magnetization M_T is defined as the magnetic moment per unit volume. In MFA each magnetic atom experiences a (magnetic) field proportional to the magnetization. This is often treated as exchange field (molecular field or Weiss field) to line up the magnetic moments parallel to each other below the Curie limit $T < T_C$. Above the

Curie limit, that is at $T > T_C$ the spontaneous magnetization vanishes and spin ordered ferromagnetic phase transited to spin disordered paramagnetic phase. Spin order also be destroyed by thermal agitation at elevated temperatures. Calculated magnetic properties of doped chalcopyrite Ag(AlA)S_2 are listed in **Table** 4.4, where 10% composition of magnetic atom A is substituted randomly at Al site. Apart from the induced moments, the saturate magnetizations are roughly estimated by the local spin moments times concentration and multiplied by the number of substitutional sites. Net moments vary proportional to the concentrations in a doped system. Ti has lowest spin moment and total moment, because its a d^1 configuration and have only one electronic states. Magnetic critical temperatures estimated by MFA are higher than room temperature.

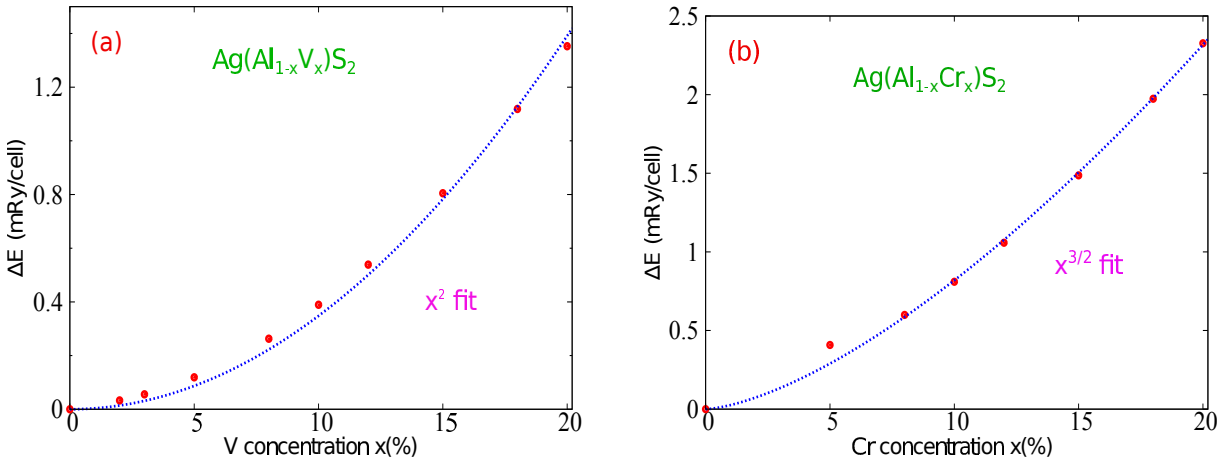

Fig. 4.12 Chemical trends on energy difference $\Delta E(x)$ versus concentrations for (a) V, and (b) Cr doped in $AgAlS_2$.

Total energy difference between FM and DSM states with concentrations of impurity V and Cr is shown in **Fig.** 4.12 (a-b). The solid red spheres are calculated data and the blue dotted curves are fitted to data. In V doped case, the data fitted as parabolic shape and thus T_C would be linear in concentration, indicating a p-d mixing dominate to stabilize the FM state. In Cr doped case, data fitted as third power of square root of concentrations, and therefore T_C would be proportional to square root of concentrations, which indicate a stability of FM state by double-exchange coupling.

4.5 Copper Indium Disulfide $CuInS_2$

4.5.1 *Electronic Structures*

We calculate electronic states at FM and DSM phases, as well as the magnetic properties of the doped systems to realize the underlying mechanisms. The design magnetic materials be stabled energetically and fully spin polarized at the Fermi level. Induced local magnetic properties is seen even at the non-magnetic atom sites.

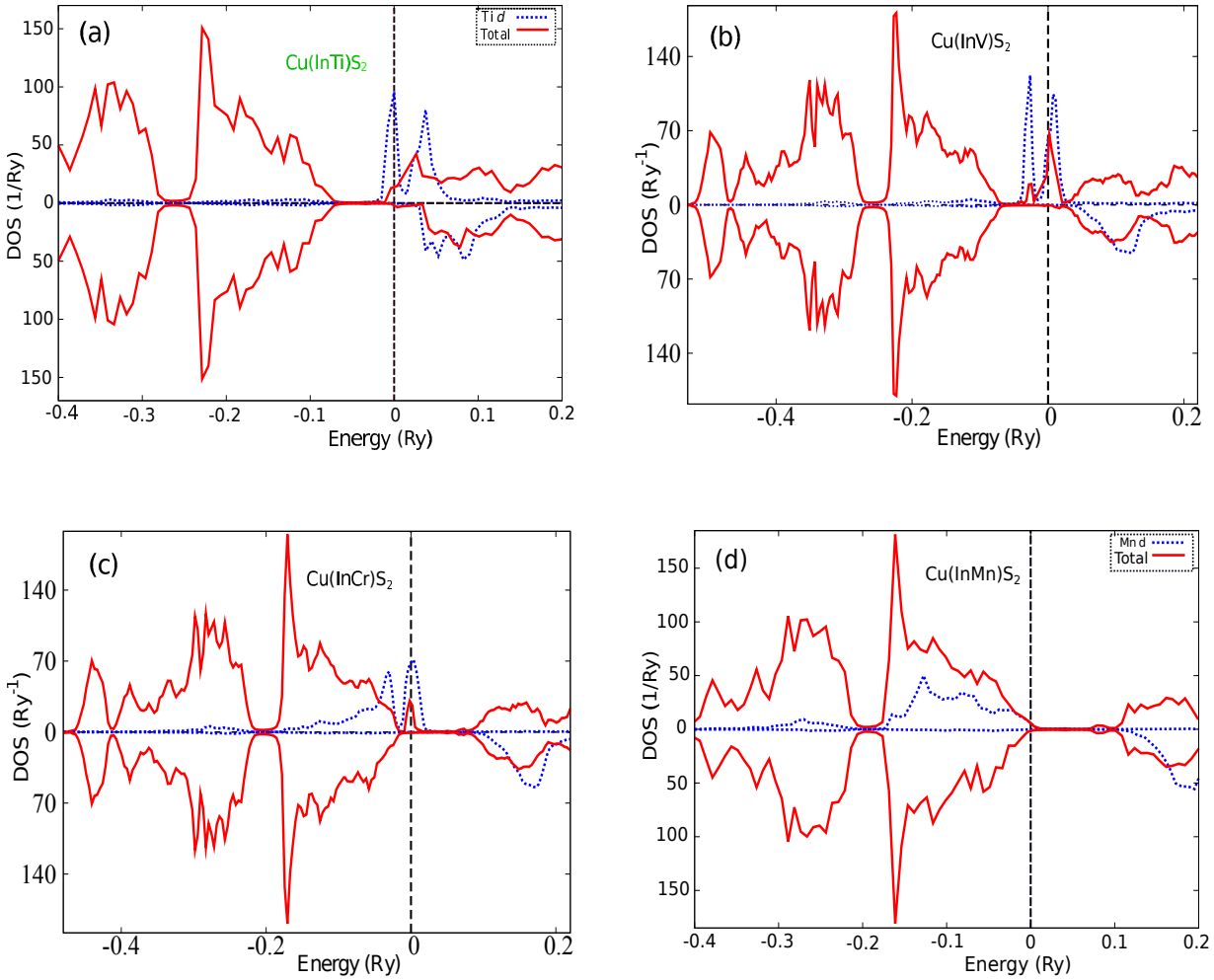

Fig. 4.13 Total density of states (DOS) per cell and local d DOS per atom for doping of (a) Ti, (b) V, (c) Cr, and (d) Mn at host In site, where ferromagnetic states are found as the ground state. Vertical broken lines denote the Fermi level at zero energy.

Ferromagnetic states are stable for Ti, V, Cr, and Mn doped cases, while Fe, Co, and Ni doped alloys are instable ferro-magnetically, as listed in **Table** 4.5. **Figures** 4.13 (a-d)

show the calculated DOS for the systems with a stable FM state. The expected configurations of d electrons of the doped A^{3+} ions in FM states are d^1-d^4, less than a half filled spin states. In these cases either e_g state or t_{2g} state is incomplete and contribute either holes or electrons as d carriers in the system for conduction. Stable FM states may be obtained by the double exchange mechanism [2-6] caused by the d carriers. The FM states realize the half metallicity by forming simultaneously a semiconducting band gap in the minority spin direction and metallic bands in the majority spin direction, mostly evolved from the doping ions.

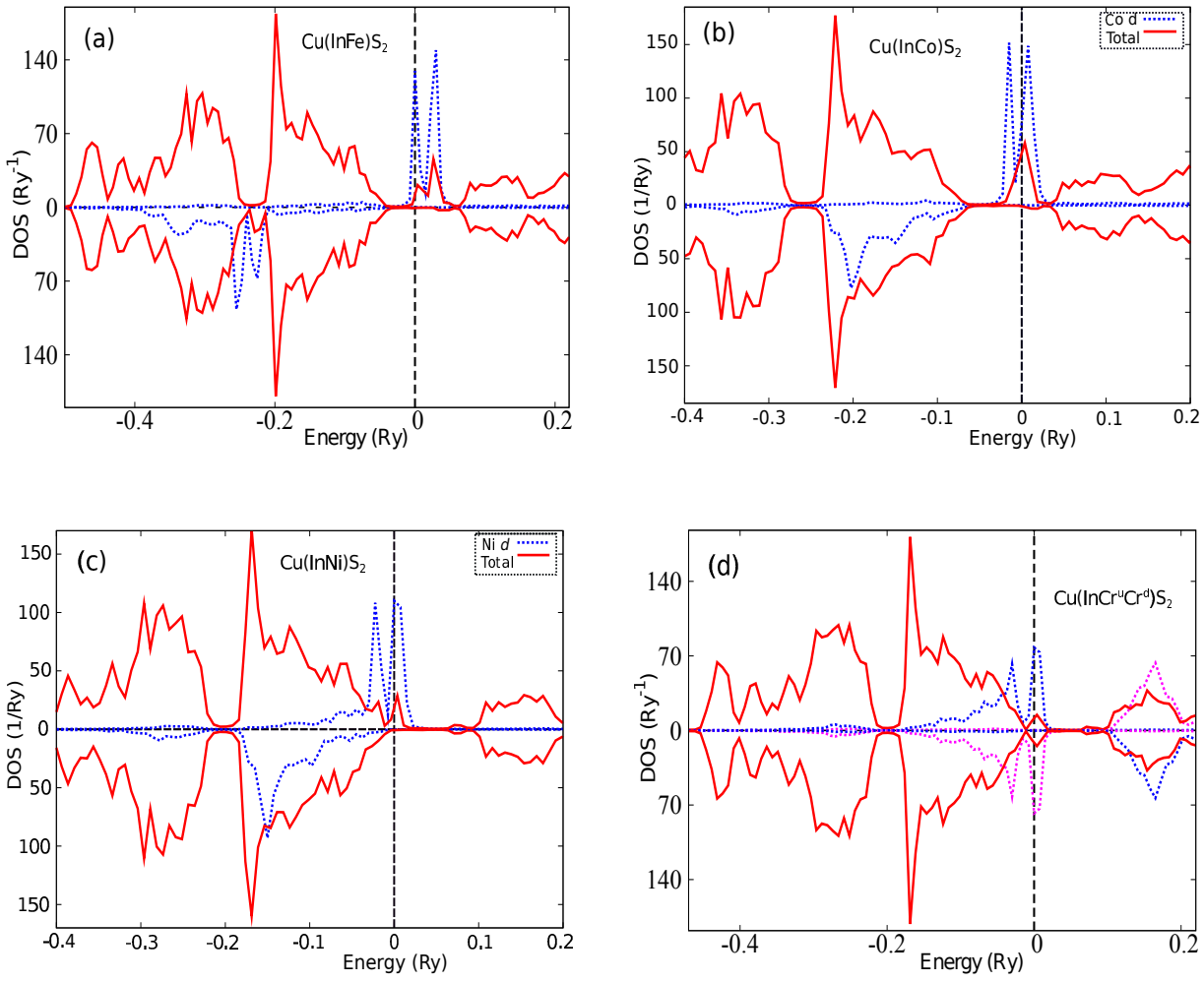

Fig. 4.14 Total density of states (DOS) per cell and local d DOS per atom for doping of (a) Fe, (b) Co, and (c) Ni at host In site, where disordered spin moment (DSM) state is the ground state, and (d) a DSM state with random orientation of spins. Vertical broken lines denote the Fermi level at energy zero.

The electron configurations of the doped Fe, Co, and Ni are d^5, d^6, and d^7, respectively. For a half filled d^5 case (e.g., Fe) there is no mobile carriers for conduction, where super-exchange coupling stabilizes the compound at DSM state, shown in **Fig.** 4.14 (a). Similarly, for d^6 and d^7 cases the $3d$ carriers (here electrons) are mainly $3d\gamma$ orbital and rather localized and less effective for conduction, hence super-exchange prevails to stabilize them at DSM state. In the present study, DSM state is manifested as $Cu(In_{0.95}A^{\uparrow}_{0.025}A^{\downarrow}_{0.025})S_2$ which usually simulates a disordered paramagnetic state as shown in **Fig.** 4.14 (d). At DSM configuration we obtain a nil net magnetization and due to exchange splittings the majority and minority spin states are fully compensated by the local spin moments.

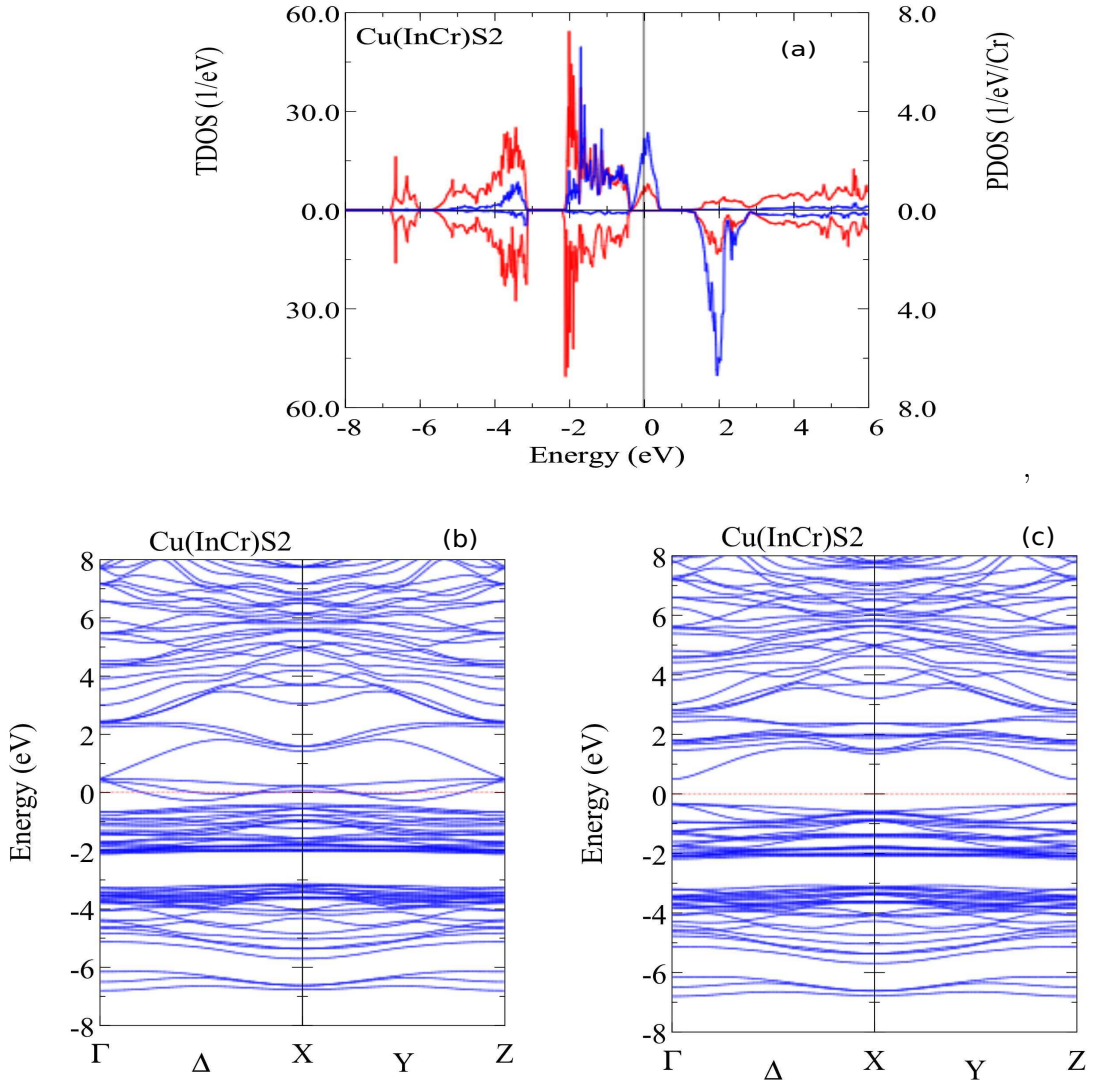

Fig. 4.15 Total density of states (DOS) per cell and local d DOS per atom in a supercell doping of (a) Cr in $CuInS_2$, and band structures (b) majority spin, and (c) minority spin bands.

FLAPW based supercell calculation of band structures and DOS in $Cu(InCr)S_2$ is half metallic with an energy gap of 0.82 eV at the minority spin band, shown in **Fig.** 4.15 (a-c). Cr spin moment inside the muffin-tin sphere is 2.94 μ_B/atom, whereas total spin moment is 3.0 μ_B/cell. We calculate the band structures of TM doped supercell using the same Brillouin zone and symmetric k points of the host chalcopyrite semiconductor. Majority spin band structure is metallic, whereas the minority band structure is insulating, i.e., the full band structure is half metallic.

4.5.2 *Magnetic Properties*

Table 4.5 Total magnetic moments (M_T), local spin moments (SM), total hyperfine fields (H^t_{hf}) at impurity site, magnetic Curie temperatures (T_C) estimated by mean field approximation (MFA) and the total energy difference ($\Delta E(x) = E^{DSM} - E^{FM}$) per cell between disordered spin moment (DSM) and ferromagnetic (FM) state for a series of transition metal doped compounds.

Composition	$M_{T(\mu_B/cell)}$	$SM_{(\mu_B/ion)}$	$H^t_{hf(KG/ion)}$	$\Delta E_{(mRy/cell)}$	$T_C^{MFA}{}_{(K)}$
$Cu(In_{0.95}Ti_{0.05})S_2$	0.09	0.94 (Ti)	−75 (Ti)	0.092	195
$Cu(In_{0.95}V_{0.05})S_2$	0.21	2.20 (V)	−164 (V)	0.795	1390
$Cu(In_{0.95}Cr_{0.05})S_2$	0.36	3.26 (Cr)	−225 (Cr)	0.348	733
$Cu(In_{0.95}Mn_{0.05})S_2$	0.48	4.37 (Mn)	−302 (Mn)	0.163	343
$Cu(In_{0.95}Fe_{0.05})S_2$	0.47	3.81 (Fe)	−238 (Fe)	−1.056	–
$Cu(In_{0.95}Co_{0.05})S_2$	0.38	2.59 (Co)	−185 (Co)	−0.100	–
$Cu(In_{0.95}Ni_{0.05})S_2$	0.23	1.62 (Ni)	−123 (Ni)	−0.082	–

The total energy difference $\Delta E(x) = E^{DSM} - E^{FM}$ per unit cell between DSM and FM states is the central quantity used to estimate Curie temperatures in MFA [7] as $T_C^{MFA}(x) = 2\,\Delta E(x)/(3x\,k_B)$, where x is the impurity concentration and k_B is the Boltzmann constant. The estimated Curie temperatures T_C ($\propto x^{-1}$) are inversely proportional to x, listed in **Table** 4.5, which are above room temperature for V, Cr, and Mn doped compounds. Ti doped system is ferromagnetically stable with T_C lower than room temperature, possibly due to a low carrier of d electron.

Magnetic properties in doped systems arise from the incomplete d orbitals and itinerant character of d electrons. Several magnetic properties such as saturate moments, local spin moments, total HF and magnetic critical temperatures of the doped alloys are listed in **Table** 4.5. The total energy difference between FM and DSM states per unit cell for a particular doping concentration is directly proportional to the critical temperature T_{C} in the framework of MFA [7]. Positive $\Delta E(x)$ is addressed as the ground state of FM state and *vice versa*. Relatively larger net moments, spin moments and HF are seen in Mn and Fe doped compounds. Variation of d electron occupancy is responsible for different local and total properties in the series of TM doped compounds. Total HF of the impurity sites are also tabulated which can be measured by nuclear magnetic resonance (NMR) or Mössbauer spectroscopic experiment [8]. As the Fermi contact term is dominated in the HF of the present systems, the HF are directly proportional to the spin density of s electrons at the nuclear position.

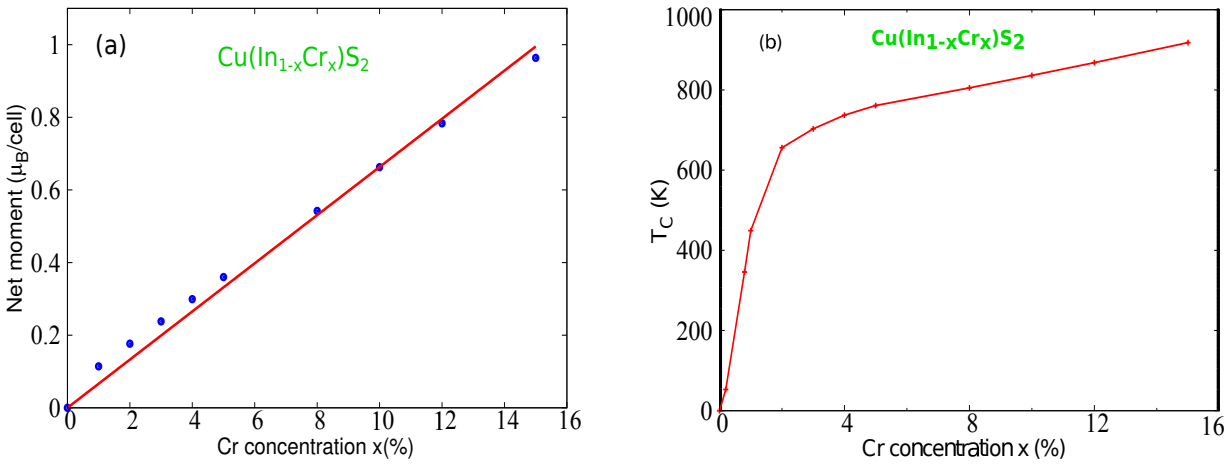

Fig. 4.16 Trends on (a) saturate magnetizations, and (b) magnetic Curie temperatures with doping concentrations.

Chemical trends of total magnetizations and critical temperatures estimated by MFA with variation of concentrations are given in **Fig.** 4.16 (a), and (b), respectively. Net magnetizations per cell give a linear behavior with concentrations, whereas T_{C} increases sharply at very lower dilute limit and then rises monotonically with concentrations.

Table 4.6 Induced local spin moments (LSM) and induced total hyperfine fields ($H_{\rm hf}^{\rm t}$) of $Cu(In_{1-x}A_x)S_2$ with A=V, and Cr at different sites in FM and DSM configuration. Listed typical data clarify the calculation trend.

Composition	Cu site	In site	A site	S site
$Cu(In_{0.95}V_{0.05})S_2$: LSM(μ_B/ion)	−0.00028	0.00186	2.24671	−0.00005
$Cu(In_{0.95}V_{0.05})S_2$: HF(KG/ion)	5.239	27.700	−162.508	1.855
$Cu(In_{0.95}V^{\uparrow}_{0.025}V^{\downarrow}_{0.025})S_2$: LSM($\mu_B$/ion)	0	0	±2.24087	0
$Cu(In_{0.95}V^{\uparrow}_{0.025}V^{\downarrow}_{0.025})S_2$: HF(KG/ion)	0	0	±162.816	0
$Cu(In_{0.95}Cr_{0.05})S_2$: LSM($\mu_B$/ion)	−0.01126	0.00185	3.26275	−0.00836
$Cu(In_{0.95}Cr_{0.05})S_2$: HF(KG/ion)	7.103	22.659	−226.484	−1.890
$Cu(In_{0.95}Cr^{\uparrow}_{0.025}Cr^{\downarrow}_{0.025})S_2$: LSM($\mu_B$/ion)	0	0	±3.25655	0
$Cu(In_{0.95}Cr^{\uparrow}_{0.025}Cr^{\downarrow}_{0.025})S_2$: HF(KG/ion)	0	0	±227.918	0

The induced magnetic properties at all sites of $Cu(In_{0.95}A_{0.05})S_2$ and $Cu(In_{0.95}A^{\uparrow}_{0.025}A^{\downarrow}_{0.025})S_2$ with A = V, and Cr are shown in **Table** 4.6. In FM states induced spin moments at the host Cu, In, and S sites are negligibly smaller than the corresponding quantity at the magnetic impurity site. Similar trend is seen in the case of hyperfine fields (HF), where some significant level of HF is found at the non-magnetic sites. Induced quantities either enhance or diminish the magnetic properties at the impurity site. On the contrary, in DSM configuration the induced spin moments at the host sites are zero and total spin moments for up- and down spin states appear at the magnetic impurity site only. Such a tendency is equally seen for the case of HF (magnetic field), where due to core polarization mechanism of core electrons, that is the spatial variation of s electron wave function contribute to induce HF at the neighboring sites. The polarized distorted waves by the intra-atomic exchange interaction between the core s electrons and the valence d electrons give an asymptotic tails, which produce induced local magnetic properties at the non-magnetic ion sites.

4.6 Hyperfine Fields

4.6.1 Hyperfine Fields in Ferromagnetic States of Cu(AlA)Se_2

Table 4.7 Net moments (M_T), local spin moments (SM) and hyperfine fields (H_{hf}) for a series of V concentrations in $Cu(Al_{1-x}V_x)Se_2$. H^c_{hf} is the core contribution, H^v_{hf} the valence one and H^t_{hf}=H^c_{hf}+H^v_{hf} the total value in kG.

Composition	$M_{T(\mu_B/cell)}$	$SM_{(\mu_B/V)}$	$H^c_{hf(KG/V)}$	$H^v_{hf(KG/V)}$	$H^t_{hf(KG/V)}$
$Cu(Al_{0.98}V_{0.02})Se_2$	0.11	1.884	−215.61	70.01	−145.60
$Cu(Al_{0.97}V_{0.03})Se_2$	0.15	1.872	−214.21	70.04	−144.17
$Cu(Al_{0.95}V_{0.05})Se_2$	0.23	1.859	−212.79	70.41	−142.38
$Cu(Al_{0.92}V_{0.08})Se_2$	0.35	1.850	−211.79	71.18	−140.61
$Cu(Al_{0.90}V_{0.10})Se_2$	0.44	1.847	−211.46	71.74	−139.71
$Cu(Al_{0.88}V_{0.12})Se_2$	0.52	1.845	−211.28	72.32	−138.97
$Cu(Al_{0.85}V_{0.15})Se_2$	0.63	1.844	−211.22	73.18	−138.04

HF is a very local spectral parameter in a magnetic system often investigated with the resonance technique or spectroscopic analyses. For instance, total HF at the impurity sites can be measured by nuclear magnetic resonance (NMR) or Mössbauer spectroscopic experiment [8]. There is no universal scaling between HF and local or dipole moments. Since at a given magnetic site the orbital moment and dipole moment are much smaller than the corresponding spin moment, therefore, to a good approximation, the Fermi contact term is dominated in the HF of the present systems. The contact term originates from a different density of s like electrons with spin-up and spin-down at the nuclear position.

In **Table** 4.7 total moments per cell, local spin moments per ion and the corresponding core, valence and total HF at the impurity sites are given for a systematic variation of V concentrations. Net moments per cell gradually increase with V concentrations, whereas the spin moments very slowly decrease with V concentrations, possibly for larger induced moments on the neighboring host ion sites of the impurity. A decreasing

trend (in magnitude) of the total HF at V site is shown in **Fig.** 4.17 (a) for a series of V concentrations, whereas an almost linear dependence of HF (increases in magnitude) with spin moments at V site in $Cu(Al_{1-x}V_x)Se_2$, shown in **Fig.** 4.17 (b).

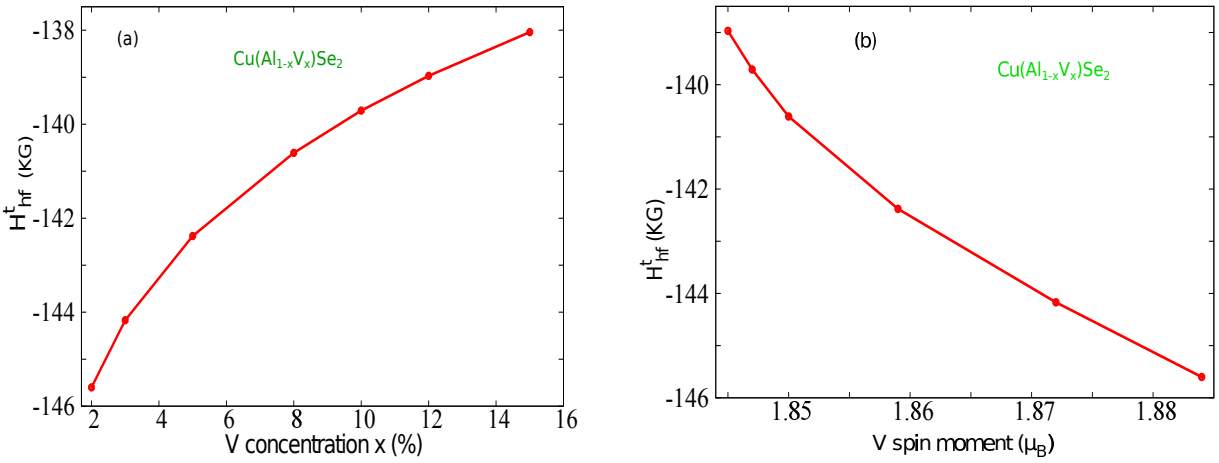

Fig. 4.17 Trends of (a) total hyperfine fields (HF) for a systematic doping of V concentration at host Al^{3+} site, and (b) HF increases (magnitude) with larger spin moment of V.

4.6.2 Hyperfine Fields in Ferromagnetic States of Cu(InA)S_2

Table 4.8 Net moments (M_T), local spin moments (SM) and hyperfine fields (H_{hf}) for doping of Cr impurity in $CuInS_2$. H^c_{hf} is the core contribution, H^v_{hf} the valence one and H^t_{hf}=H^c_{hf}+H^v_{hf} the total value in kG.

Composition	$M_{T(\mu_B/cell)}$	$SM_{(\mu_B/Cr)}$	$H^c_{hf(KG/Cr)}$	$H^v_{hf(KG/Cr)}$	$H^t_{hf(KG/Cr)}$
$Cu(In_{0.99}Cr_{0.01})S_2$	0.12	3.304	−395.48	165.67	−229.81
$Cu(In_{0.98}Cr_{0.02})S_2$	0.18	3.289	−393.67	165.33	−228.35
$Cu(In_{0.97}Cr_{0.03})S_2$	0.25	3.278	−392.47	164.98	−227.49
$Cu(In_{0.96}Cr_{0.04})S_2$	0.31	3.269	−391.44	164.56	−226.88
$Cu(In_{0.95}Cr_{0.05})S_2$	0.37	3.263	−390.58	164.09	−226.48
$Cu(In_{0.94}Cr_{0.06})S_2$	0.43	3.256	−389.79	163.57	−226.22

In **Table** 4.8 total moments per cell, local spin moments per ion and the corresponding core, valence and total HF at the impurity sites are listed for a systematic variation of Cr

concentrations ranging from 1% to 6%. Since energy gain is proportional to composition, therefore net moments per cell gradually increase with Cr concentrations, whereas the spin moments as well as the local and total HF slowly decrease with Cr concentrations for higher induced moments on the nonmagnetic ionic sites. If electronic spins are exchanged (flipped) rapidly due to the exchange interaction or the motion of conduction electrons, NMR level is shifted by the average hyperfine interaction of the electrons, known as NMR Knight shift. According to core polarization mechanism [9], the core and valence HF are opposite in sense for the inversely polarized core and valence s electron wave functions. A decreasing (increasing) trend of the total HF at Cr site with doping concentration (spin moments) is plotted in **Fig.** 4.18 a (b).

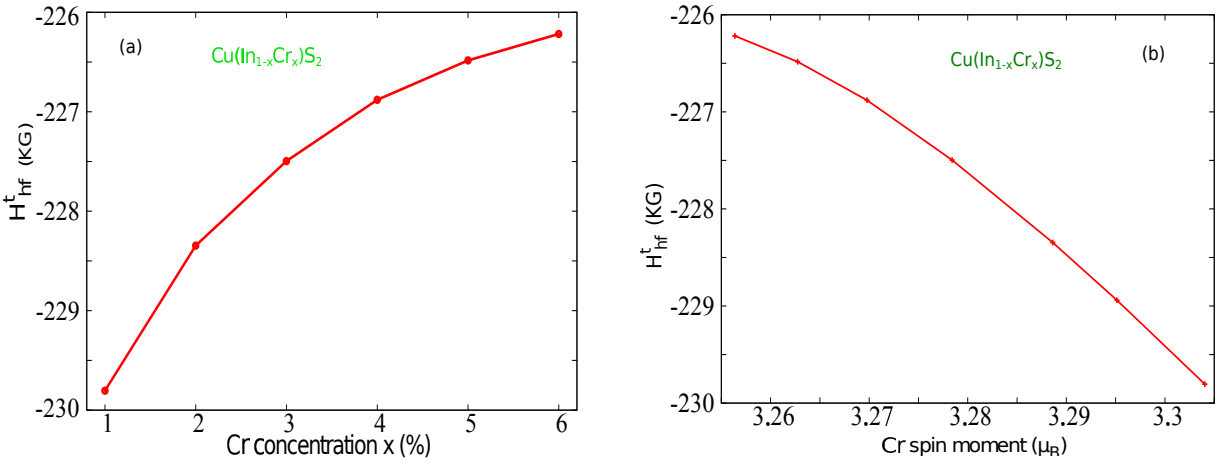

Fig. 4.18 Trends of (a) hyperfine fields with concentration, and (b) local spin moments with hyperfine fields for doping of Cr at host In^{3+} site.

4.7 $4d$, $5d$, and $4f$ Transition Metal Doping

We have investigated further using KKR-CPA by doping $4d$ and $5d$ TM at host ions In and Al site, and we found no significant magnetism arises. That is for $Cu(Al_{0.95}Sc_{0.05})Se_2$, $Cu(In_{0.95}Mo_{0.05})S_2$, $Cu(Al_{0.95}Pd_{0.05})Se_2$, $Cu(Al_{0.95}W_{0.05})Se_2$ total magnetic moment per cell is zero and hence spin moments and hyperfine fields also zero. Thus $4d$ and $5d$ series are less important for producing a new magnetic phase. On the other hand, using FLAPW method by doping $4f$ elements, namely Gd and Sm with 12.5% and 25% concen-

trations, respectively, in a supercell such as $Cu(Al_{0.875}Gd_{0.125})Se_2$ and $Ag(Al_{0.75}Sm_{0.25})Se_2$, we found no sign of ferromagnetism.

Typically, in Gd doped system total magnetization $-7\mu_B$ can be understood as follows. A magnetic atom of total angular momentum J carries a magnetic moment

$$\mu = -g_J \, \mu_B \, \mathbf{J} \tag{4.9}$$

where the *Landé factor* g_J is given by [10]

$$g_J = \frac{3}{2} + \frac{1}{2}\left[\frac{S(S+1) - L(L+1)}{J(J+1)}\right] \tag{4.10}$$

Gd is a rare-earth element with $4f$ electron system. When Gd is doped at Al^{3+} site, the Gd^{3+} ion will thus have a $4f^7$ high spin configuration, *i.e.*, n=7 electrons in the f shell, which is an exactly half-filled shell. According to Hund rules, a half-filled shell gives total orbital angular momentum L=0, total spin S=7/2, therefore total angular momentum J=7/2. Since L=0, the magnetism would be solely due to the spin. Putting above values in the equation (4.10) we get exactly g_J=2, and finally from equation (4.9) the net moment is μ=$-7\mu_B$.

4.8 Discussion on Ferromagnetic States and T_C

Ferromagnetic states are stable in Ti, V, Cr, and Mn doped compounds, which are summarized with T_C and Al-Al (doped site) bond lengths in **Table** 4.9. Beyond the limiting temperatures, magnetic ordering destroyed and FM state becomes a DSM state.

Table 4.9 Estimated Curie temperatures in **K** for each stable ferromagnetic state at 10% concentration of impurities. BL_{Al-Al} is the bond length (BL) of impurity-impurity site.

A element	Ti	V	Cr	Mn	BL_{Al-Al}
$Cu(AlA)Se_2$	267	345	713	710	3.91
$Ag(AlA)Se_2$	523	314	732	832	4.01
$Ag(AlA)S_2$	698	410	853	994	3.83

FM threshold temperatures are higher than room temperature, except in Ti case of few system which exhibit T_C lower than room temperature, possibly due to low carrier of d electrons. In Ti case double-exchange acts in majority e_g state, in V case FM super-exchange works between occupied e_g and empty t_{2g} states of majority spins, and in Cr, and Mn cases again double-exchange acts in majority t_{2g} state (**cf. § 2.8**). In Cr and Mn doped cases Curie limits are almost similar and higher than Ti case, because of more d electrons for coupling. In $Ag(AlA)S_2$ case highest T_C is estimated, where the host compound has relatively larger energy gap than other compounds, and S p states are much deeper than Se p states. In the case of V, there exists solely FSX mechanism controlling T_C in a nearly gapped situation, thus the trend in T_C can be explained by impurity-impurity distance (Al-Al bond length). In the other cases, the trends seem to be a bit complex because additional SX may contribute more or less to the double-exchange coupling. In contrast to above discussion, in Fe, Co, and Ni doped cases ASX dominate and DSM state becomes the ground state, that is their spins are randomly oriented at zero kelvin.

4.9 References

[1] R.A. de Groot, F.M. Mueller, P.G. van Engen and K.H.J. Buschow, Phys. Rev. Lett. **50**, 2024 (1983).

[2] B. Belhadji, L. Bergqvist, R. Zeller, P.H. Dederichs, K. Sato and H. Katayama-Yoshida, J. Phys.: Condens. Matter **19**, 436227 (2007).

[3] P.W. Anderson, Phys. Rev. **79**, 350 (1950).

[4] C. Zener, Phys. Rev. **82**, 403 (1951).

[5] H. Akai, Phys. Rev. Lett. **81**, 3002 (1998).

[6] A.N. Andriotis, S. Lisenkov and M. Menon, J. Phys.: Condens. Matter **23**, 086004 (2011).

[7] L. Bergqvist and P.H. Dederichs, J. Phys.: Condens. Matter **19**, 216220 (2007).

[8] C. Wang, S. Xue, J. Hu, and K. Tang, Jpn. J. Appl. Phys. **48**, 023003 (2009).

[9] S. Blügel, H. Akai, R. Zeller and P.H. Dederichs, Phys. Rev. B **35**, 3271 (1987).

[10] H. Alloul, Introduction to the Physics of Electrons in Solids, Springer (2011).

Chapter 5

Antiferromagnetic Half Metals

Theoretically design antiferromagnets (AF) are rather different from the usual AF, where the net magnetic moment is compensated by spin symmetry between the sublattices of opposite spins or the reversal of a spin-density wave. These effects cause no spin polarization of the conduction electrons. In half metallic AF the vanishing effect of local spin moments (sum to zero net moment) is provided by the requirement of the integral net moments. A suitable TM pair with total valence electron sixteen in group I-III-VI_2 case predicts a zero net moment [1]. As a result, a full spin polarization of the conduction electrons is found at the Fermi level, where the host semiconductors is doped by at least two types of equal concentration of magnetic atoms.

5.1 Codoping of Transition Metal Elements

If we take any pair of TM out of seven (Ti, V, Cr, Mn, Fe, Co, and Ni) and dope at a host cation site, then the number of alloys would be: $C(7,2) = 7!/2!5! = 21$. The prototype form of alloys can be as $Cu(In_{1-2x}A_xB_x)S_2$ or $Cu(In_{1-x-y}A_xB_y)S_2$, where A and B are TM and x, y are their concentrations. Pair concentrations can be equal or unequal. Let the TM pairs be as follows:

AB= TiV, TiCr, TiMn, TiFe, TiCo, TiNi

AB= VCr, VMn, VFe, VCo, VNi

AB= CrMn, CrFe, CrCo, CrNi

AB= MnFe, MnCo, MnNi

AB= FeCo, FeNi

AB= CoNi

Now if any three TMs out of seven are taken at a time as C(7,3) to form new alloys as $Cu(In_{1-x-y-z}A_xB_yC_z)S_2$, the total combination of alloys would be 35. Let the TM triplets be

ABC=TiVCr, TiVMn, TiVFe, TiVCo, TiVNi, TiCrMn, TiCrFe, TiCrCo, TiCrNi, TiMnFe, TiMnCo, TiMnNi, TiFeCo, TiFeNi, TiCoNi

ABC=VCrMn, VCrFe, VCrCo, VCrNi, VMnFe, VMnCo, VMnNi, VFeCo, VFeNi, VCoNi

ABC=CrMnFe, CrMnCo, CrMnNi, CrFeCo, CrFeNi, CrCoNi

ABC=MnFeCo, MnFeNi, MnCoNi

ABC=FeCoNi

If the process is repeated for any four ions at a time, then again the possible alloys would be 35 as $Cu(In_{1-4x}A_xB_xC_xD_x)S_2$, for instance $ABCD$=VCrFeCo, VCrFeNi, VCrCoNi, and so on. Therefore, to handle all possible alloys and to understand the underlying mechanisms are really a cumbersome task, instead in this dissertation, we studied selected of them based on some propositions explained in the mechanism part.

5.2 Mechanism

The stability of antiferromagnetic (AF) or ferromagnetic (FM) state can be depicted by coupling mechanisms between the magnetic ionic states. The mechanism of occurring half metallic AF in general in diluted magnetic semiconductors (DMSs) with $3d$ TM is explained in Ref. [2] and that of double-exchange and super-exchange in DMSs are described in Ref. [3]. We explain the AF stability mechanism in chalcopyrite semiconductor $CuAlSe_2$ codoped by $3d$ TM as follows. Typically we consider two magnetic ions, say Cr and Ni having valence d electrons less and more than half filled, respectively. Although, the number of d electrons vary from system to system, we assume that when Cr and Ni randomly mixed at Al^{3+} site, the available valence d electrons of Cr^{3+} and Ni^{3+} are d^3 and d^7, respectively. The exchange coupling interactions are schematically shown in **Fig.** 5.1.

When two ions (i) and (ii) couple ferromagnetically to form a joint band (iv), electrons can hop between the states of different energies of occupied and empty states reducing their kinetic energies (transfer integral). This is nothing but the super-exchange interaction [2-7]. On the contrary, for AF coupling of those two ions (ii) and (iii) to produce the joint band (v), electrons of one of the spin states (say, up) can hop between the states of the same energy (degenerate states) reducing more kinetic energy. This correspond to the double-exchange interaction [2-6, 8]. In general, double-exchange interaction is stronger than super-exchange interaction and hence AF state is more stable than FM state. The FM coupling produces metallic bands in both spin directions at the Fermi level, while the AF coupling realizes the half metallic band. Obviously, the gain in band energy in AF coupling is higher than FM coupling, which indicates the stability of AF state.

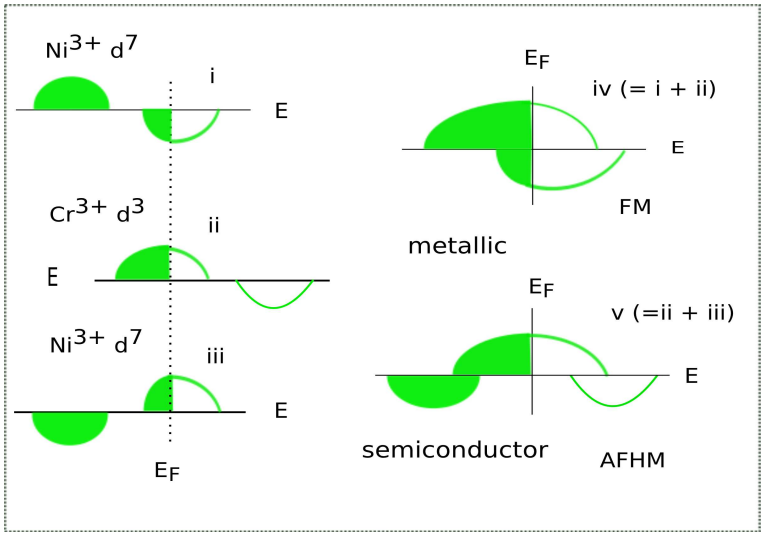

Fig. 5.1 Schematic density of states for ferromagnetic metal (FM), and antiferromagnetic half metal (AFHM), where i, ii, and iii (antiparallel band of i) are $3d$ impurity bands before coupling, and iv (i+ii) and v (ii+iii) are joint bands after coupling.

5.3 Copper Aluminum Diselenide $CuAlSe_2$

5.3.1 *Electronic Structures*

Electronic structures *viz.* local and net density of states for total 6% concentrations of impurity pairs doped at Al site of the host $CuAlSe_2$ are shown in **Fig.** 5.2 (a-d).

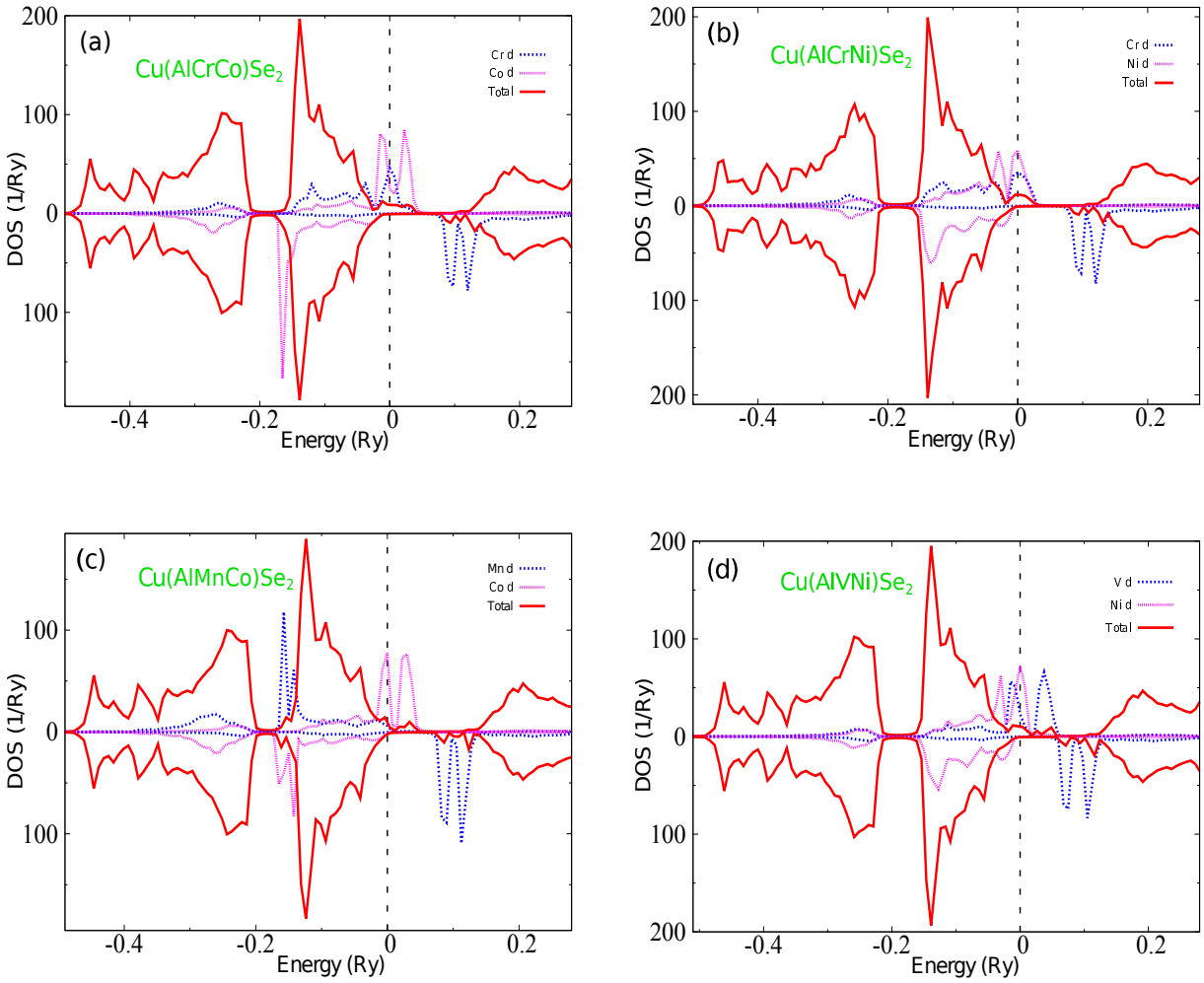

Fig. 5.2 Total density of states (DOS) per cell and local *d* DOS per atom for doping of transition metal pairs (a) Cr-Co, (b) Cr-Ni, (c) Mn-Co, and (d) V-Ni at the host Al site, where ferrimagnetic states are the ground state. The energy zero is taken at the Fermi level.

In **Fig.** 5.2 (a), Co minority e_g state partially overlap with Cr majority t_{2g} state, whereas in **Fig.** 5.2 (b) Ni minority t_{2g} state fully overlap with Cr t_{2g} producing a common total band at the semiconducting gap. In **Fig.** 5.2 (c), Mn majority t_{2g} state is almost

occupied and partially mix with the localized minority e_g state of Co, exhibiting metallicity in up spin state and produce a small DOS with few d holes at the spin down band. In **Fig.** 5.2 (d), majority e_g state of V hybridize with Ni minority t_{2g} state and exhibit half metallicity with an energy gap at the down spin channel.

5.3.2 *Magnetic Properties*

Table 5.1 Succinct of total moments (M_T), spin moments (SM), magnetic transition temperatures and total energy difference $\Delta E(x)$ between disordered spin moment (DSM) state and ferrimagnetic (FiM) state for each compound. Positive $\Delta E(x)$ means that FiM state is the ground state, unless say otherwise.

Composition	$M_T(\mu_B$/cell)	SM(μ_B/atom)	ΔE(mRy/cell)	$T_C(K)$
$Cu(Al_{0.94}Cr_{0.03}Fe_{0.03})Se_2$	0.06	−3.07 (Cr), 3.15 (Fe)	−0.137	–
$Cu(Al_{0.94}Cr_{0.03}Co_{0.03})Se_2$	0.005	2.98 (Cr), −2.07(Co)	0.064	112
$Cu(Al_{0.94}Cr_{0.03}Ni_{0.03})Se_2$	0.07	2.95 (Cr), −0.97 (Ni)	0.048	85
$Cu(Al_{0.94}Mn_{0.03}Co_{0.03})Se_2$	0.089	3.83(Mn), −2.12(Co)	0.159	279
$Cu(Al_{0.94}V_{0.03}Fe_{0.03})Se_2$	0.13	−1.83 (V), 3.10 (Fe)	−0.040	–
$Cu(Al_{0.94}V_{0.03}Co_{0.03})Se_2$	0.06	−1.79 (V), 2.04 (Co)	0.008	13
$Cu(Al_{0.94}V_{0.03}Ni_{0.03})Se_2$	0.006	1.73 (V), −0.95 (Ni)	0.078	136
$Cu(Al_{0.94}Ti_{0.03}Co_{0.03})Se_2$	0.14	−0.22 (Ti), 1.99 (Co)	0.005	8
$Cu(Al_{0.94}Ti_{0.03}Ni_{0.03})Se_2$	0.08	−0.17 (Ti), 0.72 (Ni)	−0.174	–

Calculated magnetic properties by codoping TM pairs at Al^{3+} site of $CuAlSe_2$ are shown in **Table** 5.1. We used 3% composition of each impurity atom and a total 6% mixture of foreign atoms are considered. Net moments are nearly null in Cr-Co, and V-Ni pairs and rather small in Cr-Ni, Mn-Co, and V-Co cases. Rather large net moment is found at Ti-Co pair doped case, which may be for less cancellation of local spin moments. In the present system Cr-Fe, V-Fe, and Ti-Ni are instable ferrimagnetically. Magnetic transition temperatures are lower than room temperature, except Mn-Co case, where critical temperature close to room temperature is found. Local spin moments of

the magnetic atoms are anti-parallel and give a net moments. The failure of Co (Ni) impurities in Cr-Co (V-Ni) pair to support a large spin moment of Cr (V) 2.98 μ_B (1.73 μ_B), might cause a very small net moment. Therefore, a GGA + U treatment with a suitable U value at Co and Ni d orbital would nullify the net moments and results in an AFHM.

AFHM with null net moment has advantages in applications where (i) zero spontaneous magnetization, namely vanishing effect of external field is required, and (ii) particularly to obtain spin-resolved information on a nano scale in SPSTM (spin-polarized scanning tunneling microscopy) as a tip (data reading) material [1].

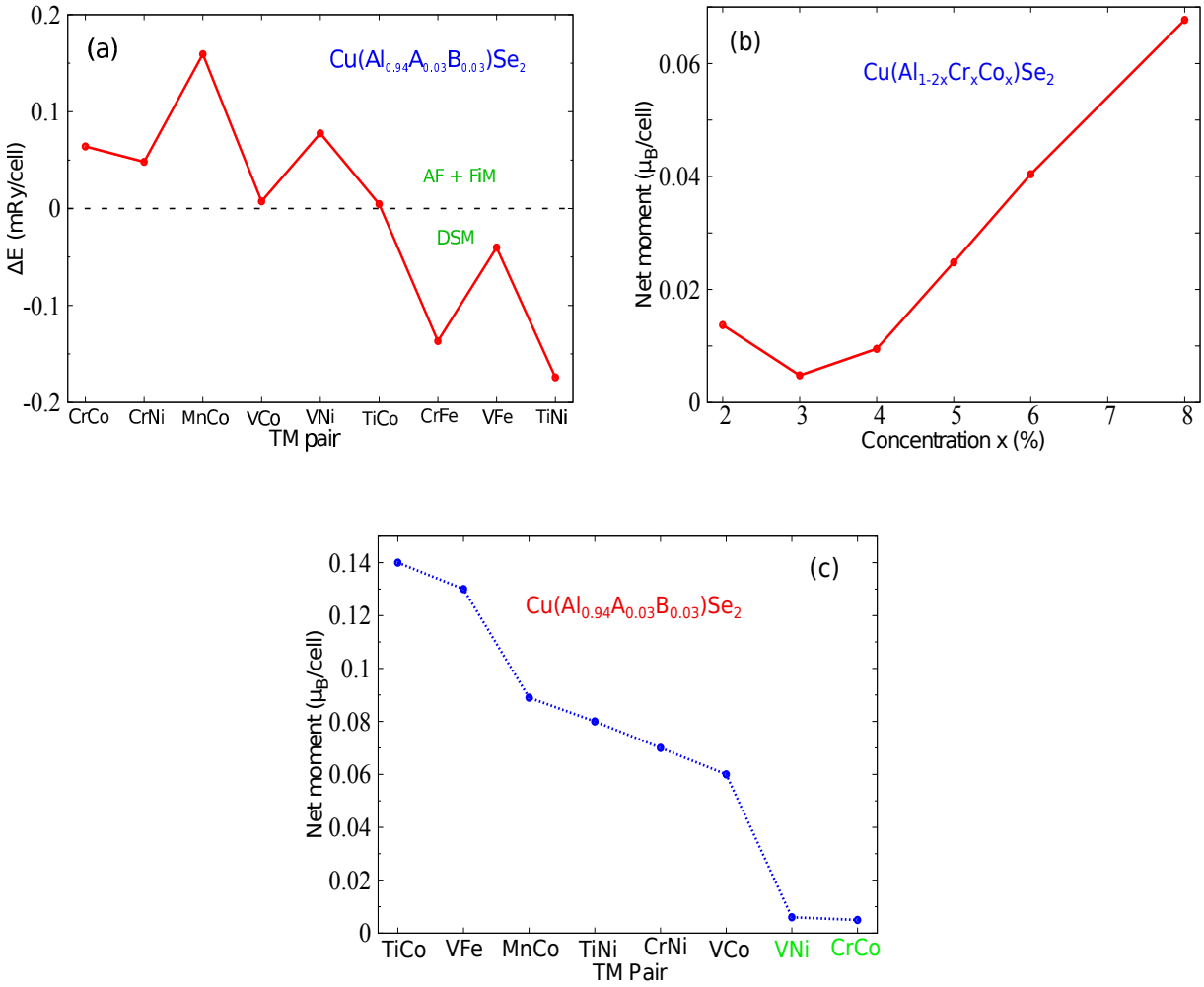

Fig. 5.3 Magnetic behaviors (a) stability trend of ferrimagnetic states, (b) saturate moments profile with concentrations, and (c) favorable TM pair with null moments in codoping cases.

In **Fig.** 5.3 (a), positive energy difference $\Delta E(x)$ denotes the stability of either FiM or AF state, otherwise spin disordered state becomes lower in total energy. Lowest net moment per cell is found at 3% concentration as given in **Fig.** 5.3 (b). Net moments are supposed to be linear with concentrations in a codoped system, but a rising moment below 3% might be due to some percolation effect at a low concentration of dilute limit. In Cr-Co and V-Ni pair cases (**cf. Table 5.1**), the negligibly small net moments can be realized as (i) two TM produce almost similar antiparallel spin moments, (ii) resultant spin moments are further canceled by induced spin moments at the neighboring non-magnetic ion sites. Otherwise, induced moments enhance the resultant spin moments and give rise to a large net moments. Therefore, in terms of net moments Cr-Co and V-Ni pairs can be candidates to design AFHM.

A typical example of magnetic interaction energy is given below. Suppose we have a doped system with two magnetic atoms as $Cu(Al_{0.94}V_{0.03}Ni_{0.03})Se_2$. FM total energy is calculated for parallel spin moments and AF total energy for antiparallel spin moments of the magnetic atoms V and Ni. The difference gives an effective interaction energy of $\Delta E(x) = E_{\rm FM} - E_{\rm AF} = 0.3276$ mRy/cell. This interaction energy maps the stable spin orientation in two different DMS. Between them, the state lower in energy relative to disordered paramagnetic state (a reference state) is taken to calculate Curie temperature in MFA. The governing double-exchange coupling holds the AF state in minimum energy level and that of the FM state at some excited (higher) energy level.

5.4 Silver Aluminum Diselenide $AgAlSe_2$

5.4.1 *Electronic Structures*

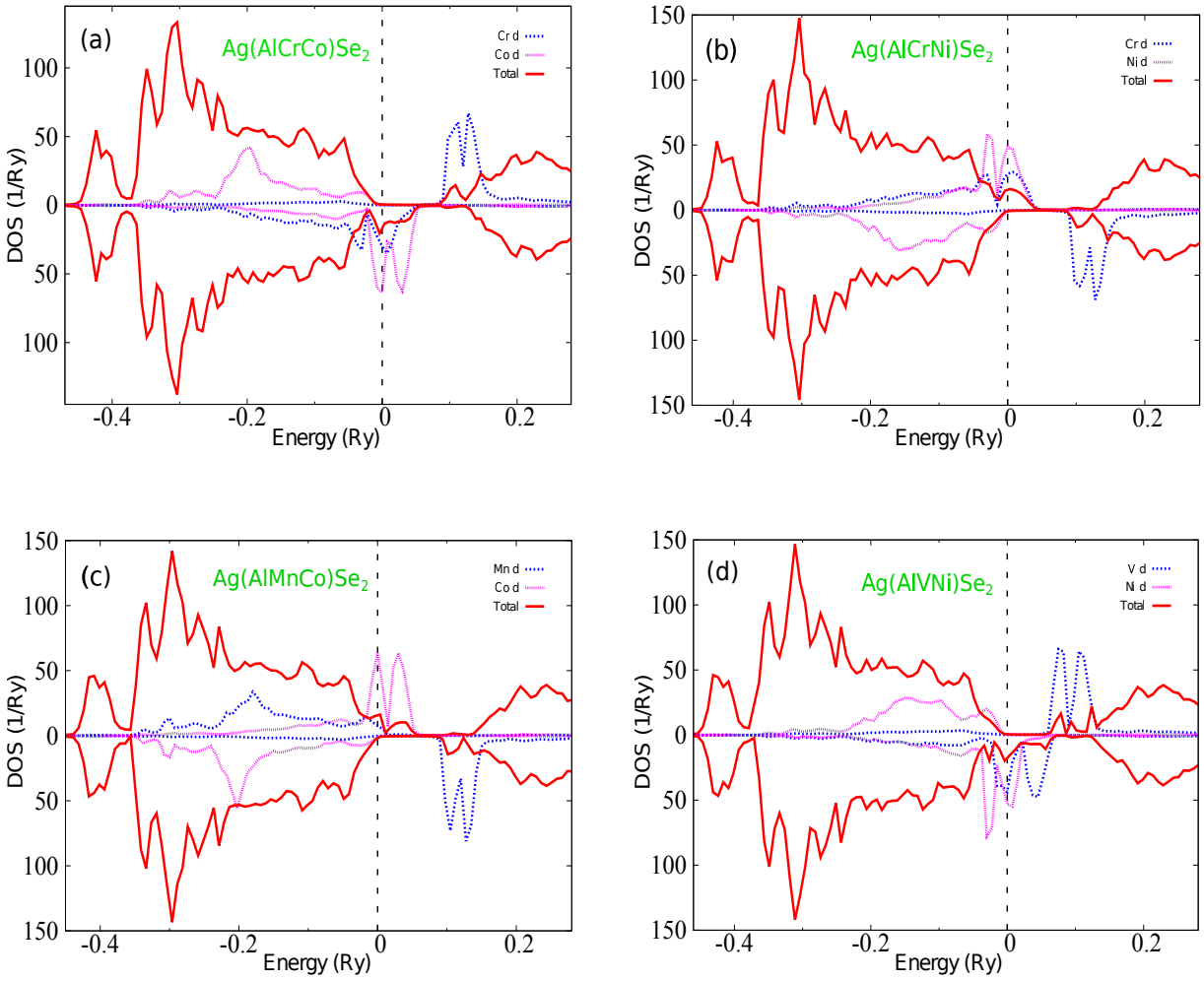

Fig. 5.4 Total density of states (DOS) per cell and local *d* DOS per atom for doping of transition metal pair with total 10% concentration of (a) Cr-Co, (b) Cr-Ni, (c) Mn-Co, and (d) V-Ni at the host Al site, where ferrimagnetic states are the ground state. Vertical broken lines denote the Fermi level.

Electronic structures of silver based and TM pair at 5% concentration of each TM doped at Al site in $AgAlSe_2$ are shown in **Fig.** 5.4(a-d). Density of states are a lucid evidence of half metallicity at the FiM ground state. Local *d* DOS are shown in amplified form to clarify the ligand field splitting. In actual situation, total DOS dominate over all the partial DOS. By integrating DOS up to the Fermi energy electron density can

be obtained, which is nothing but the area covered by the DOS curves. Due to crystal field effect, impurity d orbitals split into e_g and t_{2g} states both in majority and minority spin channels. The spins are resolved by exchange splittings as shown in the DOS curves, have variations in splitting energy which is minimum at V-Ni pair case compare to other depicted compounds.

5.4.2 *Magnetic Properties*

Table 5.2 Summary of total moments (M_T), spin moments (SM), magnetic transition temperatures, and total energy difference $\Delta E(x)$ between disordered spin moment (DSM) state and ferrimagnetic (FiM) state for each compounds. Positive $\Delta E(x)$ means that FiM state is the ground state, unless say otherway.

Composition	$M_T(\mu_B/\text{cell})$	SM(μ_B/atom)	ΔE(mRy/cell)	T_C(K)
$Ag(Al_{0.90}Cr_{0.05}Fe_{0.05})Se_2$	0.15	−3.03 (Cr), 3.36 (Fe)	0.067	70
$Ag(Al_{0.90}Cr_{0.05}Co_{0.05})Se_2$	0.04	−2.94 (Cr), 2.28(Co)	0.189	199
$Ag(Al_{0.90}Cr_{0.05}Ni_{0.05})Se_2$	0.06	2.92 (Cr), −1.19 (Ni)	0.060	63
$Ag(Al_{0.90}Mn_{0.05}Fe_{0.05})Se_2$	0.03	−3.92 (Mn), 3.40 (Fe)	0.098	103
$Ag(Al_{0.90}Mn_{0.05}Co_{0.05})Se_2$	0.07	3.90 (Mn), −2.32 (Co)	0.208	219
$Ag(Al_{0.90}Mn_{0.05}Ni_{0.05})Se_2$	0.20	3.88 (Mn), −1.20 (Co)	0.098	104
$Ag(Al_{0.90}V_{0.05}Fe_{0.05})Se_2$	0.26	−1.85 (V), 3.32 (Fe)	−0.122	–
$Ag(Al_{0.90}V_{0.05}Co_{0.05})Se_2$	0.15	−1.65 (V), 2.26 (Co)	0.267	281
$Ag(Al_{0.90}V_{0.05}Ni_{0.05})Se_2$	0.04	−1.62 (V), 1.17 (Ni)	0.280	295

In silver based host material $AgAlSe_2$, we dope a total of 10% impurity atoms at Al^{3+} site. Minimum (maximum) total moments are found at Mn-Fe (V-Fe) pair case, as listed in **Table** 5.2. A better compensation of net magnetizations may be obtained at some lower dilute limit. In positive $\Delta E(x)$ cases FiM state is the ground state. In contrast, V-Fe doped compound exhibit DSM state as the ground state by super-exchange coupling. Magnetic transition temperatures estimated by MFA are closure to room temperature in

V-Co and V-Ni doped compounds, otherwise T_C is lower than room temperature, might be for lower coupling energy of TM pair d electrons.

5.5 Silver Aluminum Disulfide $AgAlS_2$

5.5.1 *Electronic Structures*

Electronic structures for codoping of total 10% TM pair at $AgAlS_2$ are shown in **Fig.** 5.5 (a-d), where the vertical dashed lines at zero energy denote the Fermi level.

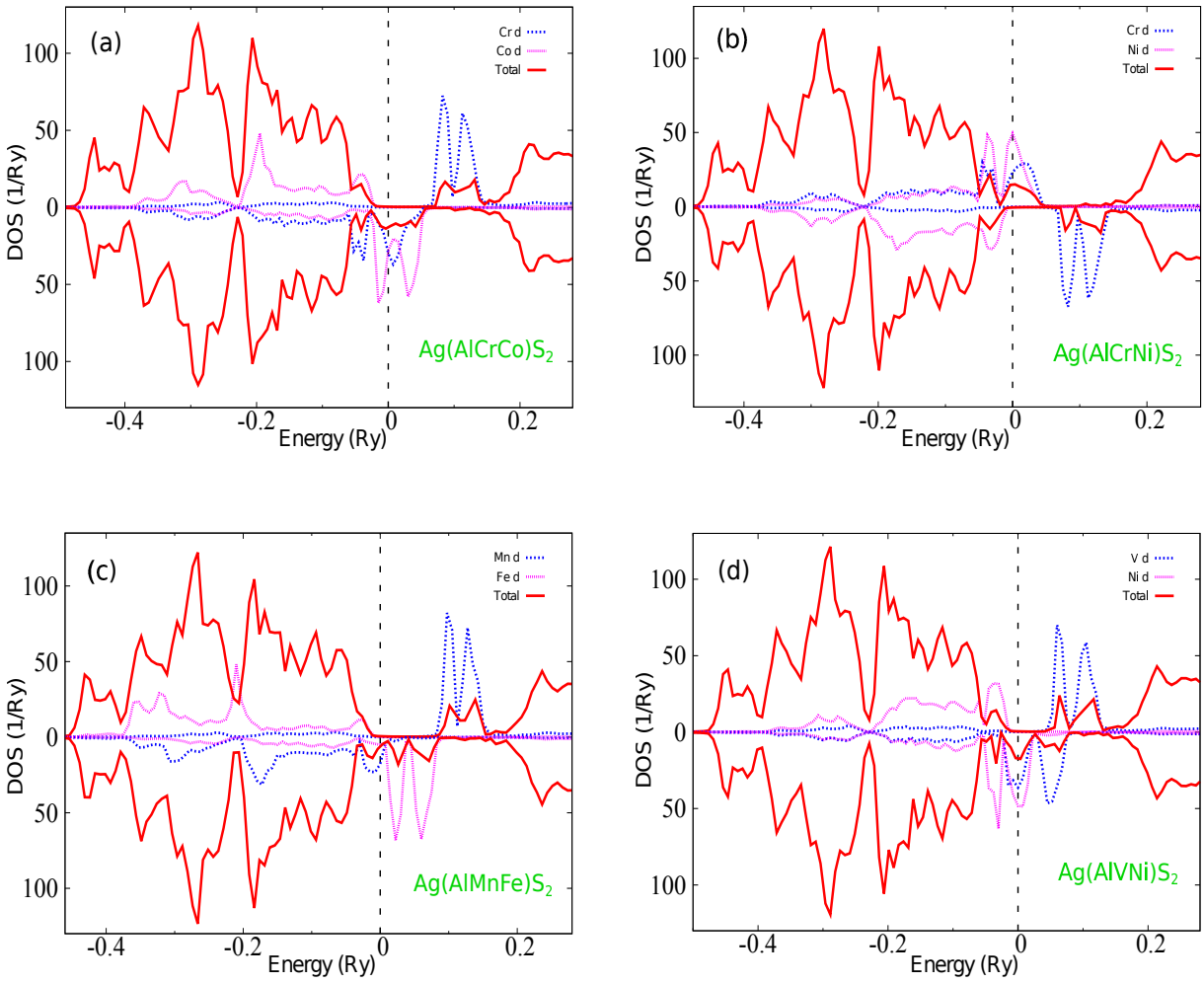

Fig. 5.5 Total density of states (DOS) per cell and local d DOS per atom for doping of transition metal pairs (a) Cr-Co, (b) Cr-Ni, (c) Mn-Fe, and (d) V-Ni at the host Al site, where ferrimagnetic states are the ground state. The energy zero is taken at the Fermi level.

The vertical axes denote the level of DOS. The high density region below the Fermi level are mainly host Ag d states, and shallow density parts arises from s and p states or any mixed states. In terms of spin configuration, each electronic state (microscopic) can accommodate two electrons with opposite spins. In spin polarized case, the splitting of up- and down spin DOS is known as the *exchange splitting*. DOS is obtained by integrating over the energy bands and integrating DOS up to Fermi energy gives the total number of occupied electrons. DOS curves scale as square root of eigenenergy. At the Fermi level no electronic states are seen for minority spin bands, whereas for majority spin bands an overlapping d states appeared in the energy gap region. Therefore, the calculated systems in **Fig.** 5.5 (a-d) are ferrimagnetic half metals.

5.5.2 *Magnetic Properties*

Table 5.3 Sum-up of total moments (M_{T}), spin moments (SM), magnetic transition temperatures and total energy difference $\Delta E(x)$ between disordered spin moment (DSM) state and ferrimagnetic (FiM) state for each compound. Positive $\Delta E(x)$ means that FiM state is the ground state, unless state otherwise.

Composition	$M_T(\mu_{\mathrm{B}}/\mathrm{cell})$	SM(μ_{B}/atom)	ΔE(mRy/cell)	T_{C}(K)
$Ag(Al_{0.90}Cr_{0.05}Co_{0.05})S_2$	0.05	−2.53 (Cr), 2.11 (Co)	0.187	197
$Ag(Al_{0.90}Cr_{0.05}Ni_{0.05})S_2$	0.06	2.47 (Cr), −1.08 (Ni)	0.221	233
$Ag(Al_{0.90}Mn_{0.03}Fe_{0.05})S_2$	0.03	−3.56 (Mn), 3.24 (Fe)	0.394	415
$Ag(Al_{0.90}Mn_{0.05}Ni_{0.05})S_2$	0.18	3.46 (Mn),−1.17 (Ni)	0.3935	414
$Ag(Al_{0.90}V_{0.05}Co_{0.05})S_2$	0.15	−1.34 (V), 2.09 (Co)	0.381	401
$Ag(Al_{0.90}V_{0.05}Ni_{0.05})S_2$	0.05	−1.27 (V), 1.03 (Ni)	0.420	442

In silver based host $AgAlS_2$, we dope again a total 10% of two magnetic atoms at Al^{3+} site. By definition, positive energy difference denote a lower total energy of ferrimagnetic state relative to a DSM state. The average local spins are antiparallel at the FiM state and produce a partially compensated net moment, shown in **Table** 5.3. The compounds with Cr-Co, Cr-Ni, Mn-Fe, and V-Ni codoping can be candidate of AF half metals at some

dilute limit. Among them Mn-Fe, and V-Ni codoped materials exhibit magnetic critical temperatures higher than room temperature. In Mn-Fe case, Fe^{3+} is a half filled electron configuration and supposed to give a local spin moment of $5\,\mu_B$, but due to hybridization a small minority e_g state of Fe d orbital mix with majority t_{2g} state of Mn d orbital around the Fermi level. As a result, Fe gives a reduced spin moment of 3.24 μ_B.

5.6 Copper Indium Disulfide $CuInS_2$

5.6.1 *Electronic Structures*

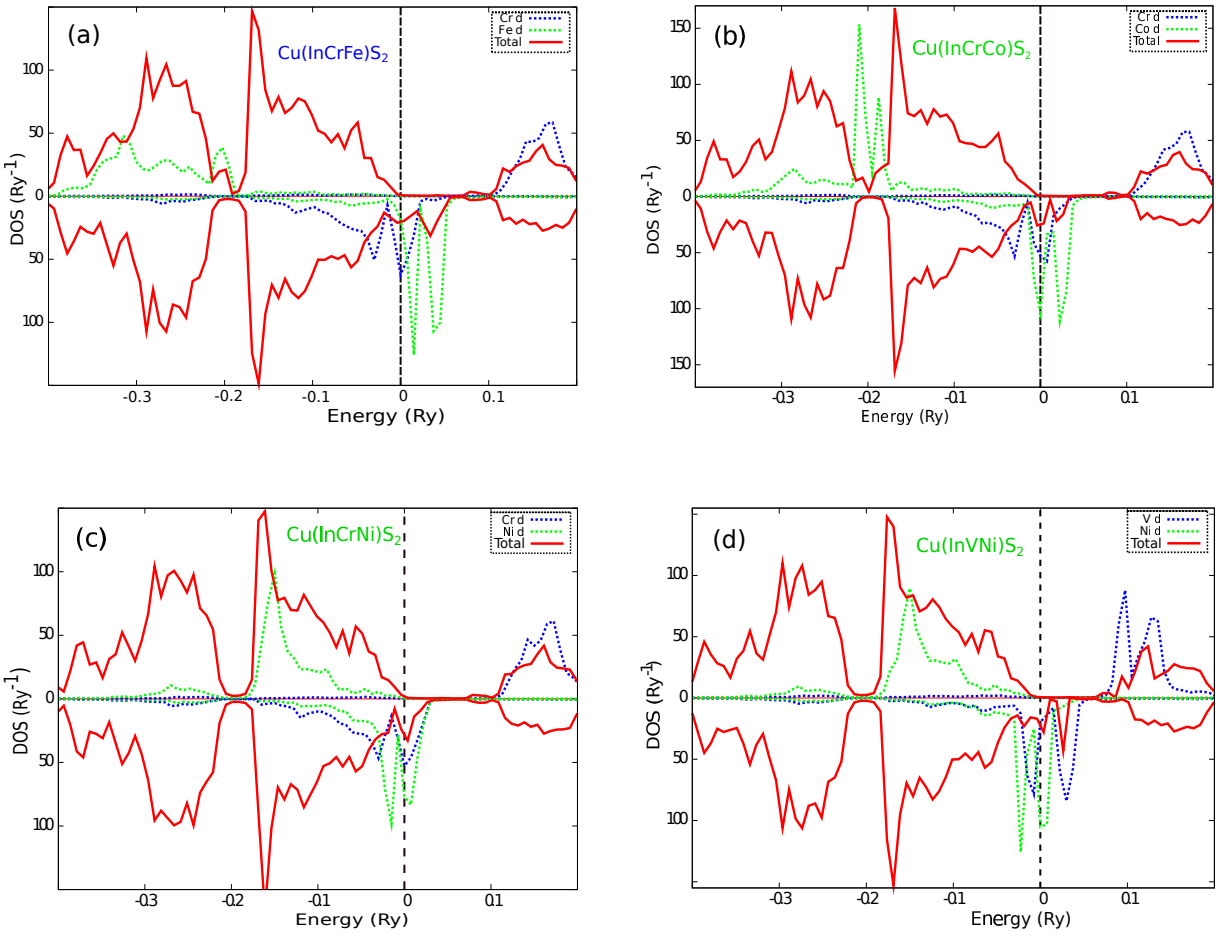

Fig. 5.6 Calculated density of states (DOS) of $Cu(In_{0.9}X_{0.05}Y_{0.05})S_2$ for codoping of (a) Cr-Fe, (b) Cr-Co, (c) Cr-Ni, and (d) V-Ni pair, where ferrimagnetic state is the ground state. The lower (upper) panel indicate the majority (minority) spin states. Local d DOS of impurity sites (blue and green curves) per atom are plotted with total DOS (red curve) per unit cell.

To realize AF and FiM half metallicity, we introduce two types of magnetic ions at In site of $CuInS_2$ at 5% concentration of each impurity ion. Electronic structures of these chemically disordered compounds are calculated for the following cases and compared their total energies to find a stable magnetic state (i) two types of magnetic ions couple ferromagnetically (FM state), (ii) those couple antiferromagnetically (AF state), and (iii) those couple such that the local magnetic moments are arranged randomly, refer to as DSM state.

Figures 5.6 (a-d) show the electronic structures of Cr-Fe, Cr-Co, Cr-Ni, and V-Ni pair doped compounds, where the ferrimagnetic state is the ground state. Electronic total density of states (DOS) per unit cell with the partial d DOS of each impurity ions are plotted. Ferrimagnetic states are taken as $Cu(In_{0.90}X^{\uparrow}{}_{0.05}Y^{\downarrow}{}_{0.05})S_2$, where we assume that X and Y atoms have X^{3+} and Y^{3+} charge states in substituting at In site of the host compound. Electronic structures of the disordered compounds realize the half metallicity by forming simultaneously a semiconducting energy gap and metallic bands, mostly arisen from the magnetic ions, around the Fermi level for up and down spin directions, respectively. The DOS of those cases exhibit a small d holes at the Fermi level, which makes the double-exchange interaction stronger than super-exchange and hence stabilizes the ferrimagnetic states. Those stable ferrimagnetic half metallic states exhibit a full compensation of net magnetization, we hereafter call them as AFHM. Therefore, from **Table** 5.4 we see that Cr-Co, Cr-Ni, and V-Ni pair doped compounds produce nearly zero net moment and are referred to as probable AFHM. **Figure** 5.7 (a) shows the ferromagnetic metallic state of V-Ni pair doped compound, where the impurity spins are taken as $Cu(In_{0.90}X^{\uparrow}{}_{0.05}Y^{\uparrow}{}_{0.05})S_2$. The local spin moments are parallel and aligned to the net moment. The corresponding DSM state of that compound is also shown in **Fig.** 5.7 (b), which results saturation magnetization exactly zero by turning the local spin moments equal and opposite. In the present calculation, DSM state is manifested as $Cu(In_{0.90}X^{\uparrow}{}_{0.025}X^{\downarrow}{}_{0.025}Y^{\uparrow}{}_{0.025}Y^{\downarrow}{}_{0.025})S_2$, which usually simulates a disordered paramagnetic state.

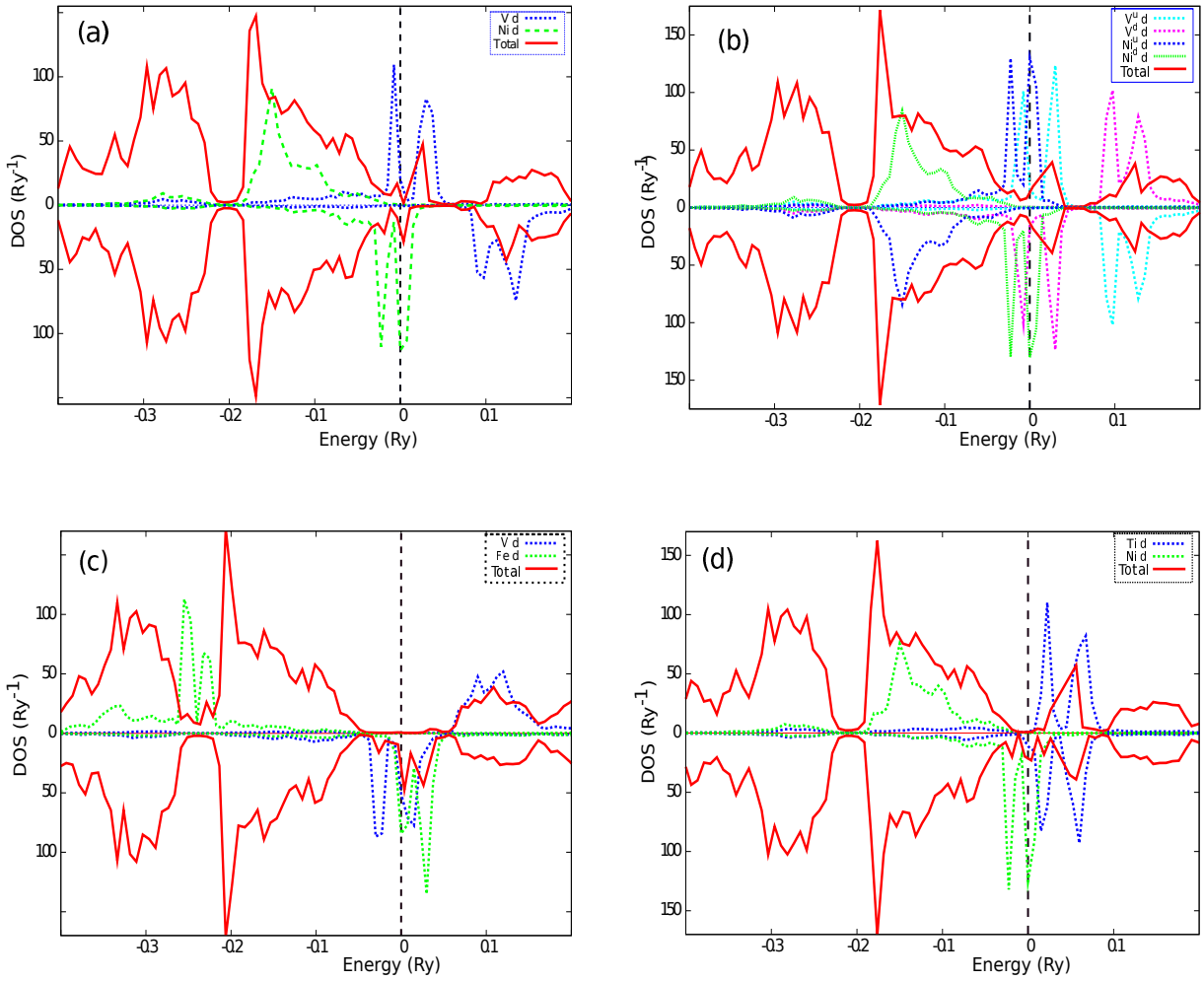

Fig. 5.7 (a) Calculated density of states (DOS) for ferromagnetic metallic state of $Cu(In_{0.9}V_{0.05}Ni_{0.05})S_2$ with total DOS per cell (red curve) and local d DOS per atom of each impurity site (blue and green curves), (b) the DOS of disordered spin moment (DSM) state for codoping of V-Ni pair, all spin moments are aligned randomly (c) DOS of V-Fe pair doped compound where the lower total energy of DSM state is obtained and (d) DOS of Ti-Ni pair doped half metallic ferrimagnetic state. The lower (upper) panel indicate the majority (minority) spin states. Vertical broken lines denote the Fermi enegy.

5.6.2 *Magnetic Properties*

The total energy difference $\Delta E(x) = E^{\mathrm{DSM}} - E^{\mathrm{FiM}}$ per unit cell between the DSM and FiM states are shown in **Table** 5.4, where positive $\Delta E(x)$ indicates the ground state of FiM state and negative $\Delta E(x)$ means the lower total energy of DSM state. The magnetic

transition temperatures are estimated from mean field approximation (MFA) as dividing the total energy difference $\Delta E(x)$ by the total concentration of the magnetic ions and Boltzmann constant and multiplied by 2/3 [9] as follows

$$T_{\mathrm{C}}^{\mathrm{MFA}}(x) = \frac{2}{3}\frac{E^{\mathrm{DSM}} - E^{\mathrm{FiM}}}{2xk_{\mathrm{B}}} \tag{5.1}$$

The estimated Curie temperatures T_{C} in the framework of MFA are also given in **Table** 5.4, which are higher than room temperature, except the V-Ni pair case.

Table 5.4 Succinct of total moments (M_{T}), spin moments (SM), magnetic transition temperatures and total energy difference $\Delta E(x)$ between disordered spin moment (DSM) state and ferrimagnetic (FiM) state for each compound. Positive $\Delta E(x)$ means that FiM states are the ground state, unless noted other-way.

Composition	$M_{\mathrm{T}}(\mu_{\mathrm{B}}/\mathrm{cell})$	SM(μ_{B}/atom)	ΔE(mRy/cell)	T_{C}(K)
$Cu(In_{0.90}Cr_{0.05}Fe_{0.05})S_2$	0.13	−3.24(Cr), 3.92(Fe)	0.289	304
$Cu(In_{0.90}Cr_{0.05}Co_{0.05})S_2$	0.03	−3.24(Cr), 2.78(Co)	0.366	385
$Cu(In_{0.90}Cr_{0.05}Ni_{0.05})S_2$	0.07	3.23(Cr), −1.65(Ni)	0.381	401
$^{\star}Cu(In_{0.90}V_{0.05}Fe_{0.05})S_2$	0.28	−2.14(V), 3.77(Fe)	−0.311	–
$^{\star}Cu(In_{0.90}V_{0.05}Co_{0.05})S_2$	0.17	−2.12(V), 2.63(Co)	−0.934	–
$Cu(In_{0.90}V_{0.05}Ni_{0.05})S_2$	0.04	−1.97(V), 1.61(Ni)	0.221	233
$^{\star}Cu(In_{0.90}Ti_{0.05}Fe_{0.05})S_2$	0.39	−0.86(Ti), 3.74(Fe)	−0.366	–
$^{\star}Cu(In_{0.90}Ti_{0.05}Co_{0.05})S_2$	0.27	−0.68(Ti), 2.63(Co)	−0.748	–
$Cu(In_{0.90}Ti_{0.05}Ni_{0.05})S_2$	0.15	−0.13(Ti), 1.58(Ni)	0.350	369

Magnetic properties such as net magnetizations, and local spin moments of the disordered compounds are listed in **Table** 5.4. Most compensated magnetizations are found in Cr-Co, Cr-Ni, and V-Ni codoped compounds, which are possible target materials for AFHM and a rather small net magnetizations are found in Cr-Fe, and Ti-Ni cases, which are referred to as ferrimagnetic half metals. Although, net magnetizations are virtually compensated, they hold the local magnetic moments of each magnetic ion to a

large value and antiparallel. On the contrary, a bit larger net magnetizations are found for codoped V-Fe, V-Co, Ti-Fe, and Ti-Co. In the 'star ($\star$) mark' compounds, the DSM states show lower total energy. DOS of those compounds reveal that neither d electrons nor d holes are exist, which makes the super-exchange interaction stronger and stabilizes the DSM state, an example is shown in **Fig.** 5.7 (c). Yet some scope remains to seek a stable magnetic phase on those compounds using other types of codopants.

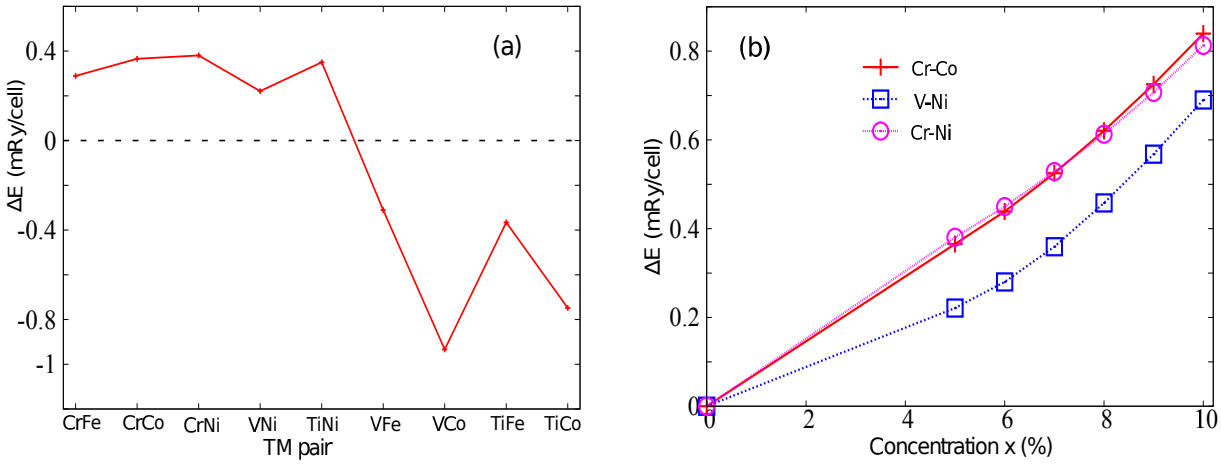

Fig. 5.8 (a) Stability trends, and (b) magnetic behavior for codoping of Cr-Co, Cr-Ni, and V-Ni pair in $Cu(In_{1-2x}X_xY_x)S_2$ with doping concentration x (%) versus total energy difference $\Delta E(x)$ per cell.

The magnetic behaviors of the target half metals in the AF spin state is shown in **Fig.** 5.8 (a) and **Fig.** 5.8 (b), where the total energy difference per unit cell with TM pair and doping concentrations are plotted, respectively. In **Fig.** 5.8 (a), the upper panel (positive energy part) denotes the stability of AF and FiM states, whereas the lower panel (negative energy part) denotes the lower total energy of DSM state. The trends in **Fig.** 5.8 (b) show a gradual increase of energy difference with increasing doping concentration. The mechanism seems to be double-exchange type rather than p-d hybridization. Although both mechanisms more or less compete, the double-exchange mechanism is dominant.

5.6.3 *Enthalpy of Formation*

Using the KKR-CPA method, enthalpy of formation of $Cu(In_{1-2x}Cr_xCo_x)S_2$ is calculated relative to the host material, ordered compound $CuCrS_2$ and bulk elements as

$$\Delta H_{\rm f} = {\rm E}[{\rm Cu}({\rm In}_{0.90}{\rm Cr}_{0.05}{\rm Co}_{0.05}){\rm S}_2] - [0.95{\rm E}({\rm CuInS}_2) + 0.05{\rm E}({\rm CuCrS}_2) - 0.05{\rm E}({\rm In}) + 0.05{\rm E}({\rm Co})] \tag{5.2}$$

A similar relation is used for Cr-Ni codoped case. Since the ordered form of the compound $CuVS_2$ is non-exist, the formation enthalpy of $Cu(In_{1-2x}V_xNi_x)S_2$ is calculated relative to the host compound and bulk elements as

$$\Delta H_{\rm f} = {\rm E}[{\rm Cu}({\rm In}_{0.90}{\rm V}_{0.05}{\rm Ni}_{0.05}){\rm S}_2] - [{\rm E}({\rm CuInS}_2) - 0.1{\rm E}({\rm In}) + 0.05{\rm E}({\rm V}) + 0.05{\rm E}({\rm Ni})] \tag{5.3}$$

The relative elements are taken as body centered tetragonal In, body centered cubic (bcc) V, bcc Cr, hexagonal close packed (hcp) Co, and face centered cubic (fcc) Ni. Experimental cell parameters of the elements are picked up from Ref. [10]. The cell parameters and atomic sites of rhombohedral $CuCrS_2$ (space group $R3m$ and number 160) are taken from Ref. [11] and Ref. [12], respectively. Enthalpy of formations are listed in **Table** 5.5.

Table 5.5 Enthalpy of formation at 5% concentration of each magnetic ion in Rydberg per formula unit.

Composition	$\Delta H_{\rm f}$ (Ry/f.u.)
$Cu(In_{0.90}Cr_{0.05}Ni_{0.05})S_2$	0.014
$Cu(In_{0.90}Cr_{0.05}Co_{0.05})S_2$	0.011
$Cu(In_{0.90}V_{0.05}Ni_{0.05})S_2$	0.041

Table 5.5 shows that positive but rather small values of formation enthalpy favors for solid mixture to fabricate the proposed half metals. At T=0 K the ions are segregated to a relatively higher energy phases and rather challenging to fabricate a target material. The disordered phases will be stabilized through entropy at some higher temperatures.

5.7 Hyperfine Fields

The hyperfine interaction between electrons and nuclei leads a splitting in atomic spectra. Hyperfine fields (HF) are calculated from the spin density difference between up- and down spin of s electrons at the nuclear position (r=0). Calculated magnetic states can be determined by HF at the impurity sites with a probe beam. The spin density m(r=0) at the nuclear position provides the HF [13] as given by equations (2.87) and (2.88). The equation (2.88) is the non-relativistic form of the Fermi contact term, whereas in the scalar relativistic formulation a finite nuclear size (Thomson radius) is assumed [14].

5.7.1 Hyperfine Fields in Antiferromagnetic States of Cu(InAB)S_2

Table 5.6 Succinct of total moments (M_T), local spin moments (SM), and total hyperfine fields (H^t_{hf}) in KG at Cr and Co site.

Composition	$M_T(\mu_B/\text{cell})$	SM(μ_B/Cr)	SM(μ_B/Co)	$H^t_{hf(KG/Cr)}$	$H^t_{hf(KG/Co)}$
$Cu(In_{0.94}Cr_{0.03}Co_{0.03})S_2$	0.003	−3.27	2.770	226.82	−179.46
$Cu(In_{0.92}Cr_{0.04}Co_{0.04})S_2$	0.01	−3.25	2.775	226.20	−182.18
$Cu(In_{0.90}Cr_{0.05}Co_{0.05})S_2$	0.03	−3.24	2.779	225.96	−184.21
$Cu(In_{0.88}Cr_{0.06}Co_{0.06})S_2$	0.05	−3.23	2.782	225.99	−185.81
$Cu(In_{0.86}Cr_{0.07}Co_{0.07})S_2$	0.07	−3.22	2.784	226.16	−187.12
$Cu(In_{0.84}Cr_{0.08}Co_{0.08})S_2$	0.08	−3.21	2.785	226.37	−188.23
$Cu(In_{0.82}Cr_{0.09}Co_{0.09})S_2$	0.10	−3.20	2.786	226.56	−189.20
$Cu(In_{0.80}Cr_{0.10}Co_{0.10})S_2$	0.12	−3.19	2.787	226.71	−190.07

The global, local and very local magnetic properties, listed in **Table** 5.6, which is obtained from chalcopyrite type DMS $Cu(In_{1-2x}Cr_xCo_x)S_2$ for a series of doping concentrations. Local moments and HF at two magnetic ionic sites are in antiparallel order, similar to the spin moments and HF at a given site. In a relatively higher

concentration case impurity d DOS spread more compare to a smaller concentration case and produce induced moments and HF by mixing with the neighboring local DOS. Therefore, the trends of local moments and HF are determined by the induced moments and HF on the nonmagnetic host sites. No significant changes occur in the absolute values of the hyperfine fields for different concentrations. AF states can be separated from the FM states by the magnetization and the energy level shift in the HF. The trends of total HF at Cr, and Co sites as a function of doping concentrations are given in **Fig.** 5.9 (a,b).

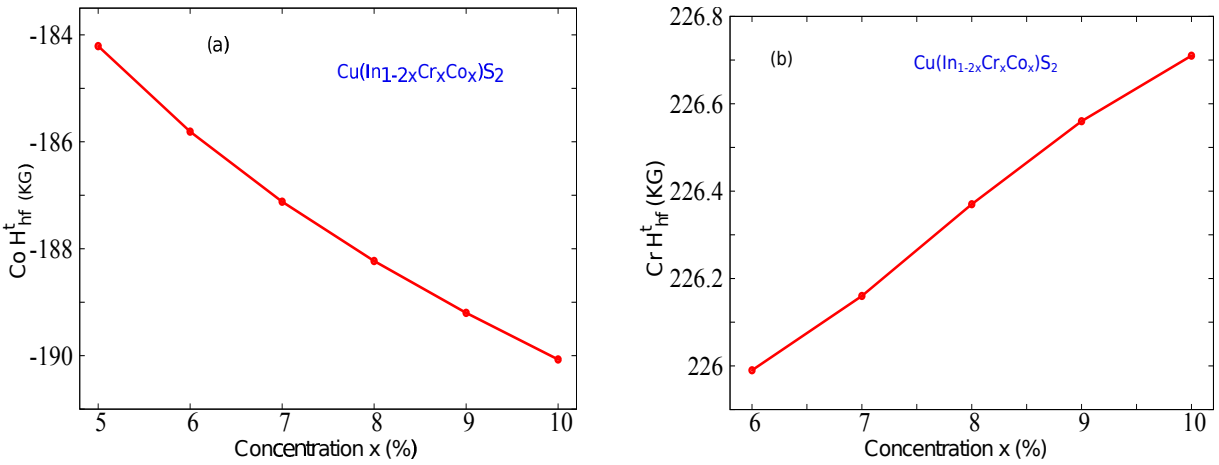

Fig. 5.9 Trends of total hyperfine fields at (a) Co, and (b) Cr site for a systematic codoping of impurity concentration at host In^{3+} site.

Magnetic states can be detected through HF by a probe nuclei. The sensitivity of the probe nuclei to the magnetic states depend on the magnetic systems. Separate probe nuclei are effective in distinguishing the AF state from the FM or DSM states. Because the HF of impurity probes are mostly associated with s electron states. Since the position of the impurity s state relative to the Fermi level varies in different systems, an effective probe nuclei is necessary to determine the magnetic state. Since the magnitude of HF at AF state is unequal at the two impurity sites and acts in opposite directions and net HF at DSM state is zero, the magnetic states can be easily determined.

Table 5.7 Summary of total moments (M_T), local spin moments (SM), and total hyperfine fields (H^t_{hf}) in $Cu(In_{0.90}V_{0.05}Ni_{0.05})S_2$ at V and Ni site for ferromagnetic (FM), antiferromagnetic (AF), and disordered spin moment (DSM) state calculation.

State	$M_T(\mu_B/\text{cell})$	$SM(\mu_B/V)$	$SM(\mu_B/Ni)$	$H^t_{hf(KG/V)}$	$H^t_{hf(KG/Ni)}$
FM	0.41	1.989	1.578	−145.09	−116.89
AF	0.03	−1.966	1.584	142.51	−121.94
DSM	0.00	± 1.984	± 1.567	∓ 145.52	∓ 117.92

From **Table** 5.7 we see that AF state shows negligibly small net moment by compensated local spins and induced moments relative to FM state, whereas disordered paramagnetic state (DSM) shows a zero net moment and zero net HF. In FM calculation, the local spins are parallel and antiparallel in AF case. HF are inversely proportional to the corresponding local spin moments.

5.8 Discussion on Antiferromagnetic States and Null Moment

Ferrimagnetic or AF specimen is designed by minimum two magnetic ions doped at the semiconductor host. Electronic structures and magnetic properties favor some states as AFHM. Local spin moments (LSM) at the impurity sites are oppositely polarized and less compensated LSM cases provide FiM ground state and full cancellation of LSM cases give the AF ground state relative to a reference DSM state. Magnetic transition temperatures calculated by MFA are higher than room temperatures in many cases, which is an attracting point for room temperature applicability of the magnetic metals. One demands the net moments to be null in stable AF state as well as the half metallicity for spintronics devices. Negligibly net moments are found in some codoped, namely Cr-Co, and V-Ni pair cases (**cf. § 5.3.2**). Half metallic AF with zero net moments are applicable where required (i) vanishing effect of external field and zero spontaneous magnetization,

(ii) no magnetic interaction between the probe tip and sample, and (iii) in spin polarized tunneling microscopy (SP-STM) and spectroscopy [1] as a tip material for data reading from a magnetic sample. SP-STM is sensitive to the spin orientation of tunneling electrons and capture atomically resolved images of the sample surfaces. STM measures the local DOS in a sample where the total tunneling current is proportional to the integrated DOS. The tunneling current depends on the relative orientations between the tip and sample spins. SP-STM is neither sensitive to total magnetic moment of the sample nor the applied magnetic field.

5.9 References

[1] H. van Leuken and R.A. de Groot, Phys. Rev. Lett. **74**, 1171 (1995).

[2] H. Akai and M. Ogura, Phys. Rev. Lett. **97**, 026401 (2006).

[3] H. Akai, Phys. Rev. Lett. **81**, 3002 (1998)

[4] M. Ogura, Y. Hashimoto and H. Akai, Phys. Status Solidi c **3**, 4160 (2006).

[5] P. Weinberger, Electron Scattering Theory for Ordered and Disordered Matter (Clarendon, Oxford, 1990).

[6] A.N. Andriotis, S. Lisenkov and M. Menon, J. Phys.: Condens. Matter **23**, 086004 (2011).

[7] P.W. Anderson, Phys. Rev. **79**, 350 (1950).

[8] C. Zener, Phys. Rev. **82**, 403 (1951).

[9] L. Bergqvist and P.H. Dederichs, J. Phys.: Condens. Matter **19**, 216220 (2007).

[10] C. Kittel, Introduction to Solid State Physics, 8th ed. John Wiley & Sons, Inc. New York, (2005).

[11] H. Hahn and C. de Lorent, Z. Anorg. Allgem. Chem. **290**, 68 (1957).

[12] P.F. Bongers, C.F. van Bruggen, J. Koopstra, W.P.F.A.M. Omloo, G.A. Wiegers and F. Jellinek, J. Phys. Chem. Solids **29**, 977 (1968).

[13] S. Blügel, H. Akai, R. Zeller and P.H. Dederichs, Phys. Rev. B **35**, 3271 (1987).

[14] H. Akai, M. Akai, S. Blügel, B. Drittler, H. Ebert, K. Terakura, R. Zeller and P.H. Dederichs, Prog. Theor. Phys. Suppl. **101**, 11 (1990).

Chapter 6

Summary

Electronic density of states and band structures of the group I-III-VI_2 based host chalcopyrites represent the non-magnetic, wide and direct energy gap semiconductors. These wide gap semiconductors are the starting point to design **new type of DMS** for spintronics devices. Therefore, to obtain novel class DMS, $3d$ TM doped chalcopyrite compounds for single doping and codoping cases are calculated to obtain stable magnetic states and half metallicity in FM and AF ordering of spins, respectively. In each case, local and total magnetic properties are calculated in favor of the material stability and critical temperatures are estimated by MFA.

In the present study we implemented the following points throughout the dissertation. (i) Proper crystal structure is considered in calculation. (ii) We explored stable FM half metallic states and calculated T_{C} for applications in Ti, V, Cr, and Mn doped cases. (iii) The concept of DMS is generalized in doped system. (iv) FiM and AF states are properly addressed with T_{C} and T_{N}, respectively, in terms of net moment in pair doped cases. (v) Mechanisms for magnetic stability are explained in detail for chalcopyrite-type DMS.

FM states by single doping can be the ground state or an excited state compare to a DSM state. FM ground state has lower total energy than the corresponding DSM state, which exhibit the salient features of half metallicity with perfect spin polarization at the Fermi level and predict Curie temperatures higher than room temperature. Ti, Cr, and Mn doped compounds are preferable as FHM in KKR-CPA calculation. On the contrary, in V doped case, insulating band structures are found with energy gaps at the majority and

minority spin channels in FLAPW calculation, whereas FM half metallicity is obtained by broadening of majority d states while disordered calculation in KKR-CPA case. Net moments and Curie temperatures increase steadily with the impurity concentrations in a doped system. The dominating mechanism in stable DMS can be understood from the magnetic behaviors, namely the energy difference $\Delta E(x)$ between FM and DSM state versus concentrations.

Spin-orbit (SO) interaction produces a small but finite orbital moments along with local spin moments for $3d$ TM. The critical temperature in SO inclusion case is often found higher than SO exclusion (scalar relativistic approximation) case. Because, LS coupling energy (perturbative energy) is an additive quantity in total energy calculation, and hence the total energy difference between FM and DSM states is lower (higher) in SO coupling inclusion (exclusion) case. Therefore, LS coupling may not be neglected.

We obtain FiM and AF metallic and half metallic states by codoping TM at group III^{3+} site of host semiconductors. Calculated electronic state densities and magnetic properties imply that some of the codoped states are lower in energy and half metallic having higher magnetic critical temperatures. Among those Cr-Co, Cr-Ni, Mn-Co, and V-Ni pair doped compounds are probable as AFHM with compensated net moments. Many of other codopant cases, we obtain FiM half metallicity with a rather small net moments and antiparallel local spin moments. FiM state is the ground state by double-exchange interaction, whereas the DSM state shows lower total energy than FiM states by super-exchange coupling.

For instance, in the cases of Cr-Co and V-Ni pair doped in $CuAlSe_2$, the negligibly small net moments can be realized as (i) two TM produce nearly equal and opposite spin moments, (ii) resultant spin moments are further canceled by induced spin moments at the neighboring non-magnetic ion sites. Otherwise, induced moments at the non-magnetic sites enhance the resultant spin moments and give rise to a large net moments. Therefore, in terms of net moments Cr-Co and V-Ni pairs can be candidates to design AFHM. Zero net moments have selective applications where required the vanishing effects of external field and zero spontaneous magnetization. Spin-polarized scanning tunneling microscopy

(SP-STM) prefers AFHM as a tip material for data reading on a sample (magnetic) surface.

Hyperfine field (HF) is a very local spectral parameter in a magnetic system often investigated by nuclear magnetic resonance (NMR) or Mössbauer spectroscopic experiment. Since at a given magnetic site the orbital moment and dipole moment are much smaller than the corresponding spin moment, therefore to a good approximation, the Fermi contact term is dominated in the HF of the present systems. The contact term originates from a different density of s electrons with spin-up and spin-down at the nuclear position. HF are proportional to the corresponding spin moments. In a relatively higher concentration doping case impurity d DOS spread more compare to a smaller concentration case and produce induced moments and induced HF by mixing with the neighboring local DOS. Therefore, the trends of local moments and HF are determined by the induced moments and induced HF on the non-magnetic host sites.

Materials stability can be understood by formation energy calculation. Calculated energy of formations is quite small (less than a half eV per formula unit) and would stabilize the doped materials through entropy at some higher temperatures. The designed FM, FiM, and AF half metals can be promising candidates for the next-generation spintronic and opto-electronic applications.

6.1 Trends on Calculated Results

We found various similar and dissimilar trends in the calculated results for doped and codoped compounds based on different host semiconductors. Results on $Cu(Al_{1-x}A_x)Se_2$ and $Cu(In_{1-x}A_x)S_2$ differ because we are mixing TM at host Al and In sites, same group III elements but they differ in many ways. For instance, atomic number Z of In is about 4 times larger than that of Al and Al p states are much deeper than In p states. On the contrary, in $Ag(Al_{1-x}A_x)Se_2$ or $Ag(Al_{1-x}A_x)S_2$ the results differ from Cu based systems, because Ag d states are much deeper than the corresponding Cu d states. In addition, S p states are much deeper than the corresponding Se p states.

Besides, if the effective range of interaction is smaller than the mean inter-atomic

distance, the system loses its ferromagnetic property, usually known as the percolation effect. MFA overestimates the critical temperatures at low concentration region mainly for the percolation tendency. In addition, no spin fluctuation is taken into account in MFA. At higher concentrations the results are reasonable. Unfixed MT radii may provide some exaggerated formation energy.

How to Improve the Present Work?

In the present study:

1. We grossly used a plain GGA to treat many electron exchange and correlation energy, whether there have any screening effect or not and for this GGA+SIC, GGA+U, screened KKR and KKRimp packages can be used for such calculations.

2. Despite use of many empty MT spheres to make the structure close packed, still there have some open structures in the unit cell, thereof to have a good space filling, full potential KKR, or a spin polarized relativistic KKR (**SPRKKR**) code can be promising.

6.2 Outlook

The present work can be extended in many ways. We expect to calculate optical properties, namely X-ray absorption spectra (XAS) such as X-ray magnetic circular dichroism (XMCD), X-ray magnetic linear dichroism (XMLD) for dipole and quadrupole transitions and Magneto-crystalline anisotropy energy (MAE), electrical conductivity, and exchange interactions J_{ij}. One possibility is to apply theories beyond GGA, such as GGA+SIC, GGA+U, GW scheme, and optimized effective potential (OEP) method implemented in KKR-Green's function and calculate electronic structures and magnetic properties on the same footings. KKR full-potential can be another approach to compare and find the discrepancies (if any) in the existing results. Collaborative work with an experimental group might verify the numerical results. Secondly, some other computational codes, namely **KKRimp** a full potential KKR-CPA package, **KKRnano** a large scale calculation code and **SPRKKR** a fully relativistic version of KKR approach can be used to compare and improve the present work. Test calculations based on some of the above methods shall be reported in due course.

Appendix A

A.1 Mean Field Approximation

Mean field approximation (MFA) is a statistical approach to find an average field of a magnetic system.

Heisenberg Model: According to classical Heisenberg model the spin Hamiltonian can be written as

$$H^{\text{spin}} = -\sum_{i \neq j} J_{ij} \mathbf{S}_i \cdot \mathbf{S}_j \tag{A.1}$$

where J_{ij} is the exchange interaction between the local spin moments at sites i and j. The bold letters denote the vector quantity. It favors parallel spins if J_{ij} is positive and antiparallel spins for negatice J_{ij}. Including the magnitude of the local spin moments in J_{ij}, expression (A.1) can be rewritten as

$$H^{\text{spin}} = -\sum_{i \neq j} J_{ij} \hat{e}_i \cdot \hat{e}_j \tag{A.2}$$

where $\hat{e}_i$ and $\hat{e}_j$ are unit vectors pointing in the directions of local spin moments. The pair interaction parameters J_{ij} can be estimated from an energy change for tilting the local spins at sites i and j while fixing the remaining spin moments. Suppose the spin moments are parallel. Variation in total energy to turn the two spin moments in other directions by opposite angles $\pm\,\theta/2$ is

$$\Delta E = J_{ij}\, 2\, \sin^2(\theta/2) = J_{ij}\, (1 - \cos\theta) \approx \frac{1}{2}\, J_{ij}\theta^2 \tag{A.3}$$

Since cos(x)=1-$\frac{x^2}{2!}$+$\frac{x^4}{4!}$-$\frac{x^6}{6!}$+... for all x. The higher order terms can be neglected if θ is small. The same energy change is evaluated from the first-principles calculations by using the local force theorem [1]

$$\Delta E = -\int^{\epsilon_{\mathrm{F}}} d\epsilon\ \Delta N(\epsilon) \tag{A.4}$$

where $N(\epsilon)$ is the number of electrons and $\Delta N(\epsilon)$ is the difference of the electron states for the rotation of local moments. In multiple scattering (KKR) theory, the number of electrons $N(\epsilon)$ is calculated by Lloyd's formula (**cf. equation 2.74**).

Mean Field: Assume the atoms of a lattice each with one unpaired s electron (angular momentum zero). This can be treated as model of a 'spin lattice' essential for study ferromagnetism via exchange interaction. The Hamiltonian with an additional term of applied field $\mathbf{B}_a$ is

$$H = -\sum_i \mathbf{S}_i \cdot \Big(\sum_j J_{ij} \mathbf{S}_{ij} \Big) - \mathrm{g}\,\mu_{\mathrm{B}} \mathbf{B}_a \sum_i \mathbf{S}_i \tag{A.5}$$

$$= -\sum_i \sum_j J_{ij} \mathbf{S}_i \cdot \mathbf{S}_{ij} - 2\mu_{\mathrm{B}} \mu_0 \mathbf{H}_a \sum_i \mathbf{S}_i \tag{A.6}$$

where the index i runs over all atoms and j over all the neighbors of an atom that take part in the exchange interaction. The sum over j refers to nearest neighbors of the site i. The magnetic induction, $\mathbf{B}$, in vacuum is related to magnetic field strength, $\mathbf{H}$, by $\mathbf{B} = \mu_0 \mathbf{H}$ with $\mu_0 = 4\pi \times 10^{-7}$ Vs/Am is the permeability of free space. g is the *Landé factor* for electron given in expression (4.10).

In the MFA, the spin operator product in (A.6) is replaced by the product of the spin operator $\mathbf{S}_i$ and the expectation value of the spin operators of all the neighbors $\langle \mathbf{S}_{ij} \rangle$. Therefore, in the MFA, the Hamiltonian becomes [2]

$$H_{\mathrm{MF}} = -\sum_i \mathbf{S}_i \cdot \Big(\sum_j J_{ij} \langle \mathbf{S}_{ij} \rangle + \mathrm{g}\,\mu_{\mathrm{B}} \mathbf{B}_a \Big) \tag{A.7}$$

Hence, the exchange coupling experiences the character of a molecular (internal) field

$$\mathbf{B}_{\mathrm{MF}} = \frac{1}{\mathrm{g}\mu_{\mathrm{B}}} \sum_j J_{ij} \langle \mathbf{S}_{ij} \rangle \tag{A.8}$$

For homogeneous system $\langle \mathbf{S}_{ij} \rangle$ is the same for all atomic sites. The average value $\langle \mathbf{S}_{ij} \rangle = \langle \mathbf{S} \rangle$ can be expressed in terms of the magnetization

$$\mathbf{M} = \mathrm{g}\mu_{\mathrm{B}} \frac{N}{V} \langle \mathbf{S} \rangle \tag{A.9}$$

where N/V is the number of atoms per unit volume. Using (A.9) into (A.8), we therefore obtain the mean field expression

$$\mathbf{B}_{\mathrm{MF}} = \frac{V}{N\mathrm{g}^2\mu_{\mathrm{B}}^2} \, z \, J \, \mathbf{M} \tag{A.10}$$

Similarly, mean field in terms of magnetic field strength is given by (with g=2)

$$\mathbf{H}_{\mathrm{MF}} = \frac{V}{4N\mu_0^2 \, \mu_{\mathrm{B}}^2} \, z \, J \, \mathbf{M} \tag{A.11}$$

where z is the number of nearest neighbors (NN) of the site i and the exchange interaction is restricted to the z NN (coordination number).

Curie Temperature: The total energy difference ΔE^{H} in the MFA of Heisenberg model can be calculated as

$$\Delta E^{\mathrm{H}} = S^2 x^2 \sum_{j \neq 0} J_{0j} \tag{A.12}$$

where x is the composition of the magnetic ions, S is the magnitude of the spin moment (that can be absorbed in J) and j sums over all sites of the entire crystal. In the one-hand, ΔE^{H} can be directly evaluated from the total energy difference ΔE computed from first-principles theory of CPA treatments in KKR. On the other hand, in the mean-field theory of the Heisenberg model, T_{C} can be estimated by the Brillouin function expression, leading to

$$k_{\mathrm{B}} T_{\mathrm{C}} = \frac{2}{3} S^2 x \sum_{j \neq 0} J_{0j} \tag{A.13}$$

Finally, the Curie temperature evaluated from the first-principles calculation is given by

$$k_{\mathrm{B}} T_{\mathrm{C}}^{\mathrm{MFA}} = \frac{2}{3} \frac{\Delta E}{x} \tag{A.14}$$

where k_{B} is the Boltzmann constant. Magnetic critical temperatures T_{C} in MFA is over-estimated, particularly near the range of lower dilute limits, which might be due to some percolation effects of the cell atoms.

A.2 Total Energy in Muffin-Tin Potential Approximation

The total energy including all core contributions per unit cell in atomic unit of a many-electron system with the static nuclei is given as the sum of three terms: the single-particle kinetic energy, the electrostatic energy (all Coulombic interactions or Hartree energy), and the exchange-correlation energy.

$$E = T_{\rm s} + E_{\rm es} + E_{\rm xc} \tag{A.15}$$

$$E = E_{\rm band} - E_{\rm pot} + E_{\rm es} + E_{\rm xc} \tag{A.16}$$

where $T_{\rm s}$ is splitted as $E_{\rm band} - E_{\rm pot}$ and is given by

$$T_s = \sum_i^{occ} (\psi_i, -\nabla^2\,\psi_i) = \sum_i \int \psi_i^*(-\nabla^2)\,\psi_i\,d^3r \tag{A.17}$$

$$= \sum_i^{occ} \epsilon_i - \sum_i^{occ} (\psi_i, V_{\rm eff}(r)\,\psi_i) = \sum_i^{occ} \epsilon_i - \int n(r)\,V_{\rm eff}(r)\,d^3r \tag{A.18}$$

where ψ_i's are the solutions of an effective one-electron Kohn-Sham equation and the sum runs over all occupied electron states. $n(r) = \sum_i |\psi_i(r)|^2$ is the electron charge density. The separated out first term in (A.18) is the sum of all the occupied single-electron energies and is regarded as a *"band energy"*. In terms of density of states (DOS) $n^j(E)$ (at atom j or $j^{\rm th}$ site) the band energy can be expressed as

$$E_{\rm band} = \sum_i \epsilon_i = \int_{-\infty}^{E_F} E\,n^j(E)\,dE = NE_F - \int_{-\infty}^{E_F} N(E)\,dE \tag{A.19}$$

where N is the total number of electrons, $N(E)$ is the integrated DOS, $n^j(E)$ is given by the imaginary part of Green's function along the complex energy contour. The spike functions produced by Green's function cannot be integrated. To overcome this difficulty, we introduce a state function $Z(E)$ [3] whose imaginary part gives the total number of states per atom below a real energy E. $Z(E)$ corresponds the integrated DOS $N(E)$.

$$Z(E) = \int_\tau \frac{dk}{\tau} \left\{ \ln\det\left|-E+(k+K)^2\right| + \ln\det\left|1-t(E)G^0(k;E)\right| \right\} - \ln\det\left|\frac{e^{i\eta_\ell(E)}}{\Lambda_\ell(E)}\right| \tag{A.20}$$

where K is a matrix in reciprocal lattice vector, τ is the Brillouin zone volume, t is the atomic t matrix, G^0 is the free space Green's function and Λ_ℓ is the normalization factor

defined as

$$\Lambda_\ell(E) = \lim_{r\to 0} \frac{(2\ell+1)!! R_\ell(r)}{(\sqrt{E}r)^{\ell+1}} \tag{A.21}$$

where $R_\ell(r)$ is a radial wave function. This provides a normalization for the phase shift η_ℓ. Such phase shift normalization makes $Z(E)$ analytical in the upper complex half plane and removes all the singularities originate from the resonances in the single site scattering phase shift $e^{\mathrm{i}\eta_\ell(\mathrm{E})}$.

The band energy is then (sum of occupied states energy up to Fermi level) obtained by energy integration of $Z(E)$ up to Fermi level:

$$E_{\mathrm{band}} = -\frac{1}{\pi}\Im\left\{ Z(E_F)\, E_F - \int_{-\infty}^{E_F} Z(E)\, dE \right\} \tag{A.22}$$

The potential energy is subtracted from the band energy which corresponds nothing but the kinetic energy of the non-interacting electron system.

$$E_{\mathrm{pot}} = \sum_j x_j \int_0^{R_{\mathrm{mt}}} r^2\, n^j(r)\, V_{\mathrm{eff}}^j(r)\, dr = \sum_j x_j \int_0^{R_{\mathrm{mt}}} n^j(r)\, V_{\mathrm{eff}}^j(r)\, d^3r \tag{A.23}$$

where $V_{\mathrm{eff}}^j(r)$ is the single-site potential at atom (site) j, $n^j(r)$ is the electron density inside the muffin-tin sphere of atom j and x_j is a weighting factor. The electrostatic energy is the sum of all Coulombic interactions given by Janak [4]

$$E_{es} = \sum_j x_j \left\{ 32\pi^2 \int_0^{R_{\mathrm{mt}}} r\, n^j(r)\, dr \int_0^r r'^2\, n^j(r')\, dr' - 8\pi Q_j \int_0^{R_{\mathrm{mt}}} r\, n(r)\, dr \right\} - \frac{C}{2}\frac{Q_0^2}{a} \tag{A.24}$$

where a is the lattice parameter and C, which is a different constant for each crystal structure, is called Madelung coefficients. Q_j is the nuclear charge (proton number) of atom j and Q_0 is the number of electrons per atom accumulated in the interstitial space. The interstitial charge is given by

$$Q_0 = n_0\Omega_0 = \sum_j x_j \left\{ Q_j - 4\pi \int_0^{R_{\mathrm{mt}}} r^2\, n^j(r)\, dr \right\} \tag{A.25}$$

where n_0 is the constant charge density in the interstitial region and Ω_0 is the interstitial volume and is given by

$$\Omega_0 = \Omega - \frac{4}{3}\pi R_{\mathrm{mt}}^3 \tag{A.26}$$

where Ω is the volume of the unit cell. The exchange-correlation energy per atom in the local spin density approximation (LSDA) is

$$E_{\rm xc} = \sum_j x_j \int_0^{R_{\rm mt}} r^2\, n^j(r)\, \epsilon_{\rm xc}(n^j)\, dr + Q_0\, \epsilon_{\rm xc}(n_0^j) \tag{A.27}$$

where $\epsilon_{\rm xc}$ is the exchange-correlation energy for a homogeneous electron gas.

A.3 Relativistic Dirac Equation

Relativistic effects are essential for atoms with relatively higher atomic numbers. Basically they originate from the deep core region. Dirac Hamiltonian for free particle

$$H_{\rm D} = c\alpha \cdot \mathbf{p} + \beta mc^2 + 0 \tag{A.28}$$

For free particles the removal of the rest mass term from the Hamiltonian is done by a unitary transformation, known as Foldy-Wouthuysen (FW) transformation. This infact implies a neglect of retardation. Now in a potential $V(r)$ the Hamiltonian is

$$H_{\rm D} = c\alpha \cdot \mathbf{p} + \beta mc^2 + V(r) \tag{A.29}$$

Using natural units (obtained naturally from the properties of nature) $c = G = \hbar{=}\kappa_{\rm B}{=}1$, where c is the speed of light, G is the gravitational constant, $\hbar$ is the reduced planck constant, and $\kappa_{\rm B}$ is the Boltzmann constant, the Dirac Hamiltonian can be written as

$$H_{\rm D} = \alpha \cdot \mathbf{p} + \beta m + V(r) \tag{A.30}$$

and the corresponding time-independent Dirac equation for a relativistic electron is

$$H_{\rm D}\, \Phi = \Big(\alpha \cdot \mathbf{p} + \beta m + V(r)\Big)\Phi = E\, \Phi \tag{A.31}$$

where βm is the rest mass of the electron and $-e < 0$ is its charge, $\mathbf{p} = -i\hbar\nabla$ is the linear momentum operator. Customarily for relativistic electron, we shall use rational relativistic units as $\hbar = m = c{=}1$, m is the electron mass and the rest energy, $E_0 = mc^2{=}1$. Then the time-independent wave equation become

$$H_{\rm D}\, \Phi = \Big(\alpha \cdot \mathbf{p} + \beta + V(r)\Big)\Phi = E\, \Phi \tag{A.32}$$

The relativistic theory of KKR Green's function is based on the following Dirac Hamiltonian for a spin-polarized system

$$\Big[-i\alpha \cdot \nabla + \beta m + V_{\text{eff}}(r) + \beta\sigma \cdot B_{\text{eff}}(r) \Big] \Phi_i(r) = E_i \, \Phi_i(r) \tag{A.33}$$

where the effective magnetic field in terms of spin magnetization $m(r)$ can be expressed as

$$B_{\text{eff}}(r) = B_{\text{ext}}(r) + \frac{\partial E_{\text{xc}}[n, m]}{\partial m(r)} \tag{A.34}$$

The spin dependent potential is formed from a relativistic spin density functional theory. Once the potentials $V_{\text{eff}}(r)$ and $B_{\text{eff}}(r)$ are known, we can immediately solve the corresponding single site Dirac equation for each type of atom. Generally, the effective magnetic field $B_{\text{eff}}(r)$ is omni-directional (non-collinear), and can be simplified by choosing a directional as $B_{\text{eff}}(\mathbf{r}) = B_{\text{eff}}(r)\hat{e}_z$. Thence the single site Dirac equation can be solved and the ansatz

$$\Phi_\nu = \sum_\Lambda \Phi_{\Lambda\nu}$$

is used with the partial waves $\Phi_{\Lambda\nu}$ having the same form as the linearly independent solutions of a spherically symmetric potential:

$$\Phi_\Lambda(r, E) = \begin{pmatrix} g_k(r, E)\chi_\Lambda(r) \\ i f_k(r, E)\chi_{-\Lambda}(r) \end{pmatrix} \tag{A.35}$$

where g_k and f_k are radial wave functions and $\chi_{\pm\Lambda}$ are the corresponding spherical harmonics.

Appendix B

B.1 Functional Derivative

Functional derivative (FD) is a differentiation of a functional with respect to another function in the function space. The function either maximizes or minimizes the given functional. We restrict on a functional *local* in x of the form

$$J[y(x)] = \int_{x_1}^{x_2} f(x, y, y', y'', ..., y^n)dx \tag{B.1}$$

where f depends on the value of $y(x)$ and many of its derivatives. By definition

$$\frac{\delta J[f(x)]}{\delta f(y)} = \lim_{\epsilon \to 0} \frac{J[f(x) + \epsilon\delta(x-y)] - J[f(x)]}{\epsilon} \tag{B.2}$$

The function

$$\frac{\delta J}{\delta y(x)} \equiv \frac{\partial f}{\partial y(x)} - \frac{d}{dx}\Big(\frac{\partial f}{\partial y'}\Big) \tag{B.3}$$

is called the functional (or Fréchet) derivative of J with respect to $y(x)$. In general we can write FD as [5]

$$\delta J = \sum_i \frac{\partial J}{\partial y_i}\delta y_i \to \int_{x_1}^{x_2} dx\Big(\frac{\delta J}{\delta y(x)}\Big)\delta y(x) \tag{B.4}$$

where the discrete index i is replaced by continuous label x and sums by integrals. The coefficient of $\delta y(x)$, denoted as $\frac{\delta J}{\delta y(x)}$, is called the FD of J with respect to y at the point x.

B.2 Green's Function

suppose $\hat{L}$ is a linear operator such as differentiation, Hamiltonian and so on. To solve an inhomogeneous equation as

$$\hat{L}f(r) = g(r) \tag{B.5}$$

we find a Green's function which results delta (spike) functions when such operator acts as

$$\hat{L}G(r, r') = \delta(r - r') \tag{B.6}$$

The solution is expressed as the sum of homogeneous and inhomogeneous parts

$$f(r) = f_0(r) + \int dr' G(r, r') g(r'), \tag{B.7}$$

where f_0 is the solution of the homogeneous part with $\hat{L}f_0(r)$=0. We can verify the solution (B.7) by putting back into the left side of (B.5) that $f(r)$ truly satisfy the relation (B.5).

Green's function in operator form is $\hat{G}$=$\frac{1}{\hat{E}-\hat{H}}$ when act on a state $|r'\rangle$ then $G|r'\rangle = (\frac{1}{\hat{E}-\hat{H}})|r'\rangle$ hence if a conjugate bra state projects on it, we get

$$\langle r|G|r'\rangle = \langle r|\frac{1}{\hat{E} - \hat{H}}|r'\rangle \tag{B.8}$$

In matrix form the Green's function matrix with elements r and r' is

$$G(r, r') = \sum_{kk'} \langle r|k\rangle\langle k|\frac{1}{\hat{E} - \hat{H}}|k'\rangle\langle k'|r'\rangle \tag{B.9}$$

where the imposed completeness conditions are

$\sum_k |k\rangle\langle k| = 1$ and $\int dk|k\rangle\langle k| = 1$

Now the orthogonality conditions are

$\langle r|r'\rangle = \delta(r - r')$ and $\int dr\varphi_k^*(r)\varphi_{k'}(r)dr = \delta_{kk'}$

The closure (closed) property or completeness relation is

$$\int \sum_{k'} \varphi_{k'}^*(r')\varphi_{k'}(r)dr = (\delta_{rr'}) = 1 \tag{B.10}$$

if the volume of the integration includes the point $r' = r$ and otherwise zero, and if $|k\rangle$ is a normalized state then $\sum_k \langle k|k\rangle = 1$ and $\sum_{k'} \int_{-\infty}^{\infty} dk' \langle k|k'\rangle\langle k'|k\rangle = 1$

Using the above conditions the Green's function matrix can be written as

$$G(r,r') = \sum_{kk'} \langle r|k\rangle\langle k| \frac{1}{E - E_{k'}} |k'\rangle\langle k'|r'\rangle \tag{B.11}$$

$$G(r,r') = \sum_{kk'} \langle r|k\rangle \frac{1}{E - E_{k'}} \langle k|k'\rangle\langle k'|r'\rangle \tag{B.12}$$

if we do the k' sum or if $k' = k$ then for a normalized crystal momentum state we get

$$G(r,r') = \sum_{kk} \langle r|k\rangle \frac{1}{E - E_{k}} \langle k|k\rangle\langle k|r'\rangle \tag{B.13}$$

$$G(r,r') = \sum_{k} \langle r|k\rangle \frac{1}{E - E_{k}} \langle k|r'\rangle \tag{B.14}$$

Let an electronic (momentum) state is ket $|k\rangle$ and take an inner product with a complex conjugate of a spatial state bra $\langle r|$, which we define as a wave function $\varphi_k(r)$=$\langle r|k\rangle$ for the state $|k\rangle$. In fact this is the probability amplitude of finding the electron having crystal momentum k in some spatial region r. $\varphi_k(r)$ is a complex number, but $|\varphi_k(r)|^2$ is real known as the probability density $(1/m^3)$ and $\int |\varphi_k(r)|^2 dr$ is the probability to find the electron over the space r. Then in terms of a complete set of eigenfunctions of H with $\varphi_k(r)$ correspond to eigenvalues E_k, the following real space spectral representation can be obtained

$$G(r,r',E) = \sum_{k} \frac{\varphi_k(r)\varphi_k^*(r')}{E - E_k} \tag{B.15}$$

which represent an outgoing wave at r originating from a source at r'.

B.3 References

[1] A.I. Liechtenstein, M.I. Katsnelson, V.P. Antropov, and V.A. Gubanov, J. Magn. Magn. Mater. **67**, 65 (1987).

[2] H. Ibach and H. Lüth, Solid-State Physics, Springer, 4th ed. (2009).

[3] H. Akai and P.H. Dederichs, Phys. Rev. B **47**, 8739 (1993).

[4] J.F. Janak, Phys. Rev. B **9**, 3985 (1974).

[5] M. Stone and P. Goldbart, Mathematics for Physics, Cambridge univ. press, (2010).

Acknowledgements

In the tenure of my Ph.D. research, I have been assisted by many intelligentsias in a variety of ways. Here I take this opportunity to express my gratitude. I am grateful to Prof. Hisazumi Akai, my former advisor, for his encouragement, guidance and trained up me in 'state of the art' of research. He assisted me to carry on my Ph.D. research in the current subject. I heartily express my gratitude to Prof. Tamio Oguchi, my present advisor, after the retirement of Prof. H. Akai, to take care of my research in the remaining term. He would provide a lucid explanation of various concepts involved. His critical reading of the manuscript and thesis paper and subsequent corrections are much appreciated. Any lacking that remains are of course mine. I am thankful to Prof. K. Shirai, for frequent discussions on some topics related to my research and checking the dissertation. I am also grateful to Prof. Momida and Dr. Toyoda for sharing some computational tips related to my work.

I am thankful to all members of my thesis scrutinizing committee, Prof. T. Oguchi, Prof. K. Shirai, Prof. T. Ogawa, Prof. K. Kuroki and Prof. H. Kawamura. I thank Prof. H. Takabe and Prof. Luca for memorable $G30$ study excursion and exchange programs. We could discuss any topic frankly with Prof. Luca. Thanks also go to Prof. M. Ogura and Prof. Yamauchi. I like to thank some visiting faculties, Prof. H. Ebert, Prof. S. Blügel and Prof. J. Yu for valuable suggestions and discussion on my subject. Finally, I express sincerest thanks to Dr. Fukazawa, Dr. Nagata, Dr. Harashima and Dr. S. Doi for their tips on computation and valuable physics discussion. I thank my Lab members for passing an enjoyable moments. I also thank secretaries in the former Akai Lab, present Oguchi Lab and IPC office for their technical support while I belong to the respective Lab. Finally, I thank my family to whom I have been attributed the effort of mind, especially at my stress moment. AFNAN-kun, my beloved child, always refreshes me in all.

This work was partly supported by Ministry of Education, Culture, Sports, Science and Technology (MEXT) by the grant No. 105099. KKR-CPA program package "MACHIKANEYAMA 2002" and full-potential LAPW code "HiLAPW 2002" are used for numerical computation.

Conference / Symposium / Workshop Presentations

1. The Physical Society of Japan (JPS) 67$^{\text{th}}$ Annual (Spring) Meeting: **Poster** Presentation, March 24-27, 2012, Uegahara Campus, Kwansei Gakuin University, Hyogo, Japan. Materials design of chalcopyrite type semiconductor based **antiferromagnetic half metals** – M. Shahjahan and H. Akai

2. "International Workshop on Nano-Spintronics" and "JSPS Core-to-Core Program Kick-Off Meeting": **Poster** Presentation, June 29 - July 1, 2012, Osaka University, Osaka, Japan. Antiferromagnetic half metals based on transition metal doped chalcopyrite type semiconductor – M. Shahjahan, H. Akai and T. Oguchi

3. ISSP-CMSI international symposium on "MAterial Simulation in Petaflops era (MASP2012)": **Poster** Presentation, July 12 - 13, 2012, ISSP, Kashiwa Campus, Chiba, The University of Tokyo, Japan. Magnetic properties of chalcopyrite based antiferromagnetic half metals – M. Shahjahan and T. Oguchi

4. The Physical Society of Japan (JPS) 67$^{\text{th}}$ Annual (Autumn/Fall) Meeting: **Oral** Presentation, Sep 18 - 21, 2012, Yokohama National University (YNU), Japan. Novel materials design of chalcopyrite type semiconductor based **ferromagnetic half metals** using KKR-CPA-GF method – M. Shahjahan and T. Oguchi

5. International Symposium on Computics: Quantum Simulation and Design (ISC-QSD). **Poster** Presentation, October 11-13, 2012, Osaka University Hall, Osaka, Japan. Chalcopyrite semiconductors $CuInS_2$ and **$CuAlSe_2$** based ferromagnetic half metals – M. Shahjahan, T. Oguchi and K. Shirai

6. Conference on Computational Physics (CCP2012): **Poster** Presentation, October 14-18, 2012, (K-computer site) Kobe, Japan. Ferromagnetic half metals based on chalcopyrite semiconductors $CuAlSe_2$ and $CuInS_2$ – Shahjahan M, Oguchi T and Shirai K

7. 15$^{\text{th}}$ Asian Workshop on First-Principles Electronic Structure Calculations (ASIAN-15): **Poster** Presentation, November 5 - 7, 2012, Institute of Atomic and Molecular

Sciences (IAMS), Academia Sinica, Taipei, Taiwan. Ferromagnetic Half Metals Based on Chalcopyrite Semiconductor $CuInS_2$ –M. Shahjahan, T. Oguchi and K. Shirai

8. The 2nd OU-RuG joint international symposium on particle-nuclear and condensed matter physics: new challenges and opportunities. **Poster** Presentation, November 26-28, 2012, Osaka University, Japan. Half metals based on chalcopyrite semiconductor $CuAlSe_2$ –M. Shahjahan and T. Oguchi

9. The 13th Japan-Korea-Taiwan (JKT) symposium on strongly correlated electron systems: **Poster** Presentation, 15-17 January 2013, Osaka University, Japan. Half metal based on chalcopyrite semiconductor $CuAlSe_2$ –M. Shahjahan and T. Oguchi

10. The Physical Society of Japan (JPS) 68th Annual (Spring) Meeting: **Oral** Presentation, March 26 - 29, 2013, Hiroshima University (HU), Japan. KKR-CPA calculation of magnetic half metal based on chalcopyrite semiconductor $CuAlSe_2$ – M. Shahjahan and T. Oguchi

11. "International Workshop of Computational Nano-Materials Design on Green Energy": **Poster** Presentation, June 16 - 19, 2013, Awaji Yumebutai International Conference Center, Awajishima city, Hyogo, Japan. Dilute Magnetic States Based on Chalcopyrite $AgAlSe_2$ – M. Shahjahan and T. Oguchi

12. "The International Workshop on New Science and Technologies Using Entangled Photons (NSTEP)": **Poster** Presentation, July 8 - 9, 2013, ISIR, Osaka University, Japan. Dilute Magnetic States and Half Metals Based on Chalcopyrite Semiconductors – M. Shahjahan and T. Oguchi

13. The Physical Society of Japan (JPS) 68th Annual (Autumn/Fall) Meeting: **Oral** Presentation, Sep 25 - 28, 2013, Tokushima University, Japan. Electronic Structures and Magnetic States Based on Chalcopyrite $AgAlS_2$ – M. Shahjahan and T. Oguchi

εnd